EXPERIMENTAL AND MODELING EVALUATION OF AQUEOUS-PHASE TRANSPORT BEHAVIOR OF QUANTUM DOTS IN HIGH TEMPERATURE POROUS MEDIA

by

Eric M. Brauser

A dissertation submitted to the faculty of
The University of Utah
in partial fulfillment of requirements for the degree of

Doctor of Philosophy

Department of Chemical Engineering

The University of Utah

December 2016

Copyright Eric M. Brauser 2016

All Rights Reserved

The University of Utah Graduate School

STATEMENT OF DISSERTATION APPROVAL

The dissertation of **Eric M. Brauser**

has been approved by the following supervisory committee members:

John David Mclennan	, Chair	**10/26/2016** Date Approved
Michael H. Risbud Bartl	, Member	**10/31/2016** Date Approved
Peter E. Rose	, Member	**10/26/2016** Date Approved
Terry Arthur Ring	, Member	**10/26/2016** Date Approved
Milind Deo	, Member	**10/26/2016** Date Approved

and by **Milind Deo**, Chair/Dean of

the Department/College/School of **Chemical Engineering**

and by David B. Kieda, Dean of The Graduate School.

ABSTRACT

Semiconductor nanocrystal quantum dots are a relatively recent area of study in materials science and engineering, but their unique, size-dependent properties have resulted in active growth over the past three decades. The motivation for this thesis has been exploiting the ability to tune the energy band gap and develop new families of geothermal reservoir tracers. While colloid transport in porous media has been studied extensively for groundwater systems, there is little existing research appropriate to high temperature geothermal systems. In this research, a multitiered approach is used to characterize quantum dot behavior at temperatures above 100 °C. First, a model system of cadmium selenide (CdSe) quantum dots is used to investigate fundamental aspects of nanocrystal growth and dissolution. Observing quantum dot dissolution and modeling the kinetic parameters yields critically important thermodynamic properties. These parameters are necessary for optimizing large-scale reactor conditions and design, and predicting fluid-phase quantum dot behavior. Insight into these thermodynamic properties provides the basis for experimentally studying transport in high temperature porous media that are surrogates for a geothermal reservoir. Core/shell quantum dots were pumped through Ottawa sand columns under a range of temperatures and salinities. Retardation and deposition were investigated as the principal transport parameters, while also considering the dynamics of quantum dot solubility and the interaction energy between quantum dots and the sand surfaces. Elevated temperatures increased the amount of quantum dot retention, following a multilayer deposition model. Finally, a novel method for detecting optically active species is introduced.

Existing techniques for optical detection of quantum dots fail in turbid or high temperature environments. We demonstrate how the characteristic absorption - coupled with a long-wavelength overtone band - can be used to detect QDs in a variety of industrially relevant mixtures.

TABLE OF CONTENTS

ABSTRACT iii

LIST OF TABLES vii

ACKNOWLEDGEMENTS viii

Chapters

1 – INTRODUCTION TO COLLOID TRANSPORT 1

References 10

2 – EXPERIMENTAL EVALUATION OF KINETIC AND THERMODYNAMIC REACTION PARAMETERS OF COLLOIDAL NANOCRYSTALS 14

Abstract 15
Introduction 15
Experimental Section 16
Results and Discussion 16
Conclusions 20
Supporting Information Available 20
Acknowledgement 20
References 21
Supporting Information 23

3 – EVALUATION OF KINETIC PARAMETERS OF COLLOIDAL NANOCRYSTALS IN AQUEOUS MEDIA 37

Introduction to Quantum Dot Aqueous Solubility 37
Experimental Methods 38
Results 39
Discussion 41
Conclusions 46
References 47

4 – QUANTUM DOT TRANSPORT IN A POROUS MEDIUM 49

Introduction and Motivation 49

Methods – Surface Interaction and Transport 70
Results 82
Discussion 90
Conclusions 102
References 106

5 – OPTICAL DETECTION OF TRACER SPECIES IN STRONGLY SCATTERING MEDIA 109

Abstract 112
Introduction 112
Methods 113
Results and Discussion 113
Conclusions 118
Acknowledgement 118
References 118

6 – OVERALL CONCLUSIONS AND DIRECTION 119

APPENDIX – DERIVATION OF KINETIC EQUATIONS 120

LIST OF TABLES

3.1 Activation energy results for QD growth from Arrhenius model..... 43

4.1 Experimental parameters for calculating interaction potential..... 72

4.2 Ionic strength and temperature conditions for quantum dot transport experiments..... 73

4.3 Percent recovery of quantum dots..... 88

4.4 Average number of counts for cadmium in each section..... 88

4.5 Dimensionless distance location of the downstream concentration peak..... 89

ACKNOWLEDGEMENTS

This thesis was completed with a huge amount of help and support from coworkers and advisors. I want to thank first and foremost my mentors, Dr. Mike Bartl and Dr. John Mclennan for their constant support and encouragement. As my research took its numerous twists and turns, these two scientists were always there to help guide the work towards interesting areas of study. Their teamwork has allowed me to take two fields that seem entirely dissimilar and combine them into interesting and relevant research. Their contributions and editorial insight to this work and my overall experience were instrumental and cannot be understated.

In addition to M. Bartl and J. Mclennan, my committee members, Dr. Milind Deo, Dr. Peter Rose, and Dr. Terry Ring provided many thoughtful insights into my work. M. Deo and P. Rose both contributed significant insight into the behavior of materials in subsurface porous media and the complex geothermal environments found within. Without P. Rose's expert knowledge of geothermal tracer development this project would not have experienced success. T. Ring provided critical analysis of solution-phase colloid behavior and useful explanations of small particle solubility thermodynamics.

Along the way there have been many who contributed valuable knowledge towards some aspect of this research. Dr. Mark Williams at Pacific Northwest National Laboratory allowed me the opportunity to work closely with subsurface numerical modeling. Dr. William Johnson and his research group in the University of Utah department of Geology and Geophysics provided critical insight into colloid transport. Dr. Jacqueline Siy built the

research framework that I used for quantum dot synthesis and dissolution. Members of both the Bartl and Mclennan research groups patiently attended my practice presentations and always gave constructive feedback. My coworkers at the Energy and Geoscience Institute were always helpful with experiment design, ordering materials, fixing electronics and pumps, and finding missing tools. Their contributions made the doctoral process much more endurable.

CHAPTER 1

INTRODUCTION TO COLLOID TRANSPORT

Colloidal transport behavior in the subsurface has been an important topic of research for some time. The original focus was on colloidal facilitation of radionuclides from leaking waste tanks in waste storage zones. Strongly sorbing heavy metals, including plutonium and cesium, were of particular interest due to their introduction to the environment via nuclear weapons production and testing. The presence of naturally occurring colloids in groundwater systems indicated decreased residence times of heavy metals during extraction of groundwater samples from low-permeability formations; residence times would normally be expected to exceed thousands of years.[1–4] Radionuclides sorb strongly to naturally occurring clay and mineral colloids via cation exchange, resulting in subsequent size exclusion from small pores or preventing radionuclide diffusion into low permeability rock matrices. Prior to this discovery, the characterization of nuclide transport in low permeability formations used techniques based on an advection-dispersion transport model with surface sorption acting to retard the radionuclide transport. The presence of colloids creates a type of "conduit" that is akin to a fracture of preferential flow, greatly reducing the residence times and creating a situation of ecological and public health importance. These initial observations of the interactions between elements, molecules, and colloids in groundwater systems have essentially created a new area of research related to environmental transport and the fate of contaminants. Interest remains centered around the

original locations of nuclear testing and waste disposal, such as Yucca Mountain, Nevada or the Hanford site in central Washington. In these localities, understanding the fundamentals of colloid transport and retention is not only a matter of scientific inquiry, but also of public health and welfare.

In addition to understanding the interactions between molecules and natural colloids in facilitated transport, the behavior of engineered nanoparticles in the subsurface is gaining traction; from the perspective of manufacture as well as application. In particular, semiconductor nanoparticle quantum dots (QDs) have been a staple in physical chemistry research laboratories for the past two decades, as scientists explore their unique properties. As they become better understood, the list of potential uses has grown and there has been increased industrial application.

The likelihood of subsurface contamination with nanoparticle colloids becomes more relevant as the field of semiconductor nanoparticles continues to grow. Contamination could arise from intentional release into the environment for remediation or treatment purposes, or via unintentional discharge associated with waste incineration or landfill leaching.[6–10,17–24] In the subsurface, molecular and particle species are exposed to a variety of environments: varied chemical species and concentrations, mineralogic surfaces, solid-liquid and gas-liquid interfaces, and temperature variation. These factors have been the focus of transport studies to ascertain how environmental factors affect the stability and transport properties of QDs.

Elimelech and O'Melia performed breakthrough transport experiments on sets of colloids between 45 and 750 nm in diameter, injected into a column with glass beads as the porous medium. As one of the first publications to explore the relationship between surface interaction and surface force calculations to colloid retention, these authors focused on ionic strength and chemical composition.[25–31] Increases in ionic strength have been found to increase colloid retention in predictable manner when single valent salts were used.

Deposition rates that increase over the course of colloid injection have been observed when high concentrations of double valent anions were present.[31,32] Importantly, these legacy results were framed within single-collector efficiency measurements. Subsequent research of transport in favorable attachment conditions used the log-dependence of collector efficiency to gauge colloid retention. Since identifying the importance of the ionic strength in the colloid retention, particularly using it to find the value of 100% collector efficiency, there have been numerous studies in model systems looking only at permutations of ionic strength in colloid transport. Kretzschmar expanded some of the earlier studies to identify possible mechanisms of retention that may be caused by differences in column material and subsequent physical parameters, such as porosity, surface charge, pore sizing, or surface roughness.[33] These and corresponding work by others showed that ionic strength, even when there are only very slight changes, is an important factor in predicting colloid retention, while introducing some of the other subsurface conditions to be expanded upon in the following decades.[34–44]

As indicated, one of the primary motivations for colloid study was to develop a better understanding of colloid-facilitated transport of radionuclides that had already been introduced into the subsurface. The development of remediation strategies for this radionuclide contamination relied heavily on laboratory transport experiments and subsequent model development for success. For example, Painter et al. implemented multi-phase radionuclides modeling, including molecule-to-colloid and colloid-to-surface transport and adsorption. This allowed those authors to accurately predict the relevant kinetic processes that dictate residence times in the subsurface.[4] More broadly, understanding that these shifts in environmental conditions can cause these rates to change are pieces of information that are required for predicting the fate of colloid-bound radionuclides in the subsurface.

The observation that colloid behavior deviated from predicted breakthrough curves (BTCs) led to the acknowledgement that the understanding of mechanisms was incomplete. Kretzschmar et al. noted that the retention of colloids decreased with an increase in pore water velocity, in agreement with the predictions of the colloid deposition rate term of the advection-dispersion equation (ADE).[33] The attachment efficiency α is the fraction of colloid-collector collisions resulting in permanent colloid retention. This term reconciles the theoretical single collector efficiency η with experimental observations. The column retention and single-collector efficiency terms (η and α) began as phenomenological constants with little basis in interaction energy due to the complexity of factors that drive colloid transport. Rajagopalan et al. and Yao et al. developed sets of dimensionless parameters that describe single collector efficiency under a variety of circumstances.[45,46] These allow rapid determination of the dominant mechanisms of colloid removal in particular experimental conditions. They note that as particle size decreases, the effect of hydrodynamic forces upon colloid retention diminishes (i.e., the particle acts more molecule-like and its transport is increasingly dictated by Brownian forces). An updated correlation equation was determined by numerical solution of the ADE using a variety of physical parameters (size, fluid velocity, density, etc.).[47] The correlation equation was then used to predict colloid retention from previously published experimental data and was shown to be a significant improvement over existing work. This result has been used extensively over the past decade for validation of experimental work, though it has been the center of debate over the significance of all the dimensionless parameters.[33,40,44,48–50] This updated approach to predicting colloid transport from experimental parameters is used to bridge classic filtration theory with experimental results and provides information on the removal mechanisms of colloids in various systems.

The correlation equations dictate that diffusion, convection, sedimentation/settling,

the relative size between colloid and collector, and electrostatic interactions are the controlling forces for colloid retention.[47,51] Many scientists have investigated which physical parameters play a role in each mechanism. For some it is a simple case of experiment parameters such as the colloid and collector size or the system geometry; in others, it is an intensive property (colloid density, fluid density) that does not change between experiments.[35,39,41,42,52–55] The variety of mechanisms proposed by Tufenkji and Elimelech that contribute to colloid retention is extensive, though the large influence ionic strength has on colloid retention was quickly identified. The role of ionic strength in colloid retention is attributed to its effect on the distance that a surface charge density can be "felt" by other surfaces and species. This effect decreases with higher salinities. Classical filtration theory makes use of column BTCs to study the deposition rate of colloids under favorable attachment conditions. This approach has led to numerous studies where the ionic strength is large enough to remove the energy barrier to attraction.[37,44] For single systems, the attachment efficiency can be shown to increase log-linearly until a minimum ionic strength is reached at which point the retention of colloids reaches 100%.[51] This is a critical parameter for understanding removal of colloids from either filtration or environmental systems.[56–58] Experimental work has typically focused on single valent ions in solution to control the ionic strength as divalent ions can lead to confounding results. The issues with divalent ions are potentially due to bridging between collector and colloid.[25,29–31]

The ionic strength is used to calculate the electrostatic potential between the colloid and collector, using electric double layer (EDL) theory.[29,59] Tying the intensity of interaction profile features, such as the primary energy barrier height or secondary well depth, to experimentally determined column retention efficiencies has proven to be difficult. Limited success has come from mechanistic analysis of the forces acting on the particles, since hydrodynamic forces through a pore throat can be significant factors in colloid recovery. The

velocity distributions around heterogeneous collectors, the subsequently poorly-defined velocity fields, and the distance of attractive or repulsive interaction from the charged surfaces all decrease the accuracy of theoretical prediction of colloid recovery.[54,60–62] Often, studies on systems of environmental interest are necessary (i.e., using the unique conditions from the field to guide laboratory parameters), as complete mechanistic analysis generally requires high-level computational tools. As for numerical evaluations, many successful studies have used mechanistic and particle trajectory analyses to gain understanding of how colloids move past different regions of a collector: through pore throats, near- and far-surface regions, and front and rear stagnation zones.[35,40,63]

Even with the development of correlation equations for attributing different physics to colloid retention, there remains uncertainty in when different mechanisms control how colloids are collected. Lingering deviations in the correlation equation results required developing new experiments to identify specific retention mechanisms. Tong et al. observed differences in the retention of colloids between column transport and impinging jet experiments, which should be analogous to one another.[54] They hypothesized that the difference in retention was due to the particular geometry in the column and the presence of grain-to-grain contacts. Tong et al. found that the increased velocity due to narrowing of the pore throats was funneling the colloids. The hydrodynamic forces were overcoming electrostatic repulsion and actually inducing aggregation. The aggregates then would bridge in the narrow pore throats via straining. This was observed in BTCs that had time-dependent kinetic deposition rates. It was also verified using optical microscopy to directly observe colloids located in pore throats. Subsequent particle trajectory studies showed that particles with diameters on the order of microns showed significant removal by straining in grain-to-grain contacts. This was observed when chemical conditions were either favorable or unfavorable for surface deposition as well.[61] Johnson et al. analyzed different mechanisms for

straining in various colloid systems, and compared mechanistic behavior to results published in the prior decade (2000-2010).[54,63] The width of the pore throat is not as easily measured as the diameter of the collector, but is proposed to offer a better metric for the dominance/occurrence of straining.

There has been a significant amount of study related to the transport of particles to understand the location of the retained particles. Understanding the fate of retained particles provides insight and potential validation of retention mechanisms in different environments. These studies predict the effect of pore water velocity upon retention mechanism by evaluating drag forces, velocity fields, and interaction energies.[35,40,60,61,63,64] A significant amount of early work used larger (>1 μm diameter) colloids. Consequently, these colloids are strongly affected by hydrodynamic drag due to the velocity fields rather than Brownian dynamics. The present work evaluates factors to be considered for sub-micron nanoparticles. In this regard, modeling showed that colloids were likely translating along the surface preferentially over transport in the bulk fluid phase. This is due to decreased velocities near the collector surfaces and the possible presence of an attractive secondary energy minimum that is essentially pulling the colloid. Numerous studies show that colloids often deposit preferentially in the rear stagnation zone of a collector where flow velocities are very low and it is possible for the secondary minimum to be the dominant force acting on the colloid.[55,62] For nanoparticles under 100 nm diameter, May et al. performed experiments in a single layer of porous media and visualized fluorescent nanoparticles following injection.[35] They found that the nanoparticles preferentially deposited in the rear stagnation zone rather that at grain-to-grain contacts. They attributed this to diffusive transport across streamlines, where larger particles are more likely to be swept along in their current streamline and less able to diffuse to the no-flow regions. These instances were subsequently shown to be more dramatic with an increase in ionic strength, suggesting that the interaction energy is

dominating colloid retention.

While many of the previous studies have considered the fundamental physics of colloid retention in porous media, there have been a number of studies that have provided insights into "real-world" colloid transport. This is the result of colloid transport research transitioning away from the fundamental physics of retention and back into industry-driven porous media remediation. Often these conditions are specific to a particular subsurface reservoir where nanoparticle or colloid transport is relevant, such as the Hanford site. One particularly important field of colloid transport research involves their behavior in the vadose zone.[39,65] The vadose zone is a near-surface region with partial groundwater saturation. Uyusur et al. suggest that colloids may have unique behavior at the gas-liquid interface, which potentially acts as a retention mechanism.[34] This type of retention is common. The analyte/tracer is retarded due to a two-phase boundary, often between mobile and immobile fluid phases. Uyusur et al. also suggested that, with an extensive set of QD transport experiments over a range of environmentally-relevant ionic strength, retention was dictated by the degree of saturation of the porous media. Retention increased when the gas-liquid boundaries in the system was more extensive.[34] The vadose zone is particularly relevant to current studies for two reasons: 1) Generally, if nanoparticles are being introduced to groundwater systems, they will first move through an unsaturated porous medium. 2) Specifically, some of the domains where nuclear waste contamination has occurred (Hanford, WA and Yucca Mt., NV) include unsaturated/partially saturated subsurface regimes into which tanks are slowly leaching radionuclides.[2,3] To facilitate remediation planning, the behavior of colloids at the gas-water interface needs to be understood. Uyusur et al. and Darnault et al. both observed preferential retention of colloids (inorganic and biological, respectively) at the gas-water interface.[34,66] This interfacial retention was more effective at increasing QD retention than straining or adsorption. This

preferential effect was demonstrated by the reduction in recovery from 80% to 40% under identical physical conditions but with the addition of gas phase regions.[67] This observation invites consideration of the variability in fluid velocity, salinities, and degree of saturation, due to the variable nature of the water table due to flooding events, changes in local aquifer chemistry, and salinity plumes. The effect of a transient chemical environment was studied extensively by Saiers and Lenhart.[39] This arises when a large volume of chemically different water passes through a porous medium, as might occur due to a meteorological event, such as a heavy rainstorm. They noted the importance of the interaction potential and its sensitivity to the perturbation in ionic strength. Changes of the interaction force strength are of particular interest to either colloid-facilitated transport of nuclides or to the behavior of colloid-like bacteria, both of which have been studied from the perspective of colloid transport. Saiers and Lenhart studied the effect of decreasing the amount of sodium chloride in consecutive infiltrations into a porous media containing adsorbed colloids (a favorable retention environment). The decrease in ionic strength with each pulse resulted in colloid desorption due to the larger primary energy barrier at low ionic strength.[39]

In empirical, laboratory assessments of the degree of colloid retention, silica spheres are commonly used in model systems. These spheres are readily available, are resistant to chemical environments, and can be selected to provide a narrow particle size distribution. In these model experiments, concentrations, locations and retention of colloids are detected or inferred in a number of ways: particle counting[41], optical detection of encapsulated dyes[68], and optical density measurements.[28] The widespread availability of inexpensive, custom fluorescent microspheres has greatly increased their usage. These methods count discrete particles or report electrical signal responses, and do not rely on static colloid sizes for accuracy. However, QDs are incredibly small colloids that have optical properties that are very sensitive to the colloid size. Small changes in a QD's size can lead to large changes of the

characteristic absorption and emission wavelengths of the QD. In order to develop QDs as a tracer for high temperatures and extreme chemical environments, fundamental aspects of nanoparticle growth and dissolution needed to be investigated.

References

(1) Zhuang, J.; Flury, M.; Jin, Y. *Environ. Sci. Technol.* **2003**, *37* (21), 4905–4911.

(2) Novikov, A. P.; Kalmykov, S. N.; Utsunomiya, S.; Ewing, R. C.; Horreard, F.; Merkulov, A.; Clark, S. B.; Tkachev, V. V.; Myasoedov, B. F. *Science* **2006**, *314* (5799), 638–641.

(3) Kersting, A. B.; Efurd, D. W.; Finnegan, D. L.; Rokop, D. J.; Smith, D. K.; Thompson, J. L. *Nature* **1999**, *397* (6714), 56–59.

(4) Painter, S.; Cvetkovic, V.; Pickett, D.; Turner, D. R. *Environ. Sci. Technol.* **2002**, *36* (24), 5369–5375.

(5) Nirmal, M.; Brus, L. *Acc. Chem. Res.* **1999**, *32* (5), 407–414.

(6) Murray, C. B.; Norris, D. J.; Bawendi, M. G. *J. Am. Chem. Soc.* **1993**, *115* (19), 8706–8715.

(7) Kwon, S. G.; Hyeon, T. *Small* **2011**, *7* (19), 2685–2702.

(8) Peng, Z. A.; Peng, X. *J. Am. Chem. Soc.* **2002**, *124* (13), 3343–3353.

(9) Cumberland, S. L.; Hanif, K. M.; Javier, A.; Khitrov, G. A.; Strouse, G. F.; Woessner, S. M.; Yun, C. S. *Chem. Mater.* **2002**, *14* (4), 1576–1584.

(10) Bullen, C. R.; Mulvaney, P. *Nano Lett.* **2004**, *4* (12), 2303–2307.

(11) Liu, H.; Owen, J. S.; Alivisatos, A. P. *J. Am. Chem. Soc.* **2007**, *129* (2), 305–312.

(12) Siy, J. T.; Brauser, E. H.; Thompson, T. K.; Bartl, M. H. *J. Mater. Chem. C* **2013**, *2* (4), 675–682.

(13) Siy, J. T.; Brauser, E. M.; Bartl, M. H. *Chem. Commun.* **2010**, *47* (1), 364–366.

(14) Wood, V.; Panzer, M. J.; Caruge, J.-M.; Halpert, J. E.; Bawendi, M. G.; Bulović, V. *Nano Lett.* **2010**, *10* (1), 24–29.

(15) Talapin, D. V.; Steckel, J. *Quantum dot light-emitting devices,* MRS Bull. **2013**, *38* (09), 685–691.

(16) Klimov, V. I.; Ivanov, S. A.; Nanda, J.; Achermann, M.; Bezel, I.; McGuire, J. A.; Piryatinski, A. *Nature* **2007**, *447* (7143), 441–446.

(17) Tessler, N.; Medvedev, V.; Kazes, M.; Kan, S.; Banin, U. *Science* **2002**, *295* (5559), 1506–1508.

(18) Kretzers, I. K. J.; Parker, R. J.; Olkhov, R. V.; Shaw, A. M. *J. Phys. Chem. C* **2009**, *113* (14), 5514–5519.

(19) Torkzaban, S.; Bradford, S. A.; Wan, J.; Tokunaga, T.; Masoudih, A. *Environ. Sci. Technol.* **2013**, *47* (20), 11528–11536.

(20) Elimelech, M. *J. Colloid Interface Sci.* **1994**, *164* (1), 190–199.

(21) Elimelech, M.; O'Melia, C. R. *Environ. Sci. Technol.* **1990**, *24* (10), 1528–1536.

(22) Trefalt, G.; Szilagyi, I.; Borkovec, M. *J. Colloid Interface Sci.* **2013**, *406*, 111–120.

(23) Taghavy, A.; Mittelman, A.; Wang, Y.; Pennell, K. D.; Abriola, L. M. *Environ. Sci. Technol.* **2013**, *47* (15), 8499–8507.

(24) Huynh, K. A.; Chen, K. L. *Environ. Sci. Technol.* **2011**, *45* (13), 5564–5571.

(25) Oncsik, T.; Trefalt, G.; Csendes, Z.; Szilagyi, I.; Borkovec, M. *Langmuir* **2014**, *30* (3), 733–741.

(26) Kretzschmar, R.; Barmettler, K.; Grolimund, D.; Yan, Y.; Borkovec, M.; Sticher, H. *Water Resour. Res.* **1997**, *33* (5), 1129–1137.

(27) Uyusur, B.; Darnault, C. J. G.; Snee, P. T.; Kokën, E.; Jacobson, A. R.; Wells, R. R. *J. Contam. Hydrol.* **2010**, *118* (3–4), 184–198.

(28) May, R.; Akbariyeh, S.; Li, Y. *Environ. Sci. Technol.* **2012**, *46* (18), 9980–9986.

(29) Kini, G. C.; Yu, J.; Wang, L.; Kan, A. T.; Biswal, S. L.; Tour, J. M.; Tomson, M. B.; Wong, M. S. *Colloids Surf. Physicochem. Eng. Asp.* **2014**, *443*, 492–500.

(30) Siubhan A. Macpherson, G. B. W. *Adv. Powder Technol.* **2012**, *23*, 478–484.

(31) Bradford, S. A.; Torkzaban, S.; Shapiro, A. *Langmuir* **2013**, *29* (23), 6944–6952.

(32) Saiers, J. E.; Lenhart, J. J. *Water Resour. Res.* **2003**, *39* (1), 1019.

(33) Kuznar, Z. A.; Elimelech, M. *Colloids Surf. Physicochem. Eng. Asp.* **2007**, *294* (1–3), 156–162.

(34) Tong, M.; Johnson, W. P. *Environ. Sci. Technol.* **2006**, *40* (24), 7725–7731.

(35) Johnson, W. P.; Tong, M. *Environ. Sci. Technol.* **2006**, *40* (16), 5015–5021.

(36) Torkzaban, S.; Kim, H. N.; Simunek, J.; Bradford, S. A. *Environ. Sci. Technol.* **2010**, *44*

(5), 1662–1669.

(37) Shen, C.; Li, B.; Huang, Y.; Jin, Y. *Environ. Sci. Technol.* **2007**, *41* (20), 6976–6982.

(38) Rajagopalan, R.; Tien, C. *AIChE J.* **1976**, *22* (3), 523–533.

(39) Yao, K.-M.; Habibian, M. T.; O'Melia, C. R. *Environ. Sci. Technol.* **1971**, *5* (11), 1105–1112.

(40) Tufenkji, N.; Elimelech, M. *Environ. Sci. Technol.* **2004**, *38* (2), 529–536.

(41) Seymour, M. B.; Chen, G.; Su, C.; Li, Y. *Environ. Sci. Technol.* **2013**, *47* (15), 8391–8398.

(42) Christiane Shani, N. W. *Colloids Surf. Physicochem. Eng. Asp.* **2008**, *316* (1-3), 142–150.

(43) Johnson, W. P.; Tong, M.; Li, X. *Water Resour. Res.* **2007**, *43* (12), W12S13.

(44) Tufenkji, N.; Elimelech, M. *Langmuir ACS J. Surf. Colloids* **2004**, *20* (25), 10818–10828.

(45) Sasidharan, S.; Torkzaban, S.; Bradford, S. A.; Dillon, P. J.; Cook, P. G. *Colloids Surf. Physicochem. Eng. Asp.* **2014**, *457*, 169–179.

(46) Li, Y.; Wang, Y.; Pennell, K. D.; Abriola, L. M. *Environ. Sci. Technol.* **2008**, *42* (19), 7174–7180.

(47) Tong, M.; ma, H.; Johnson, W. P. *Environ. Sci. Technol.* **2008**, *42* (8), 2826–2832.

(48) Torkzaban, S.; Bradford, S. A.; Walker, S. L. *Langmuir* **2007**, *23* (19), 9652–9660.

(49) Petosa, A. R.; Jaisi, D. P.; Quevedo, I. R.; Elimelech, M.; Tufenkji, N. *Environ. Sci. Technol.* **2010**, *44* (17), 6532–6549.

(50) Chen, K. L.; Elimelech, M. *Environ. Sci. Technol.* **2009**, *43* (19), 7270–7276.

(51) Chen, K. L.; Elimelech, M. *Langmuir* **2006**, *22* (26), 10994–11001.

(52) Hogg, R.; Healy, T. W.; Fuerstenau, D. W. *Trans. Faraday Soc.* **1966**, *62* (0), 1638–1651.

(53) Bradford, S. A.; Simunek, J.; Bettahar, M.; Van Genuchten, M. T.; Yates, S. R. *Environ. Sci. Technol.* **2003**, *37* (10), 2242–2250.

(54) Johnson, W. P.; Ma, H.; Pazmino, E. *Environ. Sci. Technol.* **2011**, *45* (9), 3831–3832.

(55) Johnson, W. P.; Li, X.; Yal, G. *Environ. Sci. Technol.* **2007**, *41* (4), 1279–1287.

(56) Johnson, W. P.; Pazmino, E.; Ma, H. *Water Res.* **2010**, *44* (4), 1158–1169.

(57) May, R.; Li, Y. Colloids Surf. Physicochem. Eng. Asp. **2013**, 418, 84–91.

(58) Wan, J.; Tokunaga, T. K. *Environ. Sci. Technol.* **1998**, *32* (21), 3293–3298.

(59) C. J. G. Darnault, T. S. S. *Vadose Zone J.* **2004**, *3* (1), 262–270.

(60) Chen, L.; Sabatini, D. A.; Kibbey, T. C. G. *Environ. Sci. Technol.* **2008**, *42* (6), 1916–1921.

(61) Bradford, S. A.; Simunek, J.; Bettahar, M.; Tadassa, Y. F.; van Genuchten, M. T.; Yates, S. R. *Water Resour. Res.* **2005**, *41* (10), W10404.

CHAPTER 2

EXPERIMENTAL EVALUATION OF KINETIC AND THERMODYNAMIC REACTION PARAMETERS OF COLLOIDAL NANOCRYSTALS

Reproduced with permission from Brauser, E. M., Hull, T.D., McLennan, J. D., Siy, J. T., and Bartl, M. H. Experimental evaluation of kinetic and thermodynamic reaction parameters of colloidal nanocrystals. *Chem. Mater.*, **2016**, *28* (11), pp 3831–3838. Copyright 2016 American Chemical Society.

CHEMISTRY OF MATERIALS

Article

pubs.acs.org/cm

Experimental Evaluation of Kinetic and Thermodynamic Reaction Parameters of Colloidal Nanocrystals

Eric M. Brauser,[†,‡,⊥] Trevor D. Hull,[†,⊥] John D. McLennan,[‡] Jacqueline T. Siy,[*,§] and Michael H. Bartl[*,†]

[†]Department of Chemistry, University of Utah, Salt Lake City, Utah 84112, United States

[‡]Department of Chemical Engineering, University of Utah, Salt Lake City, Utah 84112, United States

[§]Navillum Nanotechnologies, LLC, South Salt Lake, Utah 84115, United States

Supporting Information

ABSTRACT: The unique properties of colloidal semiconductor nanocrystals, or quantum dots, have attracted enormous interest in a wide range of applications, including energy, lighting, and biomedical fields. However, widespread implementation is hampered by the difficulty of developing large-scale and inexpensive synthesis routes, mainly due to our limited knowledge of formation reaction parameters. We report here a simple yet powerful method to experimentally determine critically important reaction parameters such as rate constants, activation barriers, equilibrium constants and reaction enthalpies. This method was applied to wurtzite cadmium selenide nanocrystals, yielding activation energies for growth and dissolution of 14 ± 6 kJ mol^{-1} and 27 ± 8 kJ mol^{-1}, respectively, and a reaction enthalpy for nanocrystal growth of −15 ± 7 kJ mol^{-1}. Moreover, the Gibbs free energy for growth was found to be negative at low temperatures, whereas dissolution becomes the spontaneous process above 150 °C.

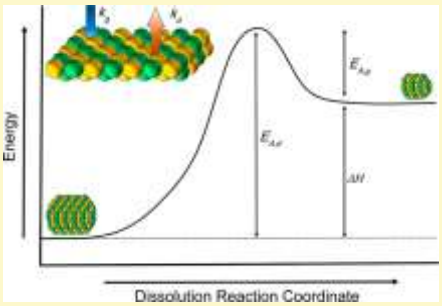

INTRODUCTION

Chemical reactions are characterized by underlying thermodynamic and kinetic properties, including reaction enthalpy and entropy, equilibrium and rate constants, and activation energies. Competitive control of these properties determines key reaction parameters such as direction and extent of a reaction, stability of reactants and products, and overall reactivity. Thermodynamic and kinetic quantities have thus been evaluated and tabulated for nearly every chemical reaction. Knowledge of these properties is of great importance in basic research and in industry for developing new reactions, optimizing reaction conditions, finding catalytic pathways, streamlining manufacturing processes, and optimizing reactor design. Surprisingly, such knowledge is largely missing for formation reactions of colloidal nanocrystals, including the important class of semiconductor quantum dots (QDs).[1−4] Nanocrystal QDs are typically formed from metal−organic precursors and intermediates in the presence of surface stabilizing ligands, conditions significantly different than for crystallization of bulk compounds.[5−13] Because of the lack of thermodynamic and kinetic information, fabrication of semiconductor nanocrystals is still largely based on optimizing small-batch synthesis reactions through tedious trial-and-error approaches. This process is slow, expensive, and lacks the control and reproducibility needed for widespread technological use of this emerging class of quantum materials.

The enormous interest in colloidal semiconductor nanocrystals stems from their size- and shape-tunable optical and electrical properties deriving from quantum size effects and strongly confined excitons.[3,4] These unique phenomena have opened the door for developing new materials with applications in photonics and nanoelectronics,[14−17] energy and lighting technologies,[18,19] and biomedical sciences.[20−22] In fact, recent market estimates for semiconductor QD materials predict a potential market value of more than $4.7 billion by 2020.[23] However, such precipitous growth of nanocrystal-based technologies will require a drastic change in the way semiconductor QDs are fabricated: transitioning from current small-batch synthesis to large-scale industrial manufacturing processes.

The major roadblock to this transition is the high reaction temperature required in current synthesis routes, which are still largely based on a method originally developed by Murray, Norris, and Bawendi more than 20 years ago.[6] For example, synthesis of high-quality wurtzite cadmium chalcogenide nanocrystal QDs, by far the most important and most widely used type of nanocrystals, requires reaction temperatures in the 200−350 °C range.[6−11] Although such temperatures are relatively simple to implement for small research-type reaction volumes, scaling-up is very difficult due to issues such as handling of organic solvents and reactants at high temperatures, formation of unwanted temperature gradients in large reaction volumes, and the requirement for rapid precursor injection and mixing. Synthesis methods below 150 °C, on the other hand,

Received: March 1, 2016
Revised: May 4, 2016
Published: May 20, 2016

 © 2016 American Chemical Society

DOI: 10.1021/acs.chemmater.6b00878
Chem. Mater. 2016, 28, 3831−3838

would be more straightforward to scale up. However, it has proven extremely challenging to find reaction conditions at lower temperatures that result in high-quality wurtzite CdSe nanocrystals.[12,13,24] Recent studies have shown that crystal nucleation can occur at lower temperatures, but the transition from stabilized nuclei (or "magic-sized" clusters) to continuously growing nanocrystals remains a bottleneck.[13,24,25]

These recent findings underline the need for a comprehensive data set of thermodynamic and kinetic properties that could guide the development of effective low-temperature synthesis routes for semiconductor QDs. Previous efforts in this direction have largely focused on experimental or theoretical determination of rate kinetics from a bottom-up perspective of nanocrystal formation.[26−34] For example, Rempel et al. provide a kinetic model for nanocrystal growth and dissolution, investigating the impact of critical reaction parameters on nucleation, size distribution and size focusing.[29] Experimental realization of these models is very difficult due to the rapid kinetics at high temperatures as well as competing processes including crystal nucleation, reaction- or diffusion-limited growth, and Ostwald ripening. These competing processes require assumptions of distinct formation and ripening mechanisms that complicate the modeling of an overall governing rate equation, which can lead to ambiguous results.[10,27,29]

In this paper, we present a fundamentally different approach to evaluating reaction parameters for colloidal nanocrystal QDs. Instead of studying nanocrystal QDs during the high-temperature growth process, we studied the "back reaction" to growth: the equilibrium-based dissolution process at temperatures between 80 and 180 °C. Using wurtzite CdSe QDs as a model system, the dissolution process is monitored *in situ* by UV−vis absorption spectroscopy via a fiber-optic probe. Experimental data were fit to framework rate equations that describe the transient QD size. The fitted rate constants for dissolution and growth were then used to derive fundamental kinetic and thermodynamic properties, including activation barriers, equilibrium constants, and reaction enthalpies and entropies.

EXPERIMENTAL SECTION

All chemicals were used as purchased without further purification. Cadmium acetate (98%), hexanes (98.5%), and technical grade trioctylphosphine (TOP), trioctylphosphine oxide (TOPO), and 1-octadecene were purchased from Sigma-Aldrich. Acetone (99.8%) and toluene (99.9%) were obtained from Fischer. Elemental selenium (99.5%) was provided by Acros and stearic acid (98%) was purchased from Alfa-Aesar.

CdSe Nanocrystal QD Synthesis. Size-monodisperse wurtzite CdSe QDs with different diameters in the range of 4−5 nm were synthesized by a high-temperature method adapted from previous studies.[28,42] Briefly, a cadmium precursor was made by dissolving 0.24 g of cadmium acetate dihydrate in 3.0 g of stearic acid (SA) in an inert-gas atmosphere at a temperature of 130 °C. This solution was then aged overnight at room temperature. Like batch numbers were used whenever results were to be compared to minimize the effect of ligand impurities, primarily variation in alkyl chain length. Afterward, 9.0 g of trioctylphosphine oxide (TOPO) was added and the mixture was heated to 300 °C under inert gas. A selenium precursor was prepared concurrently by dissolving 0.255 g of elemental selenium in 13.5 mL of trioctylphosphine (TOP) and 1.2 mL of toluene under inert gas. 10.5 mL of the selenium solution was then quickly injected into the cadmium containing solution at 300 °C. To reduce the influence of any size-dependent growth or dissolution behaviors in later experiments, the batch syntheses targeted QD radii of approximately 2.2 nm. This was achieved by keeping the reaction mixture at 300 °C for 30 s before removing it from the heating mantle and allowing it to cool to room temperature. The CdSe QDs were separated from the growth solution and purified by repeated hexanes-ethanol suspension-precipitation cycles. Purified QDs were dissolved in hexanes. The size and shape of QDs was characterized by transmission electron microscopy.

In Situ Dissolution Studies. *In situ* dissolution measurements were made using a fiber-optic transmission dip probe in a modified method developed previously in our group.[28] In short, purified wurtzite CdSe QDs were injected into the noncoordinating solvent 1-octadecene (ODE) at a given temperature (80−180 °C). For this, 100 mL of ODE was filled into a 250 mL three-necked round-bottomed flask equipped with a fiber-optic transmission dip probe connected to a UV−vis spectrometer. The ODE was briefly held under vacuum to remove dissolved gases and then heated to the desired reaction temperature under inert gas. A small amount of concentrated QDs in hexanes solution (∼0.2 mL) was then injected into ODE under heavy stirring to give a final QD concentration of 5×10^{-7} M. *In situ* UV−vis absorption measurements (see below) were started immediately. This procedure was repeated for various reaction temperatures between 80 and 180 °C.

Optical Spectroscopy. *In situ* UV−vis absorption measurements were performed using a TI300-UV−vis transmission dip probe fiber-coupled to a USB2000 miniature Fiber Optic Spectrometer and a LS-1 tungsten halogen white light source. All components were purchased from Ocean Optics. To follow the reaction (dissolution) progress, spectra were recorded at a frequency of 10 Hz (integration time of 100 ms per spectrum).

Data Analysis and Modeling. The first step in data analysis was a temperature correction of the measured wavelength position using the Varshni coefficients (see Supporting Information). QD radii were then calculated using the equation for CdSe given in ref 35, and tabulated as a function of dissolution time. QD radii vs. dissolution time data set were fitted to eq 3 or eq 4 to extract values for the rate constants of growth and dissolution, k_g and k_d, respectively. Initial values of k_g and k_d were applied and a set of nested functions was then used within the Matlab function ODE113 to optimize k_d and k_g by minimizing the square of the residuals. ODE113 was found to be less susceptible than other solvers to the experimental noise at longer times. Initial k_g and k_d values were varied within 5 orders of magnitude to test the stability of the solution set; only solutions for which full convergence was obtained were used for further analysis. The uncertainties for optimized k_g and k_d values were determined by evaluating the sensitivity of the sum of squares of the residuals (SSR) of each parameter. The evaluated uncertainties for k_g and k_d were then used for calculating uncertainties of subsequent quantities via traditional error propagation.

RESULTS AND DISCUSSION

The equilibrium-based growth reaction of a nanocrystal QD_n of size n [CdSe] units (in the wurtzite crystal lattice) can be given in simplified form as[28,29]

$$QD_n + M_1 \leftrightarrow QD_{n+1} \quad (1)$$

with M_1 being a [CdSe] monomer in solution. This reaction formulation does not require knowledge of complex monomer conversion mechanisms, and instead assumes overall kinetics are contingent upon a single rate-limiting step.[29] Equation 1 describes the attachment of a [CdSe] unit from solution to a QD (growth), whereas the "back reaction" of eq 1 is simply the detachment of a [CdSe] unit from a QD, or dissolution of a (n +1)-sized QD by one monomer unit, M_1. The interaction of a QD surface with monomers in solution is thus a dynamic system in which the individual monomer building blocks of the nanocrystal are constantly transferring between solid and solution phases. In our experimental setup, purified CdSe

DOI: 10.1021/acs.chemmater.6b00878
Chem. Mater. 2016, 28, 3831−3838

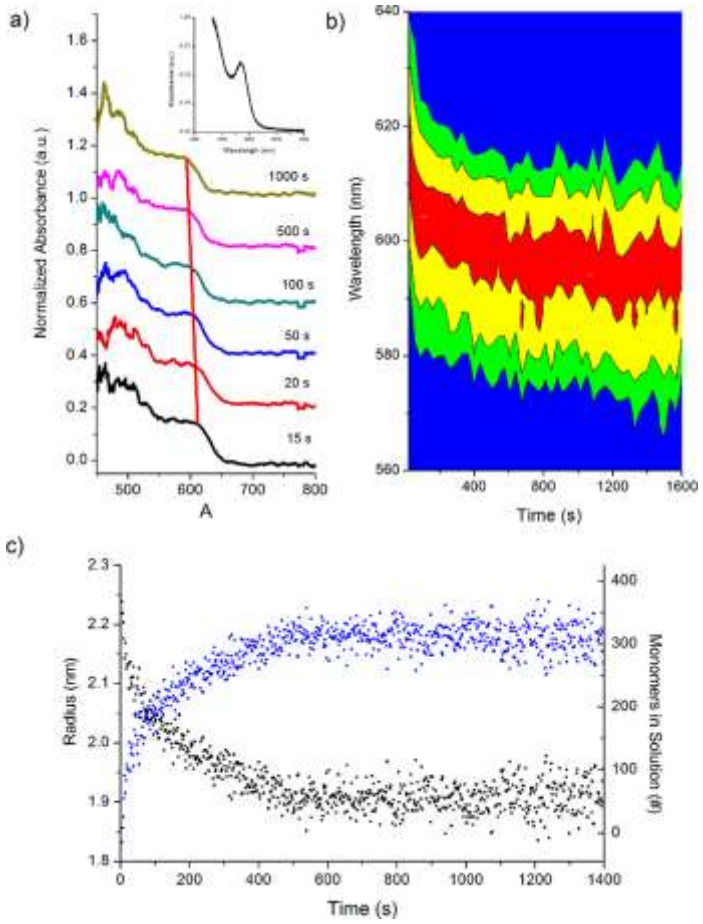

Figure 1. Temporal change of optical spectroscopy data, size evolution and monomer concentration of CdSe nanocrystal quantum dots during equilibrium-based dissolution at 180 °C. (a) Series of optical absorption spectra of CdSe nanocrystals recorded in situ at various times of the dissolution process. The red line traces the shift of the characteristic wavelength. The inset is an absorption spectrum from a sample of the purified nanocrystals. (b) Color-encoded evolution of the nanocrystal optical absorption section. For each spectrum the absorbance at the maximum of the first excitonic absorption peak was normalized to one and spectra are shown using the absorbance-range color codes: 1–0.9 (red), 0.9–0.8 (yellow), 0.8–0.7 (green), and <0.7 (blue). (c) Temporal change of the derived nanocrystal radius using eq S2 (black dots) and the per-nanocrystal-number of dissolved [CdSe] monomers in solution using eq 2 (blue dots).

QDs are injected into a neat, noncoordinating solvent. At this initial stage, eq 1 is far off equilibrium and monomer units dissolve from the QD surface. The initially rapid QD dissolution slows as the monomer gradient decreases and the likelihood of recrystallization of solution-based monomers increases. Eventually, an equilibrium state is reached in which the crystal dissolution and growth rates are balanced and a stable QD size should be observed.

Experimentally, the dissolution process of CdSe QDs can be detected by monitoring their first excitonic absorption peak (Figure 1a,b). The wavelength position of this transition is a direct function of QD size and its dependence can be described by a semiempirical expression developed by Peng and co-workers (see Supporting Information, eq S2).[35] It is important to note this equation describes the relationship between QD size and wavelength position of the first excitonic absorption peak at room temperature. We used the Varshni equation to correct for temperature effects on the measured absorption spectrum, which takes into account the effect of temperature on both crystal expansion and electron–phonon coupling.[36] After a set of temperature-dependent and experimentally verified Varshni correction factors were derived (see Supporting Information), all wavelength positions of the first excitonic absorption features were corrected to room-temperature values. This allowed accurate calculation of the QD size. Furthermore, knowing the QD diameter at the start of dissolution (D_0) and at a given time t (D_t) as well as the CdSe molar volume (V_m), eq 2 can be used to calculate the number of [CdSe] monomer units, $M_1(t)$, in solution as a result of dissolution per QD (with N_A being the Avogadro number).

$$M_1(t) = \frac{(D_0^3 - D_t^3)\cdot\pi\cdot N_A}{6V_m} \quad (2)$$

Figure 1c shows the size evolution of CdSe QDs and the increase in free [CdSe] monomers during dissolution at a

DOI: 10.1021/acs.chemmater.6b00878
Chem. Mater. 2016, 28, 3831–3838

temperature of 180 °C. The dissolution process was confirmed by transmission electron microscopy, and X-ray diffraction studies revealed that the QDs retained the wurtzite structure during dissolution.[28]

The experimental dissolution data follow the expected behavior of a system described by eq 1. The initial far-from-equilibrium state causes rapid transfer of [CdSe] monomers from the crystal surface into solution. This drives the reaction to the left. This initial dissolution is limited only by the kinetic rate at which the monomers can detach from the QD surface. At long times (beyond 600 s) attachment and detachment kinetics of monomers at the crystal surface reach steady-state condition with a stable equilibrium radius and monomer concentration.

A differential rate equation was derived for the reaction given in eq 1 by tracking the transition of individual monomers between crystal and solution phase. Variations of this equation have been reported previously in literature. Those reported relationships have been expressed on a per-QD basis or have accounted for all QDs in a solution of known volume and concentration.[10,27,29] Equation 3 includes terms for both growth and dissolution contributions to the time-dependent QD radius, $r(t)$ and is a formulation based on a per-QD model with a per-QD unit volume of solution (V_u).

$$\left(\frac{1}{N_0}\right)\frac{dr(t)}{dt} = k_g\left(\frac{4\pi}{3}\right)\left(\frac{1}{V_u}\right)[r_0^3 - r(t)^3] - k_d V_m \quad (3)$$

In eq 3, k_g and k_d are the rate constants of growth and dissolution, respectively, N_0 is the number of QDs, and r_0 is the initial QD radius. N_0 was determined from the absolute absorbance of a purified nanocrystal sample prior to dissolution (see inset in Figure 1a), using the method described by Peng and co-workers[35] An alternative form of the rate equation can be formulated by experimentally evaluating the final QD equilibrium radius, r_{eq} (the stable QD size reached at long times) and expressing eq 3 as

$$\left(\frac{1}{N_0}\right)\frac{dr(t)}{dt} = k_g\frac{1}{V_u}\left(\frac{4\pi}{3}\right)[r_{eq}^3 - r(t)^3] \quad (4)$$

This approach provides a rate equation in which the growth rate constant is the only unknown because the dissolution rate constant is embedded into the experimentally determined equilibrium radius. Equation 4 is analogous to a rate equation derived by Bullen and Mulvaney to determine the growth kinetic parameter of high-temperature synthesis by estimating a critical radius for nucleation.[10,27] While this one-parameter rate equation makes the modeling procedure less computationally intensive, the results strongly depend on how well the equilibrium radius can be estimated. Figure 2a shows results with fits using both eq 3 and eq 4 for a dissolution study at 180 °C. Although both functions give an overall reasonable agreement between fitted and measured results, eq 3 gives a significantly better fit at shorter times, the region most critical for understanding the dynamic behavior of this system. Therefore, the rate equation given in eq 3 was used to model all data in this work and evaluate temperature-dependent rate constants of growth and dissolution.

Fitting the experimental data shown in Figure 2a with rate eq 3 yields rate constants of growth and dissolution of 36 ± 2 M^{-1} nm^{-2} s^{-1} and 0.049 ± 0.003 nm^{-2} s^{-1}, respectively, at 180 °C. The uncertainty values were propagated from the variability of

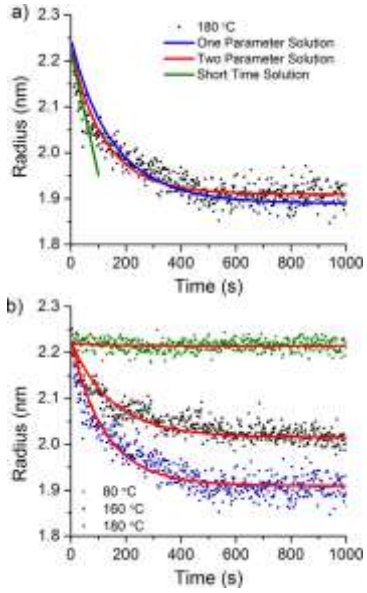

Figure 2. Experimentally measured and modeled temporal evolution of the radius of CdSe nanocrystal quantum dots during dissolution at various temperatures. a) Experimental radius data (black dots) for dissolution at 180 °C compared to modeled size evolution using the two-parameter differential eq 3 (red curve), the one-parameter differential eq 4 (blue curve), and the dissolution-only solution from the short-term dissolution term of eq 3 (green line). (b) Experimental radius data for dissolution experiments at 80 °C (green squares), 160 °C (black triangles), and 180 °C (dark blue squares). The modeled size evolution curves using the two-parameter differential eq 3 are overlaid for each temperature. The 80 °C curve does not exhibit significant decay behavior and was not used for subsequent thermodynamic analysis.

the collective radii measurements, which followed a normal distribution around the optimized model. This approach is needed since the thermodynamic parameters are obtained from the time series of wavelength position data points relative to each other (Figure 2b), and not from an individual wavelength position measurement. A detailed description of this method including error analysis is provided in Supporting Information. At very early stages of the experiments, the monomer concentration in solution is close to zero and $r(t)$ is close to r_0. Equation 3 is thus dominated by the dissolution rate term and the QD size evolution should approximate a purely kinetic-driven dissolution process. A comparison of the linear dissolution rate function with the experimental data is given in Figure 2a and confirms this behavior up to 60 s. In this initial period, about 30 [CdSe] monomers per QD detach from the surface every 10 s.

A critical assumption of the model rate eq 3 is that the system reaches a dissolution/growth equilibrium; i.e., the leveling of the QD radius and monomer concentration curves in Figure 1c are the result of a reaction equilibrium described in eq 1 and is not influenced by monomer diffusion into the bulk solution. In our experimental setup, QDs are placed into pure solvent. Therefore, [CdSe] monomers detaching from the QD surface via dissolution have two possible fates: transport into the bulk solution or reattachment back to the QD surface via growth following eq 1. To evaluate which process is controlling

DOI: 10.1021/acs.chemmater.6b00878
Chem. Mater. 2016, 28, 3831−3838

the steady-state behavior of the QDs at long times, the dimensionless Damköhler parameter, *Da*, defined as

$$Da = \frac{\text{rate of reaction}}{\text{rate of mass transport}} = \frac{k_d}{k'} \quad (5)$$

was determined. The rate constant k' in eq 5 is the mass transfer coefficient of $[CdSe]_t$ monomers at time t through an infinitesimal shell of area $A(t)$ surrounding a QD until an equilibrium number of monomers $[CdSe]_{eq}$ is reached. The outward flux of [CdSe] is then given as

$$\frac{d}{dt}[CdSe] = k'([CdSe]_t - [CdSe]_{eq})A(t) \quad (6)$$

The solution-phase concentrations $[CdSe]_t$ and $[CdSe]_{eq}$ for each experiment were calculated from the loss of solid-phase monomers during dissolution, shown in Figure 2C. The mass transfer coefficient for each experiment was then determined by optimizing k' in eq 6 using Matlab (see Supporting Information, Figure S2). Analysis of the experimental data at 180 °C yields a Damköhler parameter of 550. This clearly indicates that transport of the monomers through the near-surface film is negligible and that growth and dissolution at the QD-solution interface are the primary source of monomers in solution.

Next, the temperature dependence of the rate constants was investigated. Dissolution experiments were conducted using the same set of QDs at 160, 140, 120, 100, and 80 °C. Figure 2b summarizes the experimentally observed size evolution of the QDs and the fitted rate equation graphs. Experiments in the temperature range 80−180 °C were also performed for QDs with different initial diameters (see Supporting Information, Figure S8). Several general observations are noteworthy: (1) The Damköhler parameter ranges between 30 and 550 with a clear upward trend with increasing temperature (see Supporting Information, Figure S3). For example, even at a reaction temperature of 80 °C, the reaction rate is ~30 times higher than the rate of mass transfer away from the surface. (2) Both the rate of dissolution and the new equilibrium radius of QDs depend strongly on temperature: the higher the temperature, the higher the initial rate of dissolution and the smaller the final equilibrium radius. (3) At 80 and 100 °C, the observed decrease in QD size was smaller than the uncertainty of the data set and it was impossible to derive meaningful rate constant values. (4) At temperatures higher than 100 °C, the rate constants of growth and dissolution both increase with increasing temperature. There is a significantly larger increase of the dissolution rate constant (see Figure 3).

The set of calculated temperature-dependent rate constants can be used in Arrhenius plot analyses to evaluate activation energies (Figure 3). The fitted values for the activation energy of growth and dissolution are 14 ± 6 kJ mol^{-1} and 27 ± 8 kJ mol^{-1}, respectively. The significantly higher activation barrier for dissolution, combined with the observed low reaction rates at temperatures below 80 °C, is also the reason for the observed stable shelf life of commercially available QDs.

The results of these kinetic studies provide a basis for determining the thermodynamic properties of CdSe QD growth and dissolution. The equilibrium constant, K_{eq}, for eq 1 is given by the ratio of the rate constants for growth and dissolution. Therefore, the evaluated rate constants can be used to calculate temperature-dependent equilibrium constants. As shown in Figure 4, the equilibrium constant decreases with

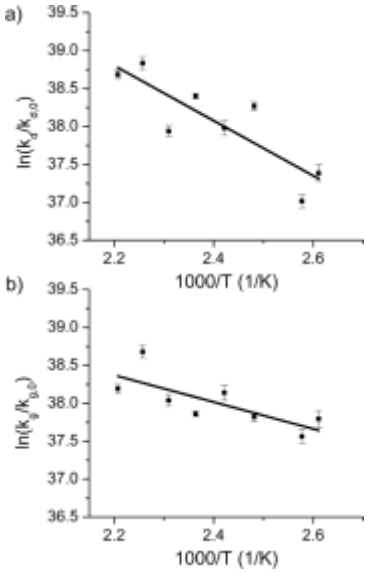

Figure 3. Linearized Arrhenius plots for CdSe nanocrystal quantum dot dissolution (a) and growth (b). Experimental data in the temperature range 110−180 °C were used for the fitting procedure. Uncertainties represent the stability of the modeling solutions upon variation of input parameters. The lines in panels a and b give the best linear least-squares fits to the data (see Supporting Information) and were used to determine the activation energies for nanocrystal dissolution and growth, respectively. Reference states for rate constants k_d and k_g were 1 m^{-2} s^{-1} and 1 mol^{-1} m s^{-1}, respectively.

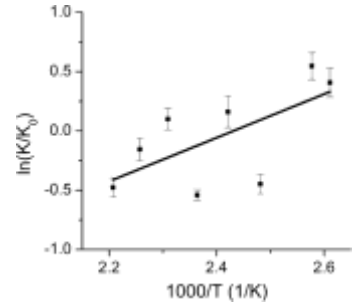

Figure 4. Linearized van't Hoff plot for CdSe nanocrystal quantum dots. The linearized van't Hoff plot is shown for the growth direction of the reaction given in eq 1 with $K_{eq} = k_g k_d^{-1}$ and a reference state K_0 of 1 m^3 mol^{-1}. The line represents the best linear least-squares fit of data in the temperature range of 110−180 °C (see Supporting Information), and was used to determine the reaction enthalpy and entropy for the nanocrystal growth reaction given in eq 1. The error bars are propagated uncertainties from the rate constant data for growth and dissolution.

increased temperature. This finding indicates that the nanocrystal growth reaction is an exothermic process. By fitting the K_{eq} data set (using a K_0 standard state of 1 m^3 mol^{-1}) to the linearized van't Hoff equation, the reaction enthalpy, ΔH, for the growth process was calculated to be −15 ± 7 kJ mol^{-1}, and a reaction entropy, ΔS, of −37 ± 18 J K^{-1} mol^{-1} was obtained.

These results reveal a negative Gibbs free energy for the growth process at temperatures below 135 °C. Thus, wurtzite

DOI: 10.1021/acs.chemmater.6b00878
Chem. Mater. 2016, 28, 3831−3838

CdSe nanocrystal growth is thermodynamically favored at low temperatures, whereas dissolution becomes the spontaneous process at elevated temperatures. This finding seems surprising initially given that most wurtzite CdSe nanocrystal synthesis methods successfully operate at temperatures above 200 °C.[6−11] In contrast, cubic zincblende QDs can be synthesized at lower temperatures.[37,38] However, it is important to consider both thermodynamic and kinetic parameters. From the wide range of reaction parameters (types of molecular precursors, functional groups of ligands, reactant concentrations, etc.) that allow successful formation of wurtzite CdSe QDs, it seems the activation energy barrier for growth is readily overcome at elevated temperatures. However, to overcome the thermodynamic barrier and the rapidly increasing rate of dissolution with increasing temperatures (Figure 3a), the growth reaction at high temperatures must be driven by an excess of molecular precursor in solution. This is in agreement with experimental growth studies by Alivisatos and co-workers who reported incomplete precursor conversion at temperatures around 300 °C.[11] In detail, this group found that at these high temperatures CdSe QDs ceased to grow once the amount of precursor units in the growth solution was reduced to around 20% of its original value.[11] Extrapolating the range of equilibrium constants determined in our study to 300 °C, gives an estimated K_{eq} value of ∼0.3 m^3 mol^{-1} (for a K_0 of 1 m^3 mol^{-1}), predicting dissolution to be the rate-dominant process.

On the other hand, our analysis revealed growth is thermodynamically favored at reaction temperatures below 135 °C. We note that our result is very close to computational results from Garcia-Rodriguez and Liu, who identify a temperature of around 140 °C as an important activation range for monomer formation in CdSe nanocrystal synthesis.[39] Our finding is also in close agreement with experimental low-temperature growth studies of high-quality wurtzite CdSe nanocrystal QDs that revealed high conversion within a temperature range of 100−150 °C.[12,13,24] However, in these studies, it was found that, in contrast to high-temperature methods, the reaction parameter window for successful growth of size-monodisperse QDs is very narrow. These findings point to the importance of finding reaction conditions that can lower the steep activation energy barrier of 14 kJ mol^{-1}. In this quest, the choice of organic ligand molecules, which play a key role in QD synthesis by stabilizing precursor molecules and the surface of growing nanocrystals in solution, was found critical. In particular, amine-based primary ligands seem to be the best barrier-lowering candidates and were reported to give the highest yields of wurtzite CdSe QDs.[12,13]

Amines have previously been described as "activating" ligands aiding in both the nucleation and growth of nanocrystals.[40,41,43] This activity of amine ligands is most likely due to their ability to bind to both precursor species (through direct cadmium−nitrogen interactions or via hydrogen bonding to selenium) and their ability to readily adsorb to the QD surface. Although the unique role of amine ligands in low-temperature synthesis was found by screening a large number of ligands,[12] our approach enables a systematic investigation of ligands and their catalytic ability simply by studying nanocrystal dissolution as a function of ligand concentration and type. The latter is of particular interest as it was experimentally found that even small changes in the alkyl chain length of amine and carboxylic acid ligands can have profound impact on the growth kinetics.[12] Moreover, Rempel et al. derived a model that relates rate constants of growth and dissolution to the equilibrium constant for ligand binding to the nanocrystals and the ligand concentration (eqs 3 and 4 in ref 29). Direct measurements of ligand−nanocrystal interactions are extremely difficult, especially for solution systems. We therefore anticipate our indirect method of dissolution and growth rate evaluation to be of great value for future studies of ligand−nanocrystal interactions and ligand binding affinities.

■ CONCLUSIONS

In summary, we developed a reaction equilibrium-based method to derive key kinetic and thermodynamic quantities for growth and dissolution of colloidal nanocrystals. Our method is fast, simple, and versatile because it uses *in situ* optical absorption spectroscopy. Using wurtzite CdSe nanocrystal QDs as a model system, we demonstrated that simple dissolution studies could be used to derive rate constants, activation barriers, equilibrium constants, and reaction enthalpies and entropies. Because of its simplicity, our method can be readily extended to any nanocrystalline system with size-dependent optical properties. Examples include different II-VI and III-V semiconductor nanocrystals, and metallic nanocrystals with plasmonic extinction features. We anticipate that building a database of kinetic and thermodynamic quantities for nanocrystal growth in the presence of different ligands, coligands, and precursor species will transform nanocrystal synthesis from a trial-and-error method to directed industrial-scale design of nanocrystalline materials with defined shapes such as rods, wires, and platelets.

■ ASSOCIATED CONTENT

Supporting Information

The Supporting Information is available free of charge on the ACS Publications website at DOI: 10.1021/acs.chemmater.6b00878.

Method for evaluation of Varshni coefficients; temperature-dependent Damköhler parameters; determination of excitonic wavelength position; error analysis and propagation method; details on linear least-squares fitting procedure; complete set of temperature-dependent dissolution graphs; nanocrystal concentration profiles during dissolution (PDF).

■ AUTHOR INFORMATION

Corresponding Authors

*E-mail: michael.bartl@utah.edu (M.H.B.).
*E-mail: j.siy@navillum.com (J.T.S.).

Author Contributions

⊥These authors contributed equally to this work.

Notes

The authors declare the following competing financial interest(s): Jacqueline Siy is president of Navillum Nanotechnologies, LLC, which licensed part of the technology described in this paper. Michael Bartl is a scientific consultant for Navillum Nanotechnologies, LLC.

■ ACKNOWLEDGMENTS

We thank Peter Rose, Terry Ring, and Larry Thorne for helpful discussions. This work was supported in part by the U.S. Department of Energy, the Energy & Geoscience Institute at the University of Utah, a Scialog grant by the research Corporation for Science Advancement, and technology

commercialization grants from the University of Utah and the State of Utah.

REFERENCES

(1) Brus, L. E. Electron-electron and electron-hole interactions in small semiconductor crystallites - the size dependence of the lowest excited electronic state. *J. Chem. Phys.* **1984**, *80*, 4403−4409.
(2) Bawendi, M. G.; Steigerwald, M. L.; Brus, L. E. The quantum mechanics of larger semiconductor clusters ("quantum dots"). *Annu. Rev. Phys. Chem.* **1990**, *41*, 477−496.
(3) Alivisatos, A. P. Perspectives on the physical chemistry of semiconductor nanocrystals. *J. Phys. Chem.* **1996**, *100*, 13226−13239.
(4) Nirmal, M.; Brus, L. Luminescence photophysics in semiconductor nanocrystals. *Acc. Chem. Res.* **1999**, *32*, 407−414.
(5) Hendricks, M. P.; Campos, M. P.; Cleveland, G. T.; Jen-La Plante, I.; Owen, J. S. A tunable library of substituted thiourea precursors to metal sulfide nanocrystals. *Science* **2015**, *348*, 1226−1230.
(6) Murray, C. B.; Norris, D. J.; Bawendi, M. G. Synthesis and characterization of nearly monodisperse CdE (E = S, Se, Te) semiconductor nanocrystallites. *J. Am. Chem. Soc.* **1993**, *115*, 8706−8715.
(7) Hines, M. A.; Guyot-Sionnest, P. Bright UV-blue luminescent colloidal ZnSe nanocrystals. *J. Phys. Chem. B* **1998**, *102*, 3655−3657.
(8) Peng, Z. A.; Peng, X. Nearly monodisperse and shape-controlled CdSe nanocrystals via alternative routes: Nucleation and growth. *J. Am. Chem. Soc.* **2002**, *124*, 3343−3353.
(9) Cumberland, S. L.; Hanif, K. M.; Javier, J.; Khitrov, G. A.; Strouse, G. F.; Woessner, S. M.; Yun, C. S. Inorganic clusters as single source precursors for preparation of CdSe, ZnSe, CdSe/ZnS nanomaterials. *Chem. Mater.* **2002**, *14*, 1576−1584.
(10) Bullen, C. R.; Mulvaney, P. Nucleation and growth kinetics of CdSe nanocrystals in octadecene. *Nano Lett.* **2004**, *4*, 2303−2307.
(11) Liu, H.; Owen, J. S.; Alivisatos, A. P. Mechanistic study of precursor evolution in colloidal group II-VI semiconductor nanocrystal synthesis. *J. Am. Chem. Soc.* **2007**, *129*, 305−312.
(12) Siy, J. T.; Brauser, E. H.; Thompson, T. K.; Bartl, M. H. Synthesis of bright CdSe nanocrystals by optimization of low-temperature reaction parameters. *J. Mater. Chem. C* **2014**, *2*, 675−682.
(13) Siy, J. T.; Brauser, E. H.; Bartl, M. H. Low-temperature synthesis of colloidal CdSe nanocrystal quantum dots. *Chem. Commun.* **2011**, *47*, 364−366.
(14) Wood, V.; Panzer, M. J.; Caruge, J.; Halpert, J. E.; Bawendi, M. G.; Bulovic, V. Air-stable operation of transparent, colloidal quantum dot based LEDs with a unipolar device architecture. *Nano Lett.* **2010**, *10*, 24−29.
(15) Talapin, D. V.; Steckel, J. Quantum dot light-emitting devices. *MRS Bull.* **2013**, *38*, 685−691.
(16) Klimov, V. I.; Ivanov, S. A.; Nanda, J.; Achermann, M.; Bezel, I.; McGuire, J. A.; Piryatinski, A. Single-exciton optical gain in semiconductor nanocrystals. *Nature* **2007**, *447*, 441−446.
(17) Tessler, N.; Medvedev, V.; Kazes, M.; Kan, S.; Banin, U. Efficient near-infrared polymer nanocrystal light-emitting diodes. *Science* **2002**, *295*, 1506−1508.
(18) Stolle, C. J.; Harvey, T. B.; Korgel, B. A. Nanocrystal photovoltaics: a review of recent progress. *Curr. Opin. Chem. Eng.* **2013**, *2*, 160−167.
(19) Milliron, D. J.; Gur, I.; Alivisatos, A. P. Hybrid organic-nanocrystal solar cells. *MRS Bull.* **2005**, *30*, 41−44.
(20) Pelaz, B.; Jaber, S.; de Aberasturi, D. J.; Wulf, V.; Aida, T.; de la Fuente, J. M.; Feldmann, J.; Gaub, H. E.; Josephson, L.; Kagan, C. R.; et al. The state of nanoparticle-based nanoscience and biotechnology: Progress, promises, and challenges. *ACS Nano* **2012**, *6*, 8468−8483.
(21) Alivisatos, A. P.; Gu, W.; Larabell, C. Quantum dots as cellular probes. *Annu. Rev. Biomed. Eng.* **2005**, *7*, 55−76.
(22) Michalet, X.; Pinaud, F. F.; Bentolila, L. A.; Tsay, J. M.; Doose, S.; Li, J. J.; Sundaresan, G.; Wu, A. M.; Gambhir, S. S.; Weiss, S. Quantum dots for live cells, in vivo imaging, and diagnostics. *Science* **2005**, *307*, 538−544.
(23) Markets and Markets. *Quantum Dot Market by Product, Material, Application, and Geography- Forecast up to 2020.* http://www.marketsandmarkets.com/Market-Reports/quantum-dots-qd-market-694.html.
(24) Yu, K.; Hu, M. Z.; Wu, R.; Piolet, M. L.; Frotey, M.; Zaman, M. B.; Wu, X.; Leek, D. M.; Tao, Y.; Wilkinson, D.; et al. Thermodynamic equilibrium-driven formation of single-sized nanocrystals: Reaction media tuning CdSe magic-sized versus regular quantum dots. *J. Phys. Chem. C* **2010**, *114*, 3329−3339.
(25) Kudera, S.; Zanella, M.; Giannini, C.; Rizzo, A.; Li, Y.; Gigli, G.; Cingolani, R.; Ciccarella, G.; Spahl, W.; Parak, W. J.; Manna, L. Sequential growth of magic-size CdSe nanocrystals. *Adv. Mater.* **2007**, *19*, 548−552.
(26) Sowers, K. L.; Swartz, B.; Krauss, T. D. Chemical mechanisms of semiconductor nanocrystal synthesis. *Chem. Mater.* **2013**, *25*, 1351−1362.
(27) Chuang, X.; Hongxun, H.; Wei, C.; Jingkang, W. Crystallization kinetics of CdSe nanocrystals synthesized via the TOP−TOPO−HDA route. *J. Cryst. Growth* **2008**, *310*, 3504−3507.
(28) Siy, J. T.; Bartl, M. H. Insights into Reversible Dissolution of Colloidal CdSe Nanocrystal Quantum Dots. *Chem. Mater.* **2010**, *22*, 5973−5982.
(29) Rempel, J. Y.; Bawendi, M. G.; Jensen, K. F. Insights into the Kinetics of Semiconductor Nanocrystal Nucleation and Growth. *J. Am. Chem. Soc.* **2009**, *131*, 4479−4489.
(30) Qu, L.; Yu, W. W.; Peng, X. In Situ Observation of the Nucleation and Growth of CdSe Nanocrystals. *Nano Lett.* **2004**, *4*, 465−469.
(31) Schikora, D.; Schwedhelm, S.; Kudryashov, I.; Lischka, K.; Litvinov, D.; Rosenauer, A.; et al. Investigations on the formation kinetics of CdSe quantum dots. *J. Cryst. Growth* **2000**, *214−215*, 698−702.
(32) Dickerson, B. D.; Irving, D. M.; Herz, E.; Claus, R. O.; Spillman, W. B.; Meissner, K. E. Synthesis kinetics of CdSe quantum dots in trioctylphosphine oxide and in stearic acid. *Appl. Phys. Lett.* **2005**, *86*, 171915.
(33) Park, J.; Lee, K. H.; Galloway, J. F.; Searson, P. C. Synthesis of Cadmium Selenide Quantum Dots from a Non-Coordinating Solvent: Growth Kinetics and Particle Size Distribution. *J. Phys. Chem. C* **2008**, *112*, 17849−17854.
(34) Peng, X.; Wickham, J.; Alivisatos, A. P. Kinetics of II-IV and III-V Colloidal Semiconductor Nanocrystal Growth: "Focusing" of Size Distributions. *J. Am. Chem. Soc.* **1998**, *120*, 5343−5344.
(35) Yu, W. W.; Qu, L.; Guo, W.; Peng, X. Experimental Determination of the Extinction Coefficient of CdTe, CdSe, and CdS Nanocrystals. *Chem. Mater.* **2003**, *15*, 2854−2860.
(36) Varshni, Y. P. Temperature dependence of the energy gap in semiconductors. *Physica* **1967**, *34*, 149−154.
(37) Talapin, D. V.; Nelson, J. H.; Shevchenko, E. V.; Aloni, S.; Sadtler, B.; Alivisatos, A. P. Seeded Growth of Highly Luminescent CdSe/CdS Nanoheterostructures with Rod and Tetrapod Morphologies. *Nano Lett.* **2007**, *7*, 2951−2959.
(38) Al-Salim, N.; Young, A. G.; Tilley, R. D.; McQuillan, A. J.; Xia, J. Synthesis of CdSeS Nanocrystals in Coordinating and Noncoordinating Solvents: Solvent's Role in Evolution of the Optical and Structural Properties. *Chem. Mater.* **2007**, *19*, 5185−5193.
(39) Garcia-Rodriguez, R.; Liu, H. Mechanistic Study of the Synthesis of CdSe Nanocrystals: Release of Selenium. *J. Am. Chem. Soc.* **2012**, *134*, 1400−1403.
(40) Pradhan, N.; Reifsnyder, D.; Xie, R.; Aldana, J.; Peng, X. Surface Ligand Dynamics in Growth of Nanocrystals. *J. Am. Chem. Soc.* **2007**, *129*, 9500−9509.
(41) Sun, Z. H.; Oyanagi, H.; Nakamura, H.; Jiang, Y.; Zhang, L.; Uehara, M.; Yamashita, K.; Fukano, A.; Maeda, H. Ligand Effects of Amine on the Initial Nucleation and Growth Processes of CdSe Nanocrystals. *J. Phys. Chem. C* **2010**, *114*, 10126−10131.
(42) Qu, L.; Peng, Z. A.; Peng, X. Alternative Routes Toward High Quality CdSe Nanocrystals. *Nano Lett.* **2001**, *1*, 333−337.

DOI: 10.1021/acs.chemmater.6b00878
Chem. Mater. 2016, 28, 3831−3838

(43) Garcia-Rodriguez, R.; Liu, H. Mechanistic Insights into the Role of Alkylamine in the Synthesis of CdSe Nanocrystals. *J. Am. Chem. Soc.* **2014**, *136*, 1968−1975.

DOI: 10.1021/acs.chemmater.6b00878
Chem. Mater. 2016, 28, 3831−3838

Supporting Information

Experimental Evaluation of Kinetic and Thermodynamic Reaction Parameters of Colloidal Nanocrystals

Eric M. Brauser[1,2#], Trevor D. Hull[1#], John D. McLennan[2], Jacqueline T. Siy[3]* and Michael H. Bartl[1]*

[1]*Department of Chemistry, University of Utah, Salt Lake City, UT, 84112, USA*

[2]*Department of Chemical Engineering, University of Utah, Salt Lake City, UT, 84112, USA*

[3]*Navillum Nanotechnologies, LLC, South Salt Lake, UT 84115, USA*

[#]*These authors contributed equally to this work.*

**Corresponding authors: michael.bartl@utah.edu (MHB), j.siy@navillum.com (JTS)*

1. Varshni Coefficients

Over the past two decades, the study of QD optical properties and their dependence upon crystal size have been extensively documented. Previous studies of bulk semiconductor materials and semiconductor nanoparticles have investigated the effect of temperature on the energy band gap. Through Varshni's relationship between the ground-state band gap and the effect of temperature on both crystal expansion and electron-phonon coupling, the characteristic energy which the QDs absorbs at room temperature can be extrapolated from observed measurements at elevated temperatures. In order to obtain accurate kinetic size data for each temperature, the measured absorption wavelength of the QD sample at room temperature was used with the first observed absorption wavelength of the kinetic study at elevated temperature. The value for the temperature coefficient α was then determined by fitting the Varshni equation with values of α and β. This reflects the temperature-dependent effects on the crystal structure that has been investigated and reported previously.[S1-S10]

\

Real time measurement of the mean QD size using an in-situ absorbance cell allows for time-accurate readings of the primary absorbance peak, and the corresponding size. With correction by the Varshni equation, a ground-state bandgap can be calculated, correcting for the observed wavelengths' dependence on temperature.[S11]

$$E_g(T) = E_0 - \frac{\alpha T^2}{T+\beta} \quad \text{(S1)}$$

The temperature coefficient α was calculated by fitting the Varshni equation for the bandgap shift at each elevated temperature. The measured room temperature (25 C) bandgap energy was 2.05 eV which was translated to a nanocrystal radius of 2.36 nm using the empirical relationship developed by Yu. et. al, shown in (4).[S12]

$$D = (1.6122 * 10^{-9})\lambda^4 - (2.6575 * 10^{-6})\lambda^3 + (1.6242 * 10^{-3})\lambda^2 - (0.4277)\lambda + 41.57 \quad \text{(S2)}$$

The band gap energy for the initial point observed during each separate experiment was then input into the Varshni equation and, with input of the room temperature band gap energy and a slight rearrangement, provides a term with parameters α and β. Both parameters were optimized such that the ΔE term was minimized which provided a matrix of values. This matrix was then compared to literature values for validation. Figure S1 shows calculated results for α, calculated for a single β.

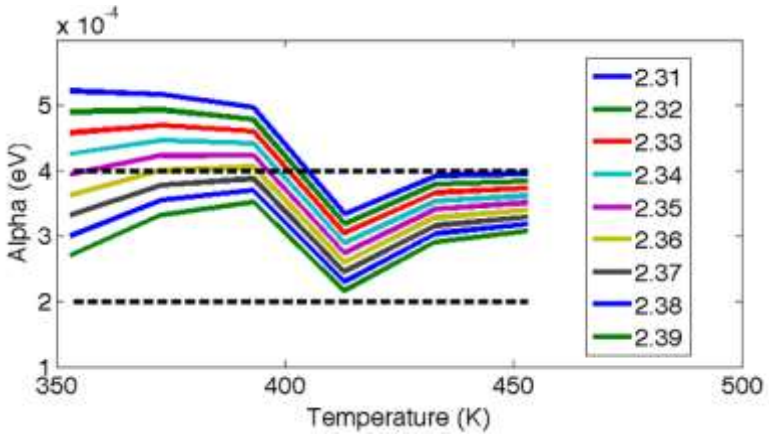

Figure S1: Alpha calculations for a range of potential room temperature radii.

Changing β values within the range of reported literature values was observed to have very little impact on the minimization of ΔE, so a value was chosen from Diroll et. al. that used similar components of study (CdSe/CdS).[S4] Note that the band gap shift in the Varshni equation is dependent on the input radius (corresponding to a bandgap energy and wavelength) and this radius has its own uncertainty. This necessitates that a range of initial radii r_o need to be tested in the model in order to reflect possible "true" value of the radius. The dotted lines reflect high and low values of α for similar systems that have been reported in the literature.[S1,S6] As the temperature increases for each experiment, the calculated α decreases, which reveals the temperature dependence of α. This is in agreement with reports that studied the effects of temperature variation on α for various semiconductor materials.[S1,S2,S4,S6] Therefore, a matrix of α values over the temperature range will be used to shift the observed radius for each experiment (as each experiment reflects dissolution at a different temperature). It is clear that as the input radius decreases, α increases beyond previously reported values across the temperature range. This reflects the inconsistency in trying to model parameters without constraining them within their physical meaning i.e. an unreasonable value for α would be required to reconcile an input radius of 2.31 or 2.38 nm with the observed initial radius. The dip in α at the 413 K mark is due to the initial observed radius at this temperature being smaller (larger bandgap energy) than the experiments at 393 or 423 K.

The overall trend however is a decrease in α across the temperature measurements. The α values for an input radius of 2.34 nm are near the reported literature values at low temperatures, and within the bounds at higher temperatures, in addition to showing minimal upward or downward trends. This radius is closest to that calculated from the QD sample absorption maxima wavelength at 602 nm calculated from (S2). For these reasons, the α values obtained from an input QD radius of 2.34 nm are shown in Table S1 and will be used for shifting the experimental data to reflect room temperature measurements.

Table S1: Modeled values of α across a range of QD dissolution temperatures

Temp (°C)	80	100	120	140	160	180
α (eV/K E-4)	4.260	4.463	4.418	2.891	3.537	3.618

The Varshni correction method was also verified by quenching aliquots of QD samples from a given high-temperature treatment to room temperature. An absorbance spectrum was then taken at room temperature and the QD radius calculated from the wavelength position of the first excitonic absorption feature (as described above). The results were in agreement with Varshni-corrected high-temperature measurements of the same sample.

2. Damköhler Parameters

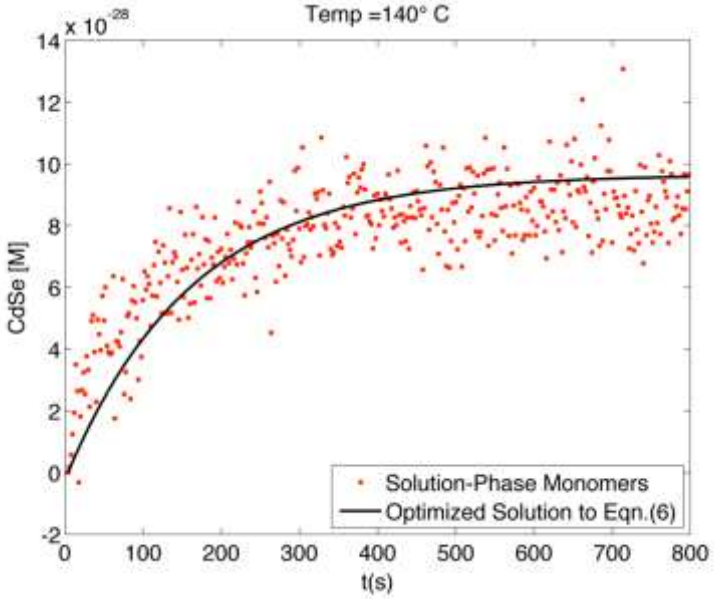

Figure S2: Example evolution of monomer concentration over time at 140 °C with optimized solution to equation (6), solving for mass transfer coefficient *k'*. The monomer concentration was determined by the transfer of material from the solid to solution phase, calculated from the change in particle size.

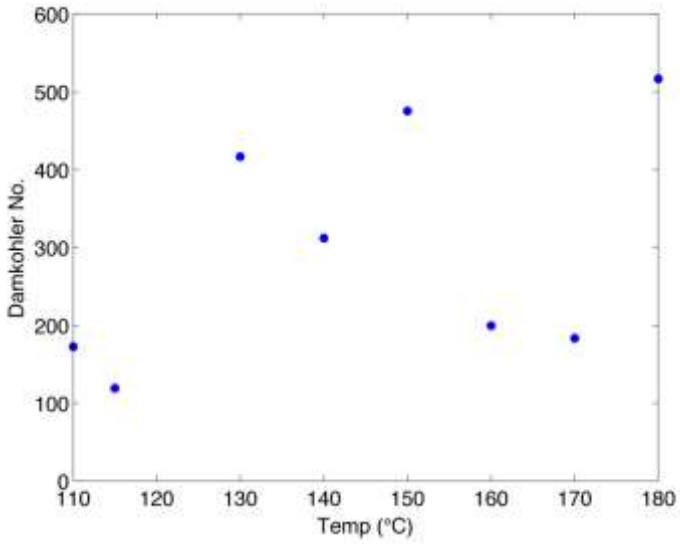

Figure S3: Plot of Damköhler parameter with temperature

3. Location of Characteristic Excitonic Wavelength Position

The characteristic excitonic wavelength position was necessary to identify in order to obtain the mean QD radius from equation (S2). The QD solutions that were analyzed had low concentrations that resulted in non-ideal definition of the characteristic peak. Post-processing of the absorbance spectra was performed to improve the accuracy of locating the characteristic wavelength. A baseline following a fourth order polynomial was established to correct for scattering (Fig S4a). This baseline was only dependent upon the wavelength position, and therefore identical in shape between experiments. The baseline was subtracted from the experimental data, which was then fit to a Gaussian distribution (Figs. S4b and S4c). The center of this peak was used in equation S2 to determine the mean QD radius for subsequent time-series analysis. It is evident that this method provides a distinct peak and even with the poor resolution of the experimental absorbance spectra, the peak location can be confidently obtained. Note that the number of nanocrystals N_0 used in equation (3) is determined prior to dissolution, and the absorbance intensity over the course of the experiment is not a parameter necessary to successfully solve the differential equations.

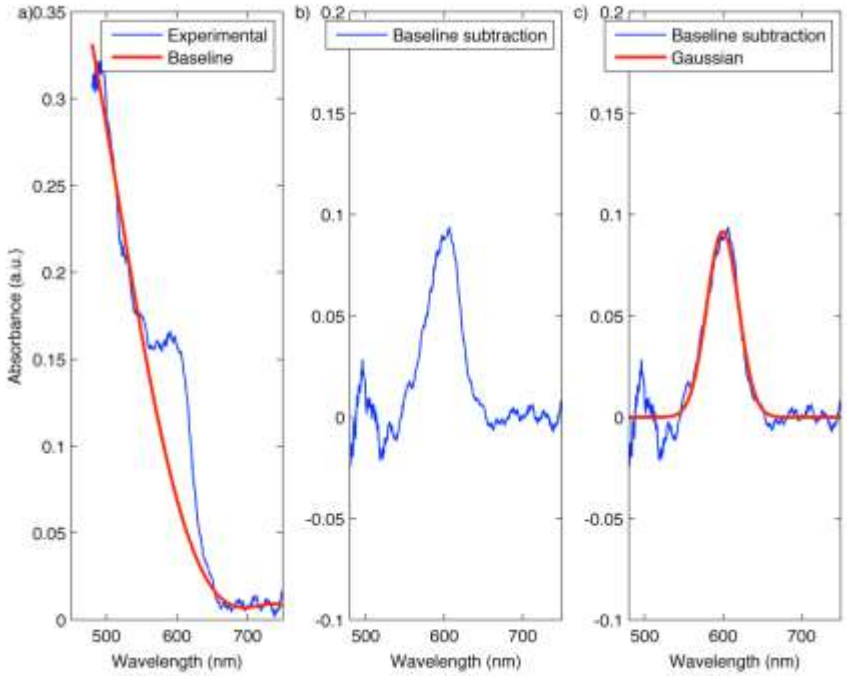

Figure S4: Gaussian distribution analysis of characteristic peak wavelength

4. Error Propagation

We accounted for error through standard error propagation techniques, though the process was non-trivial. As stated in the manuscript, the Varshni equation was used to correct the high-temperature wavelength measurement to the room temperature value so that the temperature dependence would not influence the calculated radius values. This was done as follows:

1) Convert observed wavelengths to eV

$$\frac{\lambda_2}{1240nm} = E_2[eV]$$

2) Use Varshni equation to convert the elevated temperature energy to equivalent room temperature energy

$$E_1 = E_2 + \alpha\left[\frac{T_2^2}{T_2+\beta} - \frac{T_1^2}{T_1+\beta}\right]$$

3) Use convert energy back to wavelength, and subsequently, using the Peng equation to obtain "true" radius

$$\lambda_1 = \frac{1240}{E_1} = 1240 * \left[\frac{\lambda_2}{1240nm} + \alpha\left[\frac{T_2^2}{T_2+\beta} - \frac{T_1^2}{T_1+\beta}\right]\right]^{-1}$$

$$D = (1.6122 * 10^{-9})\lambda^4 - (2.6575 * 10^{-6})\lambda^3 + (1.6242 * 10^{-3})\lambda^2 - (0.4277)\lambda + 41.57$$

$$\begin{aligned} r = \ 0.5 * ((1.6122 * 10^{-9})1240 * & \left[\frac{\lambda_2}{1240nm} + \alpha\left[\frac{T_2^2}{T_2+\beta} - \frac{T_1^2}{T_1+\beta}\right]\right]^{-1^4} \\ & - (2.6575 * 10^{-6})1240 * \left[\frac{\lambda_2}{1240nm} + \alpha\left[\frac{T_2^2}{T_2+\beta} - \frac{T_1^2}{T_1+\beta}\right]\right]^{-1^3} \\ & + (1.6242 * 10^{-3})1240 * \left[\frac{\lambda_2}{1240nm} + \alpha\left[\frac{T_2^2}{T_2+\beta} - \frac{T_1^2}{T_1+\beta}\right]\right]^{-1^2} \\ & - (0.4277)1240 * \left[\frac{\lambda_2}{1240nm} + \alpha\left[\frac{T_2^2}{T_2+\beta} - \frac{T_1^2}{T_1+\beta}\right]\right]^{-1} + 41.57) \end{aligned}$$

4) Now, error in radius can be determined via propagation:
   $r = f(\lambda, T_1, T_2, \alpha, \beta)$, and

$$\delta r = \left[\left(\frac{\partial r}{\partial T_1}\delta T_1\right)^2 + \left(\frac{\partial r}{\partial T_2}\delta T_2\right)^2 + \left(\frac{\partial r}{\partial \lambda}\delta\lambda\right)^2 + \left(\frac{\partial r}{\partial \alpha}\delta\alpha\right)^2 + \left(\frac{\partial r}{\partial \beta}\delta\beta\right)^2\right]^{0.5}$$

This process rigorously calculates the error of the room temperature from measured values (temperature, wavelength) or uncertainty from earlier models (Varshni parameters). The uncertainty of the absorbance peak wavelength λ is obtained from a Gaussian fit and accounts for the distribution of the QDs that contribute to the absorbance.

We found in this analysis that the error bars of the radii were quite large. For all except the highest temperatures, the error was greater than the radius shift from r_0 to r_{eq}. Two examples, 160 and 180 °C, are shown below:

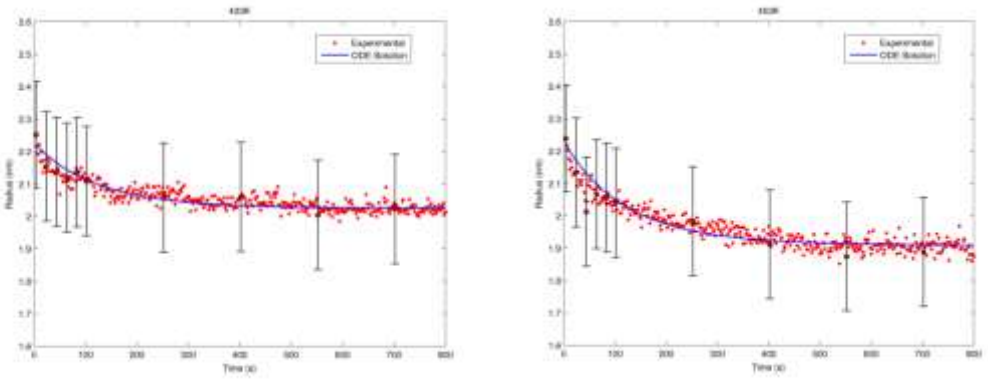

Figure S5: Data and ODE solutions from experiments conducted at 160 and 180 °C, with black error bars determined by error propagation from individual uncertainty measurements

Clearly, even at the second-highest temperature, the initial radius is still within the uncertainty of the equilibrium radius. This method only takes into account the overall uncertainty of making a single measurement of the radius at elevated temperature, i.e. it is the overall uncertainty of the

measurement technique. This is clear from the same values of uncertainty across the entire time range. To correct for this, the residuals from the model value were analyzed. The residuals for two experiments: 120 and 160 °C, with dotted lines showing Gaussian 95% confidence, are below:

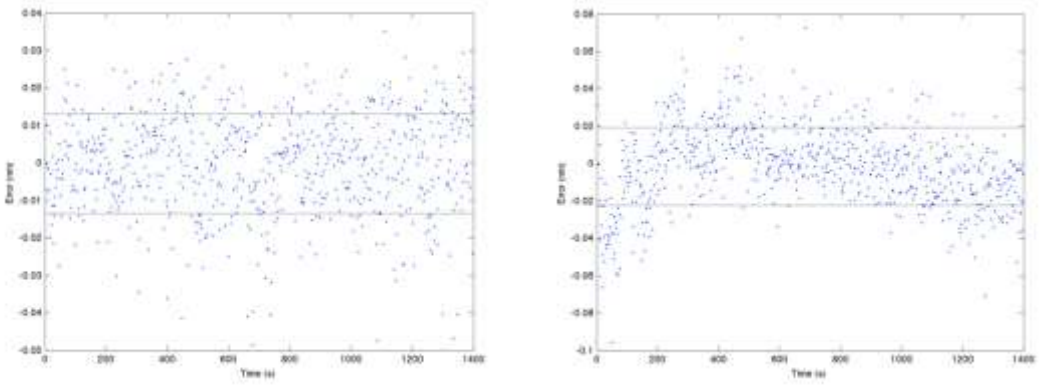

Figure S6: Time-resolved residuals of the solution set to the experimental data (blue dots). The black lines indicate the 95% confidence interval

At lower temperatures the residuals exhibit normal distribution. At high temperatures the errors are not normally distributed, because the short time solution changes rapidly. However the equilibrium distribution of residuals approaches a normal distribution, and is distorted by the inherent inability of a model to account fully for both short-time and long-time solutions. With these results, the variability of one observed radius value to a radius value at a previous time point is determined using the 95% confidence of the residuals. Subsequently, the error bars of the two temperature experiments are shown below:

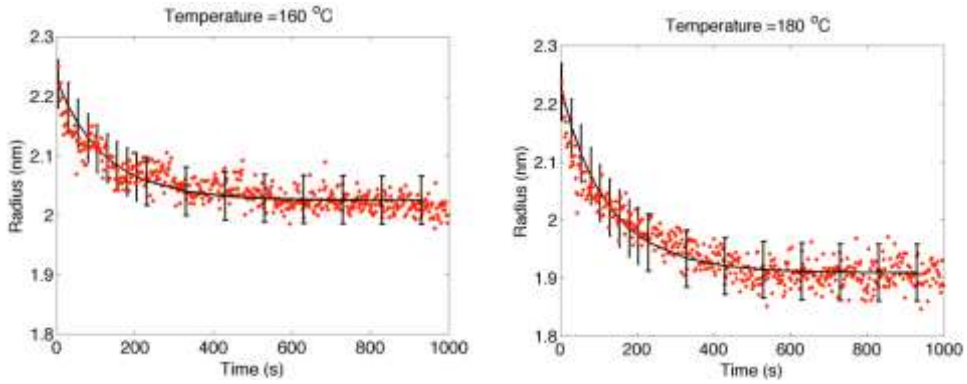

Figure S7: Data and ODE solutions from experiments conducted at 160 and 180 °C (red dots), with black error bars determined by the standard deviation of measurement variation from a previous point

Now, the initial radius is significantly different than those further in time at approximately 20-40 seconds for 180 °C. Even at the lower temperature the initial radius is significantly different as soon as 100 seconds into the experiment. These results support our claim that the error in wavelength measurement and the Peng equation have not been ignored, but the error in the Peng equation is not appropriate for a time series measurement of dynamic nanocrystal size. Error bars for each set of experiments shown in figure 2 have been obtained.

5. Linear Least Squares Fitting

The experimental temperature-dependence data of the rate constants (growth and dissolution) and of the equilibrium constant were fitted to linearized Arrhenius and van't Hoff functions, respectively. It is important to note that uncertainties of measured data (e.g., readout of nanocrystal absorption wavelength position and absorbance, wavelength-to-radius conversion equation) are the same for the entire data set (all nanocrystal sizes and temperatures) and thus only shift the decay curves up or down (Figure 2 in manuscript). Such a shift, however, has no impact on the fitted rate constants for growth and dissolution. Therefore, uncertainties in the rate constant data result solely from the stability of the modeling solutions upon variation of input parameters and do not represent measured standard deviations.

Two different fitting procedures were performed: simple linear least squares and weighted linear least squares fitting. While the obtained best estimates were within the uncertainty ranges, it should be emphasized that the theory of the weighted linear least squares method is based on the exact knowledge of the weights (defined as the inverse of the standard deviation squared, i.e. the inverse of the variance).[S13] For practical applications, this means that the weighted linear least squares method should only be used if weights can be estimated with high confidence.[S14] Since precise knowledge of experimental weights is missing for our data, the results from simple linear least squares fitting procedure were used for further analysis throughout this work.

6. Complete Experimental Data for Thermodynamic Analysis

The set of experimental data used for thermodynamic analysis, with overlain solutions to equation (3) from the manuscript, is shown below in figure S8. The kinetic parameters that were determined for these experiments were used in the subsequent thermodynamic analysis. Two things to note: 1) The results of the 120 °C experiment were significant outliers and were not considered, and 2) The results from the two 180 °C experiments were averaged for the van't Hoff and Arrhenius plots (Figs. 3 and 4). Experiments conducted at temperatures lower than 110 °C do not exhibit significant size change between initial and equilibrium time, as seen in the 80 °C result in Fig. 2b. The *r(t)* curves of these temperatures are almost flat, preventing the differential equation (3) to be solved properly. Therefore, these experiments were not considered for subsequent analysis and not shown below.

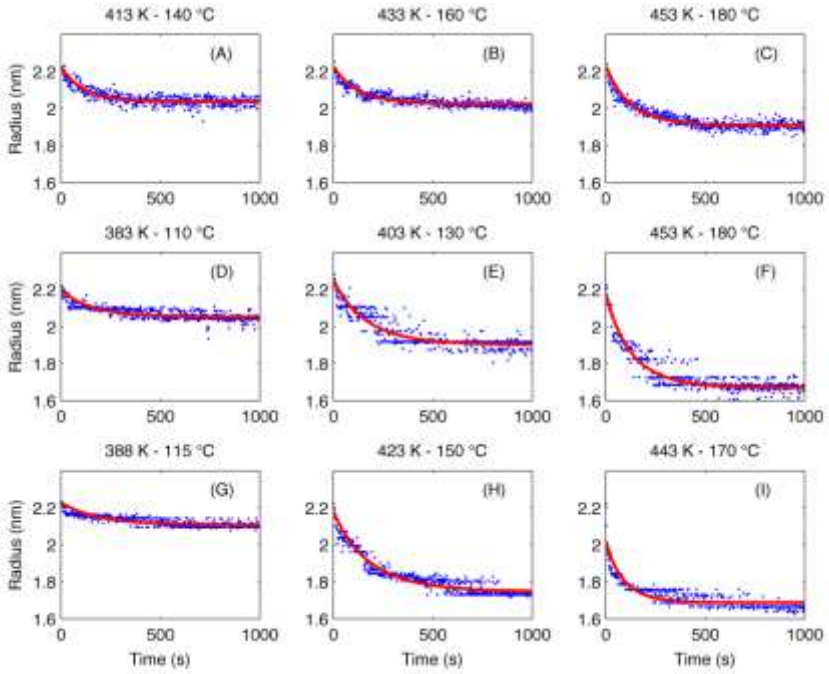

Figure S8: Data (blue circles) and ODE solutions (red lines) from experiments conducted from 110 to 180 °C that were used in the determination of the thermodynamic parameters. The figures are organized by original batch synthesis. Batch 1: figures (A) – (C); Batch 2: figures (D) – (F); Batch 3: figures (G) – (I).

7. Estimated Concentration Profiles for Select Experiments

Concentration values were calculated using the extinction coefficient method outline by Yu et al.[S12] In summary, Yu and coworkers developed an empirical relationship between quantum dot size and absorbance intensity for different materials (CdS, CdSe, CdTe). Figure S9 shows that the particle concentration over the course of the experiments is relatively stable. This an important result that was used to justify the assumption of constant concentration during the development of the governing equations, (3) and (4) in the manuscript.

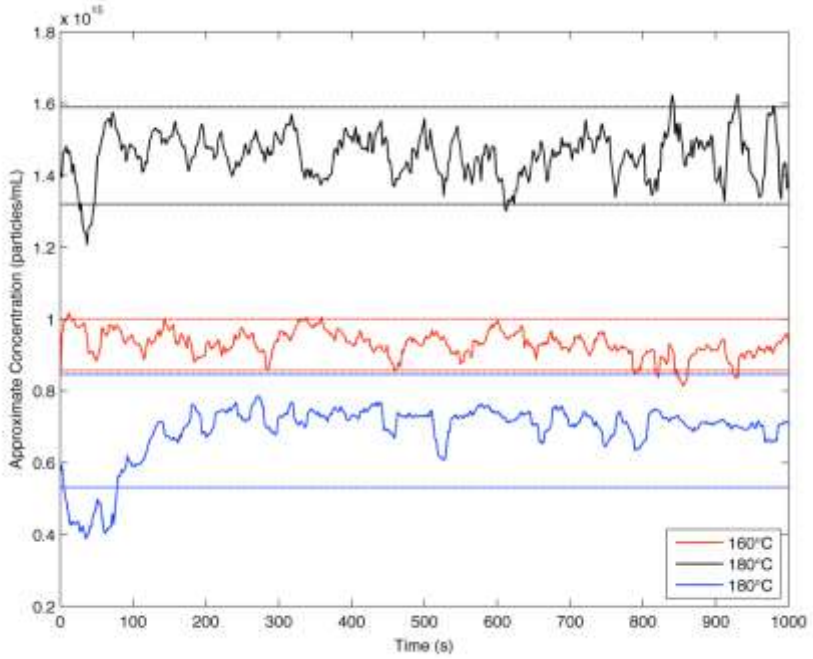

Figure S9: Concentration data calculated for 160 and two 180 °C experiments. Dotted lines indicate the 95% confidence interval.

References - Supporting Information

S1. Cheng, C.; Yan, H. *Physica E* ***2009***, *41*, 828–832.

S2. Yang, P.; Chen, H.-S.; Zhang, S.; Zhao, J.; Du, Y.; Miao, Y.; He, H.; Liu, Y. *RSC Adv.* **2014**, *4*, 43800–43805.

S3. Rowland, C. E.; Schaller, R. D. *J. Phys. Chem. C* **2013**, *117*, 17337–17343.

S4. Diroll, B. T.; Murray, C. B. *ACS Nano* **2014**, *8*, 6466–6474.

S5. Dai, Q.; Song, Y.; Li, D.; Chen, H.; Kan, S.; Zou, B.; Wang, Y.; Deng, Y.; Hou, Y.; Yu, S.; Chen, L.; Liu, B.; Zou, G. *Chem. Phys. Lett.* **2007**, *439*, 65–68.

S6. Valerini, D.; Cretí, A.; Lomascolo, M.; Manna, L.; Cingolani, R.; Anni, M. *Phys. Rev. B* **2005**, *71*, 235409.

S7. Dubiel, M.; Brunsch, S.; Tröger, L. *J. Synchrotron Radiat.* **2001**, *8*, 539–541.

S8. Breivik, M.; Nilsen, T. A.; Fimland, B.-O. *J. Cryst. Growth* **2013**, *381*, 165–168.

S9. Zheng, J.; Cao, S.; Wang, L.; Gao, F.; Wei, G.; Yang, W. *RSC Adv.* **2014**, *4*, 30948–30952.

S10. Iwanaga, H.; Kunishige, A.; Takeuchi, S. *J. Mater. Sci.* **2000**, *35*, 2451–2454.

S11. Varshni, Y. P. *Physica* **1967**, *34*, 149–154.

S12. Yu, W. W.; Qu, L.; Guo, W.; Peng, X. *Chem. Mater.* **2003**, *15*, 2854-2860.

S13. Ryan, T. P. *Modern Regression Methods* (Wiley, New York, 1997, pp. 60-70).

S14. NIST/SEMATECH e-Handbook of Statistical Methods, http://www.itl.nist.gov/div898/handbook/pmd/section1/pmd143.htm

CHAPTER 3

EVALUATION OF KINETIC PARAMETERS OF COLLOIDAL NANOCRYSTALS IN AQUEOUS MEDIA

Introduction to Quantum Dot Aqueous Solubility

Solubility behavior of organic-soluble QDs was shown in Chapter 2 to be influenced by temperature and chemical environment. In the absence of solution-phase monomers, a growth and dissolution-based model could predict the processes' energy barriers. This model system was modified to understand and predict how aqueous-soluble QDs would behave in porous media by creating a system that imitates the fluid phase of the geothermal reservoir pore space, without surface interaction and advection. The ζ-potential has been identified as an important parameter in colloid stability and retention from earlier nanoparticle experiments.[1–8] Dynamic light scattering (DLS) analysis can be performed in order to gain a more comprehensive understanding of the role of ionic strength plays on the stability of the QDs in solution. The charged surfaces of the QDs cause them to move when subjected to an electric field. A laser is initially incident on a static QD sample in solution. When the electric field is applied, the QDs move proportionally to their surface potential, the ζ-potential. This mobility results in small angle scattering of the incident laser and allows the surface potential to be measured. The previous in-situ dissolution work on organic-soluble QDs will provide the basis for measuring how QDs change size in aqueous systems that reflect geothermal

conditions of interest. The results of those experiments will be used to contextualize dynamic QD size behavior in a high temperature aqueous medium.

Experimental Methods

Aqueous solubility

Cadmium selenide core/cadmium sulfide shell QD synthesis and characterization were done based on a modified procedure of Rogach et al.[9] Precursor monomer solutions of cadmium perchlorate and 1-1,dimethylselenourea were rapidly injected into alkaline water in a 1-liter round-bottom flask at 80 °C in the presence of a coordinating ligand (sodium citrate). The core CdSe crystals were allowed to grow for ten minutes before the sulfur source thioacetamide was injected to form a passivating CdS shell (cadmium perchlorate hydrate from Sigma Aldrich, lot # 2189GPJ, no further purification; reagent grade thioacetamide from Sigma Aldrich lot # 00613EJ, no further purification; 1,1-dimethyl-1-selenourea from Sigma Aldrich no further purification; sodium citrate dihydrate from Mallinckrodt, lot # B07627, no further purification). The QD optical properties were characterized using absorbance and fluorescence spectroscopy using a fiber-optic-coupled Ocean Optics USB2000 spectrometer with LS-450 light source. Their sizes were calculated using the Peng equation (2.6). The ionic strength of the QDs were then raised to 10, 50, or 100 mM using sodium citrate dibasic from Sigma-Aldrich. Three 2 mL samples of QD solution were loaded and sealed into glass ampoules obtained from University of Utah, department of chemistry glass shop. This process was repeated for each temperature measurement: 100, 130, and 150 °C. A muffle furnace was then heated to the target temperature before three ampoules of each citrate/QD mixture were placed inside it. At 30, 45, and 60 min, one ampoule of each was removed and cooled using gentle convection. The absorbance spectra were then measured again using the Ocean Optics spectrometer, leading to the estimation of the mean diameter from the characteristic

peak using the Peng equation (2.6).[10]

Dynamic light scattering

The samples of QDs were synthesized following the previously outlined aqueous synthetic method. Individual 25 mL samples then had sodium citrate amounts ranging from 3 to 100 mg added to them. Samples were loaded into a flow cell where the ζ-potential and ionic strength were measured using a Möbiuζ from Wyatt Technology. Hydrated QD radius and size distribution were measured using DynaPro NanoStar from Wyatt Technology. QD samples were then heated in an autoclave from Autoclave Engineers for 4 h at 150 °C. The ζ-potential, ionic strength, and size distributions were then measured again.

Results

Dynamic light scattering

The growth rates of QDs in water were observed changing with different concentrations of citrate. Dynamic light scattering (DLS) allows for more in-depth investigation of these changes by measuring both size and surface potential. Combining these measurements with hydrothermal treatment explores the relationship between surface potential and stability. The addition of sodium citrate to QD samples resulted in variation of the surface potential, shown in Figure 3-1. Subsequent measurements were used to study the effect that ζ-potential had on the characteristics and stability of the QDs. The QDs were heated as described and their size and optical properties were measured again. Changes in the QD size were determined by observing their absorbance properties and with DLS. In Figure 3-2 the characteristic absorbance wavelength shift from the original samples is shown compared to the ζ-potential of each sample.

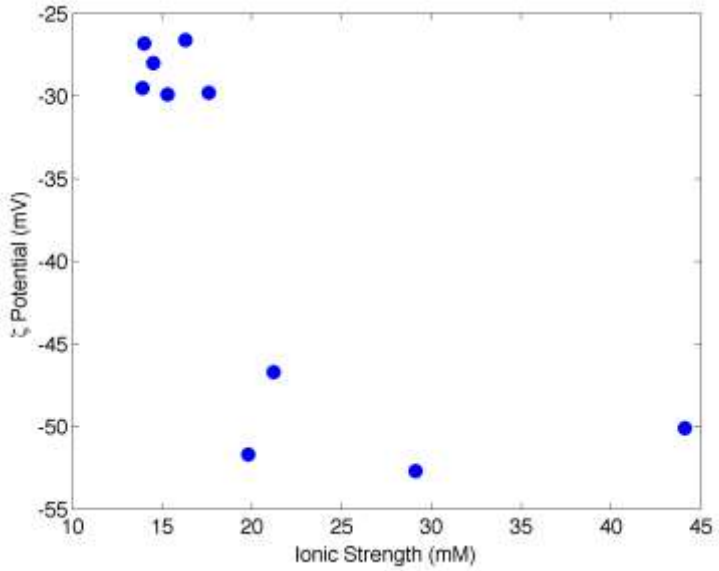

Figure 3-1 - The change in ζ-potential for samples of QDs due to the addition of citrate. The citrate amount added is indicated by the ionic strength of the solution.

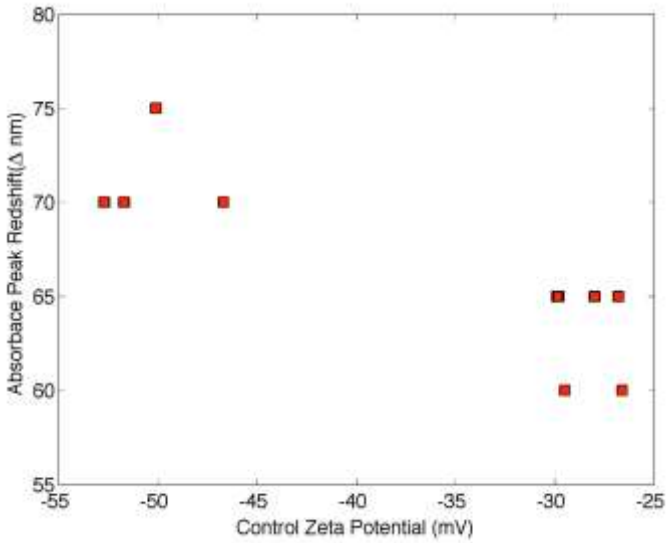

Figure 3-2 - The redshift of the QD characteristic absorbance peaks after 4 h at 150 °C compared to each samples' ζ-potential. Shift is based on a control QD samples λ_{max} of 510 nm.

Aqueous solubility

Establishing the fundamental parameters of this model experimental system allows for further study on the QD behavior in high-temperature solutions. The improved understanding of how monomers are behaving at the interface can be used to predict how QDs will behave in aqueous solutions in high-temperature porous media. An example of an unheated QD sample spectrum and one that was heated for 60 min at 150 °C is shown in Figure 3-3. QD sizes before and after the experiment were calculated from the location of the characteristic excitonic absorption peak using the Peng equation (2.6). The sizes were then plotted against the amount of time spent at the high temperatures. Figure 3-4 shows the comparative plots of diameter versus time for different temperatures and ionic strengths. The results of the linear regression were subsequently used to determine the energy barriers for the growth process using the Arrhenius relationship. In particular, the rate constants are the slopes of the Arrhenius model linear regression shown in Figure 3-5. The subsequent activation energy barriers are tabulated in Table 3-1

Discussion

Dynamic light scattering

The behavior of these QDs in high temperature, aqueous environments revealed a dynamic system where crystals change size in the presence of excess monomer and elevated temperatures. These changes were influenced by different ionic strengths, as shown by the addition of varying amounts of sodium citrate. The set of DLS results from before and after hydrothermally treating the QDs are relevant for understanding how QDs will respond to high temperature environments. Traditional colloid transport experiments have identified surface potential as a critical parameter for recovery or retention. Different amounts of

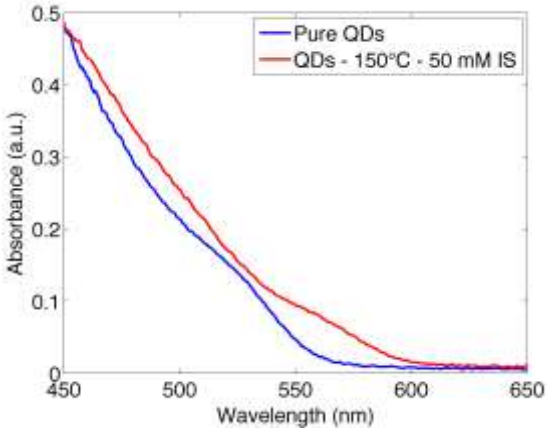

Figure 3-3 - Absorbance spectrum of pure QDs and QDs heated for 60 min at 150 °C indicating mean nanocrystal growth.

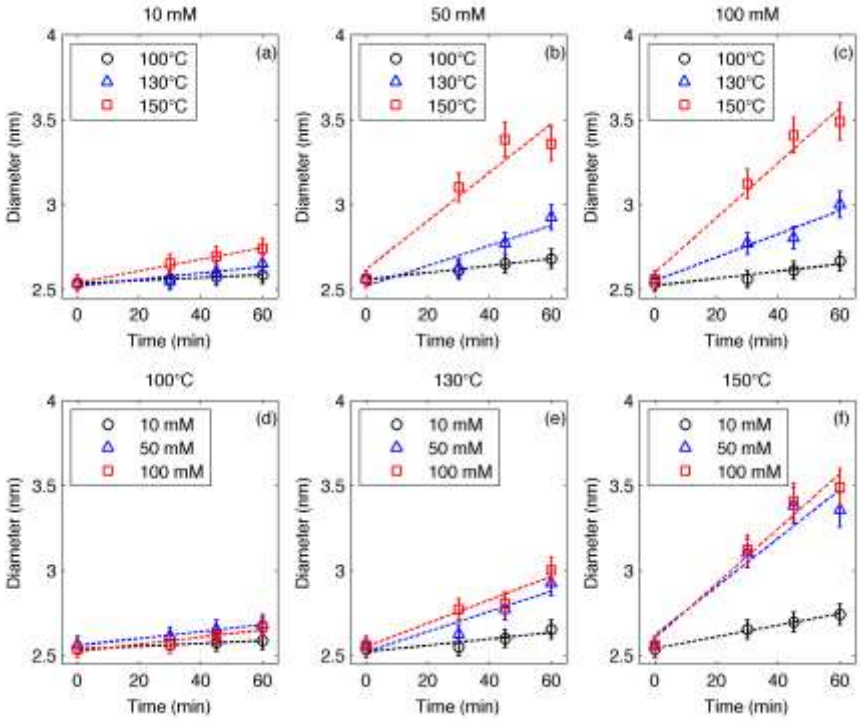

Figure 3-4 - The size evolution of the six experiment parameters; (a)-(c): ionic strength = 10, 50, and 100 mM; (d)-(f): T = 100, 130, and 150 °C. The discrete points are the experimental diameter measurements and the dashed lines show a linear regression for each set of data.

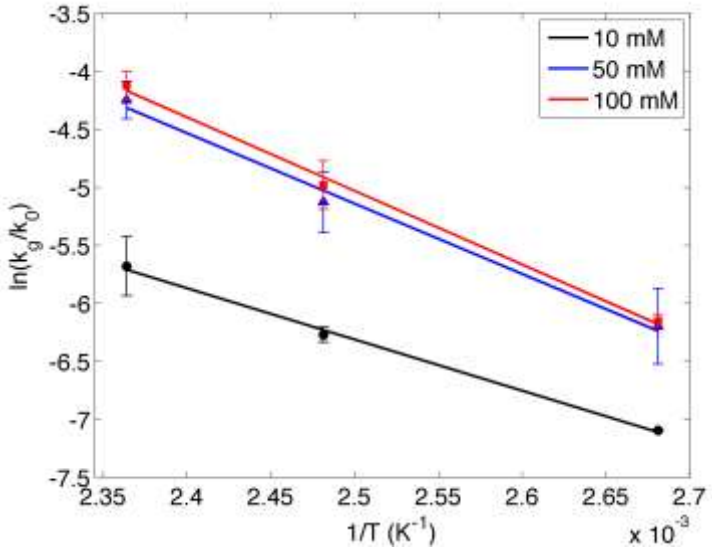

Figure 3-5 - Linearized Arrhenius plots for each set of ionic strength experiments. It is evident that for all three ionic strength experiments that the behavior of the crystal growth follows an Arrhenius model that describes their energy barriers.

Table 3-1: Activation energy results for QD growth from Arrhenius model

Ionic Strength (mM)	Activation Energy (kJ mol^{-1})	Uncertainty (kJ $mol^{-1)}$
10	37	± 2
50	50	± 5
100	53	± 3

sodium citrate were added to each QD sample. Conductivity was then measured and correlated to the ionic strength. The ligand citrate has three terminal carboxyl groups that provide two functions:

1) High amounts of negative charge at the fluid-ligand interface in this pH range of 7 to10, and,
2) Branched carbon chains that provide steric hindrance to QD-QD interaction.

The result of the increasing the amount of citrate molecules in solution is seen in Figure 3-1, where the QDs ζ-potential is near -27 mV between 5 and 15 mM ionic strength but then rapidly decreases to between -45 and -55 mV. This shows that the amount of negative charge on the QD surface is increased, consistent with increased surface coverage by citrate molecules. Colloids with ζ-potential values around -40 mV are generally considered to be very stable due to electrostatic repulsion effects.[11–13] Figure 3-1 shows that larger additions of sodium citrate did not continue to lower the ζ-potential, but a transition at ionic strength of 20 mM from -20 mV to -45 mV was observed. The larger magnitude ζ-potential at the increased ionic strengths exhibited larger resistance to wavelength shifts when exposed to high temperatures. This is in agreement with existing results on colloidal systems, which predicts stable (nonagglomerative) colloids at -40 mV.[13]

Using the ζ-potential as a metric for colloid transport in porous media is a common approach. It is a simple and rapid measurement that provides a first approximation of the stability of a colloidal mixture. The QDs that were heated had their characteristic absorption wavelength measured and compared to the control samples properties. In Figure 3-1 there are the two distinct groups with similar ζ-potentials over the range of measured ionic strengths. These groups subsequently have similar thermal stability characteristics, shown in Figure 3-2. The QDs that had ζ-potential between -25 and -30 mV had their characteristic wavelength redshift by 60-65 nm. From the Peng equation (2.6) this corresponds to a

diameter increase from 2.5 to 3.4 nm. The absorbance maximum of QDs with larger magnitude ζ-potential redshifted up to 75 nm, corresponding to a final diameter of 4.0 nm calculated from the Peng equation (2.6). The distance the characteristic peak shifts highlights the unique nature of QD optical properties. The primary wavelength absorbed goes from green to yellow and orange, a distinct difference in the spectrum, and further emphasizes how small size changes can have dramatic effects.

Aqueous solubility in simulated geothermal conditions

The QDs at each ionic strength and temperature exhibit linear growth over the time period of 0 to 60 min explored in this set of experiments. At 10 mM ionic strength the diameters of the QD samples at each temperature undergo minimal change, with a maximum diameter shift of 0.2 nm occurring at 150 °C. This is similar to the behavior of all three ionic strength experiments at 100 °C and shows that under low ionic strength and low temperature conditions, the QDs exhibit the smallest amount of size change. At 50 and 100 mM ionic strength the QDs under 100 °C show similar growth characteristics. With an increase in temperature, the QD size increases more, Figure 3-4a-c, than with an increase in ionic strength, Figure 3-4d-f. The strong temperature dependence indicates that the growth process from 0 to 60 min is kinetic-based, though it is influenced by the ionic strength.

The linear growth exhibited by the QDs is consistent with a rate law that is independent of the particle size, concentration, or monomer concentration. Without purification of the QDs after synthesis, the monomer concentration changes are insignificant to the observed growth of the particle. The results of the Arrhenius analysis in Figure 3-5 support this hypothesis. Between 100 and 150 °C, each ionic strength system behaves in agreement with an Arrhenius model, as shown by the strong linearity of the kinetic rate data. The activation energy increases from 39 ± 2 kJ mol^{-1} at 10 mM to 53 ±3 kJ mol^{-1} at 100 mM.

The increase in the radius is due to the "salting out" effect of decreasing solubility with an increase in ionic strength. The solubility of crystal structures generally decrease with increased ionic strength and is more noticeable at high ionic strength where solution behavior does not follow ideality. Similar particle solubility trends with ionic strength have been documented in studies of gas-phase aerosol formation.[14,15] Common salting out effects do not take into account that the system solution phase consists of both sodium citrate salt and precursor monomers. These are factors that may contribute to the overall increase in the activation energy, while the monomers in solution provide additional material that allows crystal growth.

Conclusions

The dependence of growth kinetics of aqueous QDs with temperature and ionic strength was tested. This facilitated planning QD transport experiments under similar conditions. The QD samples showed linear behavior under each condition. The diameters of QDs at 100 °C temperatures changed less than 0.2 nm under all ionic strength conditions, while at 150 °C diameter growth up to 1 nm was seen. Increasing temperature was shown to be the driving force for QD growth, aided by the salting out effect due to higher ionic strength. An analysis of the kinetic behavior for each set of ionic strength experiments demonstrated that growth followed an Arrhenius kinetic model. Activation energies for particle growth were 37 ± 2, 50 ± 5, and 53 ± 3 kJ mol^{-1}.

Both hydrophobic and hydrophilic QD samples exhibited transient solubility behaviors at high temperature. The organic soluble QDs show that fundamental surface thermodynamics can be determined from modeling the dissolution. The aqueous QDs show linear growth under geothermal conditions with the presence of solution-phase monomers. These coupled solubility experiments provide the basis for the next set of experiments where

QDs are injected into a porous medium. Across the range of temperatures at each ionic strength, the QDs exhibited linearized Arrhenius behavior. This allowed the activation energy of growth to be determined. The solution-phase behavior of QDs during transport is an important parameter for geothermal tracers. These experiments have shown that the mean size of these QDs is not stable under geothermal conditions. However, the kinetic basis for predicting QD diameters following injection into high-temperature porous media has been established. Now that the behavior of the QDs in the fluid-phase is established, the role that interaction between QDs and sand surfaces plays in QD transport needs to be investigated.

References

(1) May, R.; Akbariyeh, S.; Li, Y. *Environ. Sci. Technol.* **2012**, *46* (18), 9980–9986.

(2) Bradford, S. A.; Torkzaban, S.; Simunek, *J. Water Resour. Res.* **2011**, *47* (10), W10503.

(3) Kini, G. C.; Yu, J.; Wang, L.; Kan, A. T.; Biswal, S. L.; Tour, J. M.; Tomson, M. B.; Wong, M. S. *Colloids Surf. Physicochem. Eng. Asp.* **2014**, *443*, 492–500.

(4) Shen, C.; Li, B.; Huang, Y.; Jin, Y. *Environ. Sci. Technol.* **2007**, *41* (20), 6976–6982.

(5) Torkzaban, S.; Bradford, S. A.; Wan, J.; Tokunaga, T.; Masoudih, A. *Environ. Sci. Technol.* **2013**, *47* (20), 11528–11536.

(6) Johnson, W. P.; Tong, M.; Li, X. *Water Resour. Res.* **2007**, *43* (12), W12S13.

(7) Elimelech, M. J. *Colloid Interface Sci.* **1994**, *164* (1), 190–199.

(8) Chen, K. L.; Elimelech, M. *Environ. Sci. Technol.* **2009**, *43* (19), 7270–7276.

(9) Rogach, A. L.; Nagesha, D.; Ostrander, J. W.; Giersig, M.; Kotov, N. A. *Chem. Mater.* **2000**, *12* (9), 2676–2685.

(10) Yu, W. W.; Qu, L.; Guo, W.; Peng, X. *Chem. Mater.* **2003**, *15* (14), 2854–2860.

(11) Lin, S.; Wiesner, M. R. *Langmuir* **2012**, *28* (30), 11032–11041.

(12) Siubhan A. Macpherson, G. B. W. *Adv. Powder Technol.* **2012**, *23*, 478–484.

(13) Hogg, R.; Healy, T. W.; Fuerstenau, D. W. *Trans. Faraday Soc*. **1966**, *62* (0), 1638–1651.

(14) Kroll, J. H.; Ng, N. L.; Murphy, S. M.; Varutbangkul, V.; Flagan, R. C.; Seinfeld, J. H. J. *Geophys. Res. Atmospheres* **2005**, *110* (D23), D23207.

(15) Kampf, C. J.; Waxman, E. M.; Slowik, J. G.; Dommen, J.; Pfaffenberger, L.; Praplan, A. P.; Prévôt, A. S. H.; Baltensperger, U.; Hoffmann, T.; Volkamer, R. *Environ. Sci. Technol*. **2013**, *47* (9), 4236–4244.

CHAPTER 4

QUANTUM DOT TRANSPORT IN A POROUS MEDIUM

Introduction and Motivation

The QDs in the previous section had surface potential measured using dynamic light scattering (DLS). This measurement technique uses an electric field to move QDs through an aqueous medium at velocities proportional to their surface potential. The surface potential of particles is dependent on their surface charge density. This charge density occurs due to the attachment of citrate ligands that have terminal carboxyl groups with negative charge. Similarly, the sand surfaces have silica groups that deprotonate and leave negatively charged silanol groups. Both of these result in negative surface potentials. Away from either QD or sand surfaces, the electric potential due to the surface charge leads to regions of counterions (solution-phase ions of charge opposite the surface), followed by a region of coions (solution-phase ions of charge similar the surface). These layers of ions are shown in Figure 4-1.

The potential is determined by the amount of work to bring one test charge in from a reference location to a location some distance away from the surface. The influence of the surface potential drops off into the solution and eventually reaches a reference potential in the bulk fluid. The chemical potential of species *i* can be written as:

$$\mu_i = ze\psi + kT \ln \rho_i \tag{4.1}$$

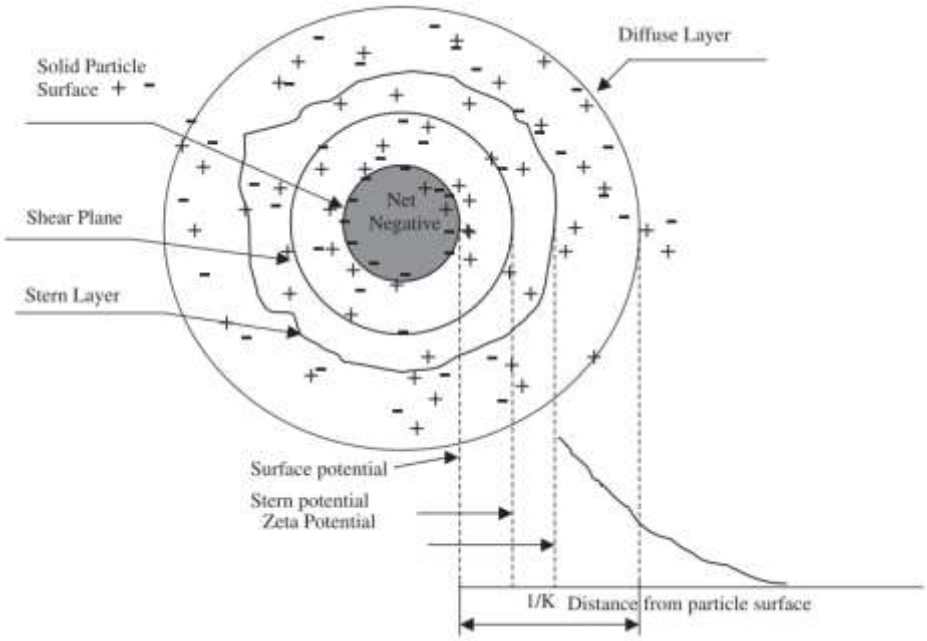

Figure 4-1 - Illustration of solution-phase ion behavior near charged surface (Source: Kaya et.al *Canadian Geotechnical Journal*, 2005, 42 (5). 1280-1289. © Canadian Science Publishing or its licensors. Reproduced with permission).[48]

And subsequently, at equilibrium the concentration of ions in an electrolyte solution follows a Boltzmann distribution away from the surface:

$$\rho_{x_i} = \rho_{\infty i} \exp\left(-\frac{ze\psi_x}{kT}\right) \tag{4.2}$$

This provides an ion concentration estimate for distances away from the surface based on measured values surface potential ψ_0 and bulk ion concentration ρ_∞. The Poisson-Boltzmann equation from electrostatics can be written:

$$\frac{d^2\psi}{dx^2} = -\frac{\rho_0}{\epsilon_0\epsilon} = \frac{\rho_\infty}{\epsilon_0\epsilon} \exp\left(-\frac{ze\psi_0}{kT}\right) \tag{4.3}$$

Combinations of equations (4.1) and (4.2) provide the bases for determining the osmotic pressures as two charged surfaces are brought toward each other.[1]

The repulsive force is due to the ionic double layer away from the charged surface. The high ionic density is predicted by equation (4.2). Bringing particles towards a surface where the ion density is increasing requires work to overcome osmotic pressure. The combination of the charge-induced repulsive potential and the attraction due to van der Waal potential creates a potential field between the charged surfaces of the collector and the colloid. This combination provides the overall interaction energy between the QDs and the sand grain surfaces. The resulting potential energy field is commonly used to predict the likelihood of retention of colloids in porous media. Regions of attractive force, either near the surface or in local energy minimums, result in colloid retention. Large energy barriers result in electrostatic repulsion and subsequently do not favorably retain colloids.

Numerous formulations of the interaction energy have been derived using two

infinite plates of constant surface potential. These derivations have been extended to describe the behavior between two charged spheres. Determination of these potentials, even for simple geometries, has relied on a series of assumptions. The most commonly applied approximation is the Derjaugin assumption (DA) that prescribes that the screening length κ^{-1} is much smaller than the radius of curvature of the particle, $\kappa r_p >> 1$. This has been shown to be a good approximation for a number of colloidal systems and has been used extensively to incorporate surface charge and electrostatics into clean-bed colloidal filtration and transport theory. It is critical to note that this assumption is not typically applied to small particles such as QDs. Lin and Wiesner addressed the DA and its use in nanoparticle stability.[2] They compared existing rigorous non-DA formulations of the interaction potential from Bhattacharjee et al. against DA formulations to predict deposition of nanoparticles on a porous medium. They concluded that the DA formulations can be used, though there are other physical issues that arise from particles with high curvature.[3]

The formulation proposed by Lin and Wiesner, equation (4.3), was adapted from commonly used formulations from Gregory and Bhattacharjee et al. for colloid-surface interaction potential:[2–4]

$$\Delta V_{El} = \frac{64\pi\epsilon}{\kappa}\left(\frac{kT}{ze}\right)^2 \gamma_1\gamma_2\left[\left(\kappa r_p - 1\right)\exp(-\kappa h) + \left(\kappa r_p + 1\right)\exp\left(-\kappa\left(h + 2r_p\right)\right)\right] \tag{4.4}$$

$$\Delta V_{VDW} = \frac{-A_{132} r_p}{6h} * \left(\frac{1}{1 + \frac{14h}{\lambda}}\right) \tag{4.5}$$

$$\gamma_i = \tanh\left(\frac{z_i e\psi_i}{4kT}\right) \tag{4.6}$$

Where κ is the Debye screening length:

$$\kappa = \left[\frac{e^2\left(\sum n_i z_i^2\right)}{\epsilon\epsilon_0 k_B T}\right]^{1/2} \tag{4.7}$$

The interaction energy between QDs was also calculated in order to compare it to the interaction between a colloid and a collector. The Lin and Wiesner formulation for potential energy between two spheres is:[2]

$$\Delta V_{EL} = \frac{64\pi\epsilon\epsilon_0}{\kappa}\left(\frac{r_{p1}r_{p2}}{r_{p1}+r_{p2}}\right)\left(\frac{kT}{ze}\right)^2 \gamma_1\gamma_2 \exp(-\kappa h) \tag{4.8}$$

Before applying these results to the calculation of interaction potentials, it is important to note where the experiment variables will be a significant influence. Higher ionic strength decreases the Debye screening length, as the increased concentration of ions in solution around the charged surfaces leads to dilution of the surface charge's influence into the solution (i.e. the distance within which a colloid can "detect" a sand grain). When the ionic strength of the solution is increased, the thickness of the diffuse layer decreases even more rapidly, effectively shielding the surface charge of the colloid or collector. The attractive potential between surfaces is a superposition of van der Waal's pair potentials, if each atom of the QD was brought towards the surface individually. The dependence of the interaction potential on temperature can also be predicted. First, the temperature is incorporated into the Debye length calculation and counteracts the effect of salinity – a lower ionic strength

extends surface charge while lower temperature shields it. For this reason, higher temperatures will likely result in decreased retention events due to the increase in the electrostatic repulsion dependence on κ. However, the pre-exponentials γ_i exhibit inverse dependence on temperature and subsequently act to dampen the repulsion increase with temperature. Consequently there may be regions between surfaces where the electric potential is either attractive or repulsive.

There are a number of assumptions and potential drawbacks that need to be considered when using the Lin and Wiesner formulation of the interaction energy, equation (4.8). As indicated previously, the primary simplification that was introduced was that the Derjaugin assumption (DA) is valid. There have been numerous studies on colloids ranging from 30-500 nm in diameter. The 30 nm particle studies result in κr_p values that are the minimum acceptable for applying the DA. Given that QDs are very small particles, comparing DA formulations to non-DA formulations leads to inconsistencies at low ionic strengths since both decreasing ionic strength and increasing r_p lead to failure of a $\kappa r_p >> 1$ stipulation, resulting in κr_p values on the order of one or lower. The interaction potentials calculated from the non-DA formulation by Lin and Wiesner deviate significantly around 10 mM and there are distinct differences until the ionic strength is on the order of 10^3 mM, where κr_p exceeds 10. At small sizes ($r_p < \sim 25$ nm) the Lin and Wiesner non-DA formulation interaction potential is very sensitive to the particle radius used in the calculation. So even though Lin and Wiesner argue the DA form is valid for nanoparticle stability, their model system does not directly apply to the very small QDs here. A range of particle sizes were used to test the formulation of equation (4.4) to emphasize the sensitivity of the near-surface interaction energies between a particle and a surface when the particle size is small. This is shown in Figure 4-2. Figure 4-2 demonstrates that as a particle size decreases, this formulation predicts that the potential at small separation will be dominated by the van der Waal

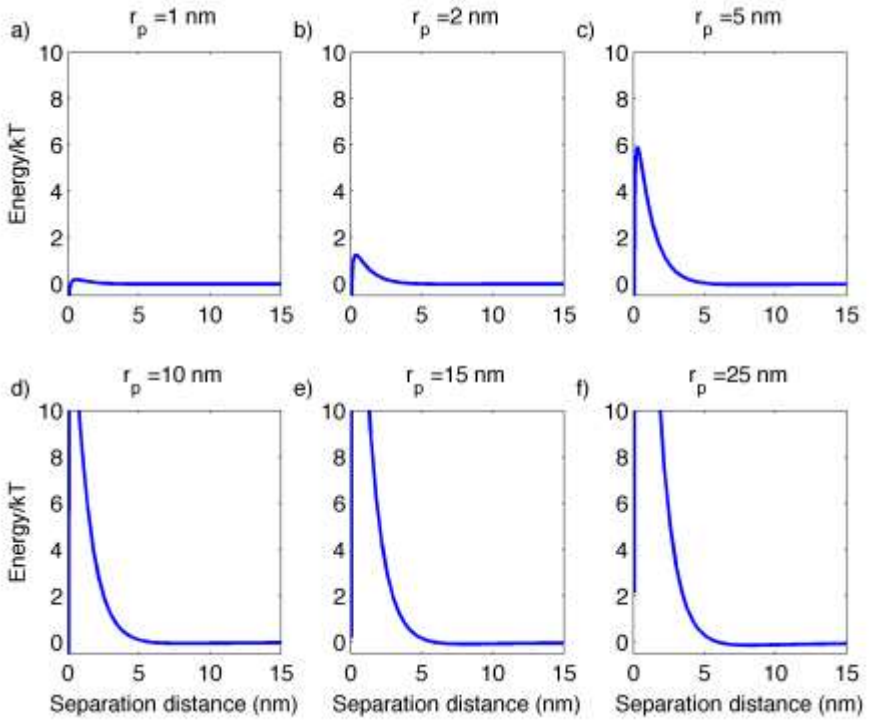

Figure 4-2 - Comparison of DA/non-DA formulation with various particle radii at 100 mM ionic strength, using Lin and Weisner non-DA formulation.

attraction term in equation (4.5). The small primary energy barrier suggests that small particles would both readily aggregate, and deposit on charged surfaces. This is contrary to experimental results of particle stability.[2] This failure to accurately predict interaction behavior indicates that existing potential energy formulations may not be effective models for very small particles.

The QD size was calculated using the Peng equation (2.6) and the mean QD diameter was calculated to be 2.5 ±0.2 nm. At this size and with ionic strength of 100 mM, the primary attractive barrier potential is on the order of 1 kT, or the approximate thermal energy of a molecule. This attractive barrier would be overcome easily, leading to permanent QD retention. However, the DLS experiments outlined earlier showed that the mean

hydrodynamic radius of the QDs is between 10 and 20 nm. Referring to Figure 4-2 this radii measurement range (2.5-4.0 nm diameter) suggests that there can be large deviations of the near-surface potential. The lack of a comprehensively used interaction potential formulation for nanoparticles means that the sensitivity of potential at small QD sizes coupled with the absence of agreeing size measurements will have to be considered.

Breakthrough profile: sweep volume and early breakthrough

Overall, there has been extensive work to determine how different environmental factors govern the subsurface interactions of nanoparticles and which of these are the most important in controlling their retention and release. Early studies were motivated by observed disparities in column transport between molecules and colloids and were analyzed in the context of molecular transport. Generally, transport of ionic and molecular species through a porous medium follows the basic advective-dispersive-reactive transport equation:

$$\theta \frac{dC}{dt} = \theta D \frac{d^2C}{dx^2} - v \frac{dC}{dx} - \theta k_1 C \tag{4.9}$$

This form of the species transport equation accounts for the material balance due to diffusion, advection, and a removal process (decay, sorption, etc.). Measuring the concentration of analyte in the effluent of the column provides fundamental information about transport behavior as a breakthrough curve (BTC). This includes both the organization of the porous medium, fluid velocity and residence times, and possible surface interaction. In a perfectly packed medium, each individual grain will be prevented from moving by frictional interaction with the particles around it. The entire bed is constrained by mesh over the inlet and outlet. If the bed is poorly packed, then these grains may move with hydraulic or other

perturbations. This could result in channeling in the column and manifest itself in a BTC as a peak shoulder with early breakthrough.

The failure of molecular transport analysis to sufficiently explain colloid retention, coupled with improved sand and colloid characterization techniques (dynamic light scattering, electron microscopy, etc.), has created the framework for a standalone subfield of porous media transport. Fundamental studies have subsequently expanded into "real-world" applications, shifting from simple model systems to field samples and heterogeneous chemical solutions that mirror subsurface environments. These relatively recent developments are spearheading the expansion of the field to include more extreme parameters: high temperature porous media and nanoscale colloids (QDs).The nature of colloids as a discrete particle distribution also results in divergence of transport behavior from uniform molecules. While small, the QDs can be excluded from pore structures that are swept by the ionic tracers used to define the porous properties of the column. It is therefore important to apply the results of previous work that has been done in colloid transport to better predict which retention mechanisms are relevant.

Effect of temperature on diffusion

Elevated bed temperature is the primary variable of study for application to geothermal systems, and can influence various colloid transport mechanisms. For instance, the dispersion that a molecule or small particle undergoes as it is transported through a porous bed depends on the tortuosity of its flow path (mechanical dispersion) as well as the particle's diffusion constant *D.* The sand grains' sizes don't change through the temperatures of interest (up to 150 °C), so the flow fields will not change due to grain size expansion. Consequently, there is no effect on the mechanical dispersion with temperature. However, the Stokes-Einstein relation is commonly used to estimate *D* for small, spherical particles and

is linearly dependent on the temperature, so an increase in temperature would result in increased diffusion of QDs through the porous bed. This is further accentuated by the decrease of viscosity of compressed water in high temperatures.[5] At high temperatures BTCs would show earlier detection and more gradual development of the maximum plateau. This is commonly represented by "spreading" of the concentration around the ideal Heaviside breakthrough, as seen in Figure 4-3. Since dispersion is a combination of mechanical and Brownian diffusion, different-sized materials will be more or less influenced by the two mechanisms. Larger particles such as bacteria or microspheres have much smaller diffusivities (10^{-10} – 10^{-12} $m^2 s^{-1}$) compared to molecules (~10^{-9} $m^2 s^{-1}$), and are less influenced by their individual random motions (Brownian diffusion) compared to the mechanical dispersion. QDs, with sizes between molecules and particles and room temperature diffusion constants on the order of 10^{-10} $m^2 s^{-1}$ may be sensitive to either mechanism. In order to discern a dominant diffusion mechanism, it will be necessary to look at the QD BTC against a conservative tracer. More particle-like behavior should result in BTCs that are closer to

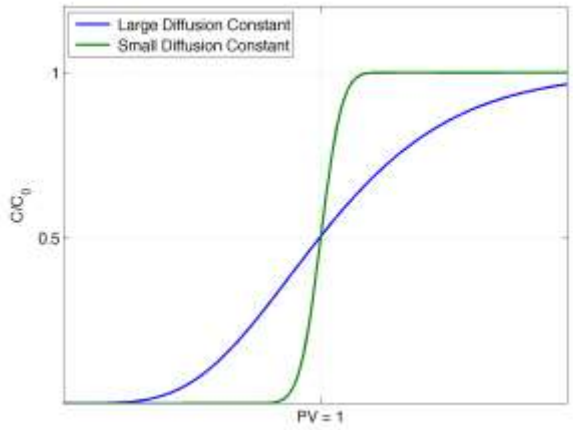

Figure 4-3 - Theoretical breakthrough curves with and without dispersive transport. Dispersion leads to spreading of the concentration front due to non-advective forward and backward species movement.

conservative transport, with minimal dependence on experimental temperature. The breakthrough curves for a baseline salt are used to determine pore volume and water residence time and provide the conservative reference to the behavior of the QDs.

Effect of temperature on BTC profile

There have been very few studies concerning the effects of temperature on the breakthrough profiles of colloids in porous media. While there have been a number of studies on molecular transport in these conditions, for the development of geothermal tracers, the differences of molecules from medium and large-sized particles would suggest that there should be different retention mechanisms.[6,7] The absence of high temperature studies leaves opportunities to better understand particle transport. Existing work has identified a number of mechanisms that influence particle transport to varying degrees. In these legacy studies, transport dependencies on temperature have not been studied explicitly. Arguably, the most studied are the interaction energies between the charged surfaces of the transporting particle and the porous medium grain. Although there are many formulations for the energy calculations due to the nature and complexity of surface interactions, each invokes a dependence on the Debye length κ^{-1}, equation (4.7). This distance is a metric of how far the electric influence of a surface with ζ-potential will extend into an ionic solution.

The shielding length away from a charged surface increases with an increase in temperature. This shielding is due to the Boltzmann distribution of ions near the charged surface. This results in charged surfaces being able to "sense" each other more at higher temperatures, subsequently leading to increased interaction (attractive or repulsive). The calculation of the interaction profile under experimentally relevant conditions yields regions of both attractive and repulsive forces. With a decrease in the shielding of the charged surfaces with increased temperature, the amount of interaction between QDs and a porous

medium is also expected to increase. This will result in retention features evidenced in the BTC, including steady-state plateaus lower than unity, retarded breakthrough, or elevated retention within the column.

Effect of ionic strength on BTC profile

Unlike the temperature, ionic strength has been extensively studied as a factor in particle transport, due to its importance in the retention and release of colloids in the environment.[8–12] The magnitude and composition of ionic strength in the subsurface differs geographically, creating a diverse set of conditions for study. These are unique to the reservoir of interest and have facilitated a wide range of experiments in order to build transport response surfaces for conditions such as: single and multivalent ions, single and multi-component solutions, or highly saline environments. The effects of the many variables that comprise an ionic strength go beyond electrostatic interaction and include chemical reaction or phase change. Consequently, ionic strength evaluations have become a large subfield of study within particle transport and wastewater treatment. Limiting the scope of a study to interaction potential (without explicit studies on concentration, particle or collector size, etc.) narrows the focus of the effect of increasing/decreasing the ionic strength to only a few factors. Again one of these factors is the dependence of the Debye length on ionic strength and the calculation of the characteristic screening length. Surface charge is increasingly screened with the addition of ions to the system, decreasing the range at which two particles can electrically sense each other. This counteracts the effect of an increase in temperature and, without additional assumptions, would act to reduce both particle-particle aggregation and particle-collector deposition. In fact, the stabilization of inorganic and biological particles has been studied extensively, and stabilization has been shown to be successful under modest salt concentrations.[2,13–15] However, instability arises with high ion concentrations due to the

breakdown of electrostatic repulsion from two charged surfaces, resulting in high levels of aggregation and deposition. In summary, the effects that might arise from systematic increases of the salt include a range of relative stability, presented as limited retention, minimal size change, or both. This, as predicted by earlier studies on ionic strength, will be followed by increases in retention as the attractive forces begin to dominate both the interparticle relationships and the particle-collector interaction.

Summary of mechanisms and expected results for adsorbed cadmium

Some retention mechanisms were outlined above in terms of their expected influence on a BTC profile. Determining the degree of surface deposition is important for determining the fate of the QDs that were not detected in the effluent from a packed column experiment. For example, after a test has been completed, measuring the profile of the detected cadmium along the column may yield information about the amount of QDs spatial deposition. Measuring the cadmium profile with depth (location along the sand column) is the primary consideration because many of the mechanisms retaining or holding up the QDs rely on the rate of QD transfer from the bulk to the surface (or into the secondary energy minima). This subsequently dictates the amount of QDs that are deposited. The flux of QDs towards the surface is a dependent of the concentration gradient, which is steepest at the column inlet. The decrease in QDs along the length of the column from inlet to outlet is due to particle concentrations in subsequent series of bins (unit collector sections of column). Colloids entering a section will have a concentration C_0 and will exit the same section with a concentration C_1. Within the section the difference in concentration is the amount of colloids held by the collectors, C_0-C_1. Since the flux of QDs towards a surface depends on the bulk concentration, downstream bins will have lower numbers of QDs and there will be fewer retention events. The consequence is that the highest concentrations of retained QDs are

located nearest to the injection port, particularly for irreversibly retained QDs. This retention gradient applies to those mechanisms that depend on the flux from the bulk fluid. Without resolution of individual grains or a representative elementary volume, it is difficult to determine what other mechanisms may be operating – such as stagnation point deposition or grain-to-grain contacts. To complicate the situation further, colloids have exhibited reversible adsorption in various conditions. This is due to weak secondary energy minima or locally weak hydrodynamic drag forces, resulting in reactive tracer behavior and extended QD residence times.[16–18]

Time-dependent deposition models (straining and multilayer deposition)

The mechanisms for retention described above have been used for single-layer, one-site deposition of colloids on collectors, and change due to occupation of adsorption sites over time. Another retention mechanism that has been observed is straining of the colloids at grain-to-grain contact points. This phenomenon results in a BTC concentration profile that declines over time. The preinjection sand column contains no colloids at grain-to-grain contacts. As colloids are advected through higher velocity pore throats, the likelihood increases that the colloid-colloid or colloid-surface primary energy barrier will be overcome. This increases the possibility of straining in two ways:

1) The new colloidal aggregate has a larger mean radius, which has been shown to be an important parameter in the colloid removal via straining and,
2) Colloids that have been intercepted and are “stuck” on the surface slightly increase the overall surface area of the collector; and if the energy barrier between two colloids is lower than the between a colloid and a surface an attached colloid provides a region with a more favorable retention characteristic to subsequent colloids.

The basis of these mechanisms predict that as more colloids participate in straining, the

likelihood increases that subsequently injected colloids will also be strained. This means that the recovery of colloids injected later will be lower than those injected initially, and the BTC concentration will decrease over time. QDs are much smaller than many conventional colloids that have been studied in groundwater systems and the guidelines that have been developed to predict the presence of straining are generally inadequate. These guidelines have been established by series of studies that failed to observe straining when the colloid diameter was smaller than approximately 1% of the collector diameter.[19] Our system consists of QD diameters that have diameters approximately 0.001% of the sand grains. This is three orders smaller than the closest colloid sizes that observed straining.[20–25] Therefore, without conducting studies that either observe real-time QD deposition (in-situ visualization of columns) or through postexperimental analysis of the porous medium, it is not justified to assume that straining is causing the profiles exhibited here.

Explanation of dynamic deposition rates is not limited to straining. Multilayer deposition may result from where multiple kinetic processes. If changes in ionic strength dictate the interaction between QDs, then this would include QDs that are retained by collectors as well as those that are in the mobile phase. Furthermore, if the QD-collector kinetics are slow compared to QD-QD aggregation kinetics, then the effective collection kinetics will increase over time as QDs become immobilized on the surface (slowly) before mobile QDs become stuck (quickly) onto them.[26] This is analogous to two separate removal mechanisms with unique kinetic rate constants.A decrease in concentration with time has been termed “ripening” of the column and has been proposed as a retention mechanism in biological colloid transport. Favorable QD-QD interaction could also occur in the mobile phase, resulting in QD aggregates. The larger sizes of aggregates have important implications in both straining (larger particles more susceptible to straining mechanisms) and estimations of the electric potential interaction (particle size is a parameter within the interaction energy

calculation). Existing estimates predict that straining becomes relevant when the collector diameter is at least 20-200 times the diameter of the colloid. Current research is not in agreement with where the maximum limit of this ratio is, but there is indication that additional variables influence straining retention.[17,19,23,27] This would require approximately 50 million, 25 nm diameter QDs aggregating (to form a sphere of diameter 9 μm – a conservative estimate). Observing any size changes of eluted QDs, as seen by changes in the characteristic absorption feature, is critical to determining whether either of these processes are relevant.

Additional influences and mechanisms

A number of additional influences have been proposed. These are increasingly of interest as colloid transport analysis becomes more sophisticated. One of these is the effect that divalent molecules in solution have on the retention of colloids in transport. Research efforts on this subject have considered divalent cations, due to the common presence of magnesium and calcium in groundwater (although sulfate and carbonates are also often present). Chen et al. reported that citrate-stabilized nanoparticles aggregated much more readily in the presence of divalent ions than monovalent ions, and nanoparticle deposition rates onto a silica surface increased in the presence of divalent ions compared to monovalent ions.[15,28,29] Overall, while these phenomena are not explicitly addressed in this thesis, the experimental conditions consist of di- and trivalent anions of citrate in solution and bound to the QD surface. The designed influence of these is to reduce interaction between QDs through charge repulsion and steric stabilization of the surfaces. It is possible that the citrate may, under the stressful experimental conditions, facilitate retention or size changes of the QDs through bridging, resulting in either QD-QD-collector “chains” or larger QD aggregates that can be filtered at grain-to-grain contacts.

Mechanisms for retention of adsorbed cadmium

There is little mention in the literature of mechanisms for increased colloid deposition downstream, as the large diffusive flux at the inlet drives upstream colloid deposition. Temporary retention in the secondary energy minimum is often identified as the cause of retarded colloid mobilization, although alternative hypotheses have been proposed where retention is affected by multivalent ions in solution. The synthesis and aqueous dissolution of the QDs in Chapter 3 do not include additional purification techniques to minimize post-synthesis changes to the colloids. This results in an ionic solution that includes citrate, which acts as a QD surface-stabilizing ligand. Citrate has been used for making hydrophilic nanoparticles and also to serve as a scaffold for encasing colloids in silica for biological and environmental applications.[14,15]

Many researchers have demonstrated hydrodynamic drag forces influence colloid retention in a column. Higher flow rates coincide with decreased retention.[22,30] The increased well depth is a mechanism for the secondary potential deposition under the increased ionic strength conditions. Reduced fluid velocity near the collector surface results in lower hydrodynamic drag on particles located in the secondary potential well.[31] Shani et al. recognized that mobilization of particles due to hydrodynamic shear may account for increased downstream deposition. A higher primary energy barrier at increased ionic strength coupled with the larger magnitude secondary energy minima suggest that some particles may translate along the surface of the porous media more slowly than those in bulk, leading to a chromatographic-type peak feature seen in the retention.[32] Becker et al. observed increasing deposition concentrations along the column and attributed this to blocking of active sites on the sand coupled with polymer bridging interaction.[33] The combination of increased well depth and lower hydrodynamic force establishes conditions that are more favorable to QD retention. Alternatively, blocking of adsorption sites may result in the

downstream presence of QDs. Modeling the flow fields through pore throats provides more insight into the forces that particles experience at different distances from the surface experience. These distances are significant since the velocity profile decreases as it approaches a surface, and the low fluid velocities near the sand surface can coincide with features in the interaction potential. An example of this would be a low flow velocity overlapping a region of attractive force that results in more favorable retention. Changes in flow rate over the course of a QD injection may contribute to variability in transport behavior. This may affect QD retention due to dynamic particle drag forces and a larger influence of attractive electrostatic forces near the collector surface.

These possible retention mechanisms require specific experimental studies and certain assumptions in order determine whether they significantly influence the transport behavior of QDs. Evaluating the signature of the BTC itself, however, is a powerful method for inferring the strength of the interactions. In field-scale analysis of tracers, long tailing of the BTC often represents the complexity of subsurface transport pathways through fracture networks and regions of varying conductivity. At a benchtop scale, however, the porous medium is assumed to be more homogeneous. Delayed breakthrough or tailing will indicate the presence of reversible interactions between a colloid and a collector. Reversible interactions have been systematically developed for molecules to interact with a porous medium in specific ways, allowing estimation of the surface area by using a partitioning coefficient. Development of a new tracer requires that the in-situ behavior of the analyte in the porous medium of interest is well understood, whether or not it behaves conservatively. If any of the above mechanisms significantly affect the QDs, then reactive transport behavior is envisioned. However, if the reactive behavior is not permanent, such as diffusion out of a weak energy well, this needs to be understood in detail. The strength of an interaction will determine the shape of the BTC: a strong interaction will cause low initial breakthrough,

while a very weak one will lead to conservative transport behavior. For intermediate or reversible interaction between a colloid and a collector, the initial breakthrough will be delayed as adsorption sites are filled by QDs. As the QDs are injected, there is a flux from the high QD concentration in the fluid phase towards the low QD concentration on the solid surface. If an attractive force is present, due to the pair intermolecular force above in equation (4.5), then there is a chance of a retention event. Over the course of the injection, a finite number of these retention events occur. As QD-free water is flushed through the column after the injection period, the flux is then directed towards the bulk fluid and there could be release events from the collector surfaces back to the mobile region. The strength of the retention mechanism will dictate how quickly these release events happen and how likely the QDs will be entrained again, leading to a short (low attraction) or long (high attraction) tailing period. Finally, if the force of attraction is very strong, then there may not be any tailing since the probability of a release event would be near zero.

Modeling background

The treatment of colloids in porous media transport modeling follows a number of methodologies. There are methods that treat the collection of colloids as a concentration of molecules, allowing traditional modeling techniques and software to be implemented. While the results in the literature are hardly unanimous, these approaches have generally been adopted without explicitly addressing colloid-specific interactions. Sometimes these methods have been abandoned in favor of mechanistic analysis and particle tracking.[34–37] The intricacies between these different modeling approaches has created a new subset of colloid transport study and sparked debate over the dominant forces in colloid retention. The continuum approach studies the breakthrough curves of the colloids in the effluent. It is most easily applied to columns with favorable retention conditions that lead to clear retardation

factors and distinct behavior of the column's steady-state plateau This allows for relatively easy experimental model verification where long-term colloid injection is required to establish the plateau These assessments can then be used to determine the sticking efficiency α and subsequently the single-collector efficiency η from the steady-state advection-dispersion equation. The physical meaning of these terms is in dispute, and additional factors have been introduced to incorporate theory from interaction potential energy, gravitational settling, and straining mechanisms to add credence to the measurement of η and its relationship to the physical processes of colloid retention.[38] In contrast, mechanistic approaches study the forces – hydrodynamic, Brownian, electrostatic – acting on individual particles to predict single collector efficiency of a "unit cell." The protocol then involves integrating over the length of the column and applying the calculated α to the overall retention. These methods offer improved control over the relevant physics of the system but are computationally expensive and rely on complicated or uncommon experimental techniques (single-particle tracking and visualization over time). There are advantages for either approach. Both generic numerical approaches in conjunction with experimental work have shown varying degrees of success in predicting breakthrough profiles or surface retention.

Both of these techniques have been used for modeling nanoparticle transport.[14,23,25,39] A lack of consistent accuracy reveals the complexity of interactions between surfaces. Colloid transport models become further complicated in geothermal settings where high temperature results in additional mechanisms affecting the breakthrough profile. This section is not designed to be a comprehensive study of colloid transport modeling. It is only intended to relate features that may be prevalent on experimental BTCs to previous hypotheses. Becker et al. observed QD/polymer BTCs where the QDs exhibited greatly delayed breakthrough. Surface analysis revealed QD sorption increasing with distance along

the column. This result contrasted traditional colloid retention theories that show highest retained concentrations near the inlet, and were hypothesized to be due to the outcompeting for adsorption sites by other constituents in solution. This result reduces the effective number of adsorption sites. By altering their model with the time-dependent blocking function, the retention profiles under certain conditions could be effectively modeled. A combination of experimental BTC data, surface retention, and physical intuition can be used to effectively model colloid transport.

The governing equations within the column can be written to reflect specific interactions. Matlab is one convenient platform for doing this. This is advantageous because it does not rely on existing prefabricated models that require either over-simplification of the system or advanced programming ability for implementation. The parameters specific to the experimental column: velocity, pore volume, and porosity, are experimentally determined from breakthrough data for a nonreactive species. The rate of adsorption and desorption are then determined by inverse optimization of the model to the BTC data. The resultant rate parameters describe phenomenological results of the experiment, without providing insight about specific mechanisms that are causing the adsorption or entrainment of colloids (i.e., the adsorption rate constant would not specify the difference between primary or secondary energy minimum attachment). Further experimentation is necessary to clarify specific interactions, but this modeling approach offers a first approximation of the governing parameters occurring in QD porous media transport.

Methods – Surface Interaction and Transport

Streaming potential

A threaded PVC cylinder (length 3", diameter ½ NPT, McMaster-Carr Supply Company, Elmhurst, IL) with mating end caps was packed with the porous medium used in the column experiments (46 – 42 mesh Ottawa sand). The sand was packed by repeated, gentle "knocking" of the column, and compressing the sand prior to closing the column with caps. Each cap had two drilled holes; one to accommodate a luer-type connector (Qosina corporation, Ronkonkoma, NY) that was epoxied in place, and one to hold a silver electrode (also epoxied in the cap). A silver mesh (size 50 mesh; Alfa Aesar) was connected to the electrode and placed in contact with the sand pack immediately below the cap over the holes. This mesh contained the sand bed in place and acted as a porous electrode for measuring the electric field across the bed. Figure 4-4 is a schematic of the fixture.

The flush solution comprised sodium citrate with a targeted conductivity. pH was adjusted to 8 using NaOH. The bed was saturated with multiple pore volumes (PVs) of the flush solution over a period of 4 to 6 h. This established chemical equilibrium between the sand surfaces and the solution. The flush solution was covered with paraffin film to prevent CO_2 dissolution during the equilibration period. Equilibrium was determined by observing stability of the potential across the bed using a multimeter. Once equilibrium was established, the streaming potential was measured by increasing the head on the inlet side of the column by adjusting the height of the flush solution reservoir. The pressure difference across the column was determined from the head (the difference between the height of the water in the reservoir and the height of the downstream end). The slope of a plot of voltage versus differential pressure is related to the streaming potential through:

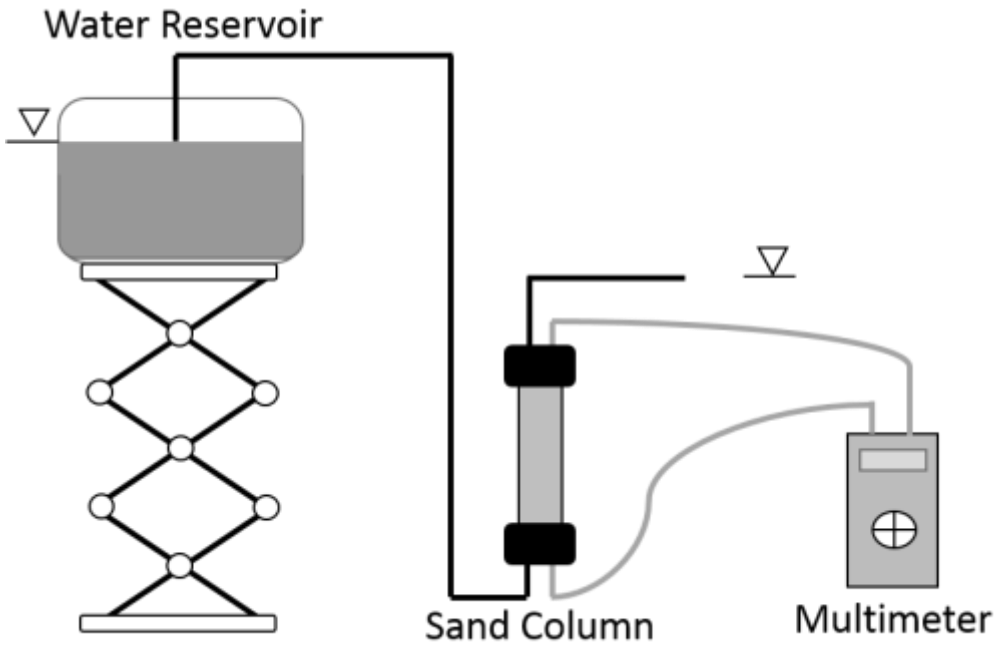

Figure 4-4 - Experimental setup of the sand streaming potential apparatus. The flush solution is introduced to the column directly from a water reservoir and the voltage across the bed is measured with a multimeter. The water reservoir is on an adjustable lab jack to easily change the pressure head gradient.

$$m = \frac{\Delta V}{\Delta P} = \frac{\epsilon \epsilon_0 \zeta}{\eta \sigma_F} \tag{4.10}$$

Surface potential method

The formulation by Gregory et al. is used to determine the overall potential energy profile for nanoparticles in porous media.[2,4] The parameters in Table 4-1 were used for calculating the interaction energy over separation between surfaces. The experimental conditions for the surface potential and transport experiments are outlined in Table 4-1. The Hamaker constant was calculated according to Israelachvili et al., representing the CdS-water-CdS (for QD-QD interaction) or CdS-water-SiO_2 for (for QD-surface).[1,43] Zeta potentials

Table 4-1: Experimental parameters for calculating interaction potential

Particle Radius r_p (nm)	Hamaker Constant A (J)	Valence z	Ionic Strength (mM)	ζ-Potential QDs (mV)	ζ-Potential Sand (mV)
9	3.4E-21	2	[10, 50, 100]	[-28, -50, -70]	-180

of the QDs were measured using DLS as outlined in Chapter 3.

High temperature transport

To study the transport of QDs in high temperature porous medium, a custom flow reactor was constructed. The flow reactor in Figure 4-5 was configured to heat the QD solution before it enters the reservoir ("preheater") and then in the porous media reservoir. This stabilized the target temperature in the porous media bed. The heat flux was delivered using fiberglass insulated heat tape, from Omega Engineering, Inc., and was measured in the preheater and reservoir using thermocouples, also from Omega Engineering. The preheater was set to 75 °C, and the temperature was monitored throughout the experiment. Fluid was pumped upward vertically in all experiments, shown by arrows in the configuration in Figure 4-5. The flow rate was obtained by measuring the time and volume of each fractional volume collected. These volumes were analyzed for salt concentration by measuring their conductivity. The nomenclature for experimental conditions, which will be referred to throughout the dissertation, is outlined in Table 4-2.

The concentration of QDs was evaluated using an external USB2000 spectrometer with LS-450 light source from Ocean Optics. For each transport measurement, clean Ottawa

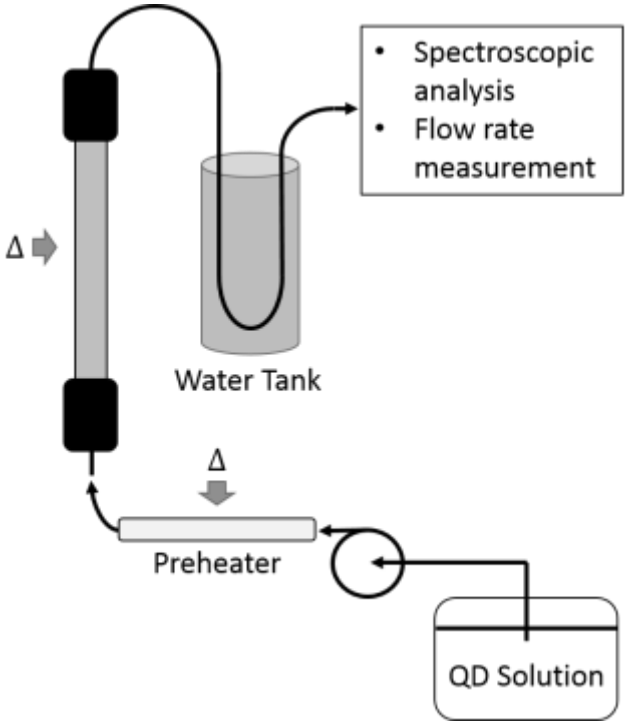

Figure 4-5 - Experimental setup of quantum dot column injection. QDs are injected via peristaltic pump through a preheater before introduction into sand-filled, stainless steel column. The solution is then run through a water tank to cool before being collected for spectroscopy and flow rate measurement.

Table 4-2: Ionic strength and temperature conditions for quantum dot transport experiments

	Temperature		
Ionic Strength	*100 ˚C*	*130 ˚C*	*150 ˚C*
10 mM	100C10	130C10	150C10
50 mM	100C50	130C50	150C50
100 mM	100C100	130C100	150C100

sand was loaded into the column. The sand diameter ranged from 400-425 μm and was cleaned in large batches using the SC1 silica cleaning procedure:

1) A 50 mL solution of 5:1:1 ratio of DI water, ammonium hydroxide (Fisher Chemical), and 30% w/w hydrogen peroxide was mixed and heated in a water bath to 60 °C.
2) This solution was then added to approximately 100 mL of sand and sonicated for 10 min at 60 °C.
3) The wet sand was then gravity filtered and washed with 50 mL of 18 MΩ ultrapure water.
4) The sand was stored indefinitely in DI water before being loaded into the column wet.

Occasional percussive force was used during loading to increase the packing efficiency. Prior to each QD injection the column was equilibrated to the experimental conditions using water containing sodium citrate with ionic strength matching that of the experiment (matching the measured conductivity to that of the QD solution). During these equilibrations, the breakthrough volume of the salt front was measured in order to establish the effective pore volume of the column. This was performed for each column individually since there were small variations in the amount of sand that was loaded in each column. This affords a more accurate pore volume calculation that is independent of other system parameters (versus using making a calculation from assumed packing density and sand unit volume). The porosity of the sand section was estimated from the measured mass added to the column and the volume of the column:

$$\theta = 1 - \frac{\rho_{bulk}}{\rho_{silica}} = 1 - \frac{m_{sand}}{V_{tot} * \rho_{silica}} = \frac{V_{pore}}{V_{tot}} \tag{4.11}$$

The total citrate salt residence time was used in conjunction with the estimated pore volume of the column to determine a value of the total pore volume of the experimental setup, which

dead volume such as the influent and effluent piping, the preheater, and thermocouple wells. The column was equilibrated using the following procedure:

1) Flush with deionized water at room temperature to saturate the system. $V_{inj} > 1.5$ pore volumes
2) Flush with deionized sodium citrate salt solution flush (conductivity matching experimental conditions) at room temperature. $V_{inj} \sim 1.5$ pore volumes
3) Flush with deionized water at 150 °C. $V_{inj} \sim 1.5$ pore volumes
4) Flush with sodium citrate salt solution flush (conductivity matching experimental conditions) at 150 °C. Solution was injected into the column until effluent was optically clear, V_{inj} generally more than two pore volumes
5) Temperature was brought to the target experimental conditions in preparation for QD injection

The repeated salt flushing was done in order to prepare the column as though it were a subsurface reservoir that had not been exposed to QDs (clean bed filtration). It also provided an opportunity to replicate the pore volume measurement and to check if there were strong or weak interactions between the salt solution and the silica surfaces (as would be seen by delays in the breakthrough or changes in the breakthrough profile). It was important that the effluent was optically clear due to the sensitivity of the spectrometer that was used to detect light scattered by small particles. At even moderate turbidity, it can be very difficult to clearly detect QDs in the solution. Even when the effluent was clear to the naked eye small particle scattering was periodically detected by the spectrometer, adding an additional source of error when determining QD intensity. Approximately two pore volumes of QD solution were injected. This facilitated observation of any reversible/irreversible adsorption kinetics occurring during the steady-state injection period.

The aim of the high temperature experiments was to evaluate the response of the QDs

in porous media at different temperatures and a range of ionic strengths. Since there have been reports that colloid concentration can be a principal variable in clean-bed filtration, steps were taken to reduce variation in the QDs themselves as much as possible.[27,44] The QDs were synthesized using previously established methods (Chapter 3) in three 500 mL batches. There were minimal size differences between each batch as verified by absorbance spectroscopy. The three batches were collected in a single vessel, diluted slightly to provide more material for transport, and then divided back into three vessels. This created three batches of uniformly composed QD mixtures. The final concentration of QDs was 10^{15} particles mL^{-1}, determined using an empirical relationship determined by Yu and coworkers.[45] Each vessel contained approximately 600 mL of QD solution, which was enough for the three proposed experiments for each ionic strength. The QD solutions were then modified to the target conductivity using sodium citrate dihydrate (Sigma-Aldrich) before adding NaOH (Fisher) and HCl (Sigma-Aldrich) to establish the pH at 8.0. The ionic strength was related to conductivity through a calibration curve of KCl and solution conductivity (μS/cm) for the instrument (Ultrameter II, Myron L Company).

Sodium citrate was used in order to provide a chemical environment most similar to those used in experimental evaluations described in previous sections of this dissertation, which were designed to minimize size changes in high temperature environments. The system described here, while a reasonable surrogate, does not reflect some of the characteristics of a subsurface reservoir, since it is a simple, somewhat homogenous porous medium, there is minimal mineralogic complexity, and the solution chemistry is different. Studying the behavior of nanoparticle transport under more realistic in-situ reservoir conditions will be an interesting and valuable set of experiments for future researchers.

Analysis of quantum dot spectra

Over the course of a single transport experiment, fractional volumes of effluent were collected, and the following properties were recorded: time, fractional volume, preheater volume, ionic strength, and absorbance spectra. The absorbance spectra were imported into Matlab for analysis. The most basic method of establishing the concentration of QDs in the effluent was to observe the intensity of the QD spectra at the wavelength of the maximum absorbance, λ_{max}, from the "pure" QD sample (the QDs that were injected into the column). There are two caveats:

- First, the intensity at a single point is highly subject to variations in the baseline turbidity of the sample. Should any particulate or mineral be entrained in the mobile phase during the experiment, the response from the spectrometer would alter the detection (and subsequent concentration calculation) of the QDs. Although preventing this intrusion is the primary goal of the long flush injection that procedure did not always prove to be entirely successful.
- Second, this method of analysis assumes that the QD size is stable in the high temperature column.

The validity of these assumptions will be assessed further in the discussion section. This leads to a second proposed method of analysis where the entirety of the spectrum is integrated and compared to the pure QD absorbance. In order to reduce the influence of fourth-power natural colloidal scattering at short wavelengths, the integration is performed numerically using the following scheme to yield the peak area A_k:

$$A_k = \sum_{i=1}^{i=m} I_i\left(\lambda_{i+1}^4 - \lambda_i^4\right) \tag{4.12}$$

The cumulative intensity is then normalized by the integrated spectrum of the pure QDs. The advantage of equation (4.12) over using only characteristic absorbance relates to the reduced dependence of the particular λ_{max}. Specifically the absorbance of a solution is diluted over the entire distribution of QDs, although it is still subject to local perturbations from particulate release events. Furthermore, reducing dependence on the λ_{max} intensity prevents misidentification of the characteristic peak. The characteristic peak can be difficult to locate on samples with weak absorption features, particularly those that have been exposed to high temperatures. The normalization of the spectrum with that of the spectrum of the injected QDs provides the dimensionless concentration, C/C_0, for further analysis.

Column segmentation

Assessing attachment of QDs to the sand in the column required elemental analysis of the sand surfaces following a breakthrough experiment. After flushing of the column with a solution of appropriate ionic strength conductivity matches that of the QD solution injected, as described in the previous section, the column was allowed to cool before being removed from the system. The injection end (closest to the pump in the flow scheme) was opened and the sand was extruded from the column with light percussive force and collected in pre-weighed sample vials. At first the segment amounts were estimated, and if a column exhibited signs of QD retention such as visible red/orange coloration, the number of collected samples was increased. The samples were dried in an oven for at least 24 h at 70 °C and then weighed again to obtain the dry sample mass of each section and the total mass of sand in the column.

Metal digestion and ICP detection

Each section sample was homogenized by a combination of stirring and shaking in order to ensure that data obtained from the sample would be representative of the entire section. Approximately one gram of each section sample was removed for acid digestion in accordance with protocol developed and made available by the Environmental Protection Agency's (EPA) protocol for digestion of soils and sediments for trace metal detection.[46] Each one gram sample of sand had 10 mL of nitric acid added (VWR International BDR Chemical, trace metal-free) before being heated in a 65 °C water bath for 5 min. An additional 5 mL of trace metal-free nitric acid was then added to each sample and the sample was heated in the water bath for 30 min. The samples were cooled and each sample was diluted either 40% or 8% with deionized water. These samples were then analyzed in triplicate using an ICP-OES (Thermo Scientific) for plasma emission at wavelengths of 214.4, 226.5, 228.8, and 326.1 nm corresponding to energy level changes of elemental cadmium.

Modeling methodology

Modeling was suggested as an additional tool for more completely understanding the causes of QD retention. As examples in literature showed, the modification of governing equations can be used in conjunction with BTC data to clarify mechanisms for colloid retention.[33] A graphic of clean-bed filtration and reversible deposition are shown in Figure 4-6(a) and (b). Lower temperature and IS conditions exhibit more traditional breakthrough curves, exhibited by a gradual increase of concentration over time. Without prior knowledge of surface coverage, a reversible sorption model was applied to the experiments:

$$\theta \frac{dC}{dt} = \theta D \frac{d^2C}{dx^2} - \theta v \frac{dC}{dx} - \theta k_1 C + \rho_b k_r C_S \tag{4.13}$$

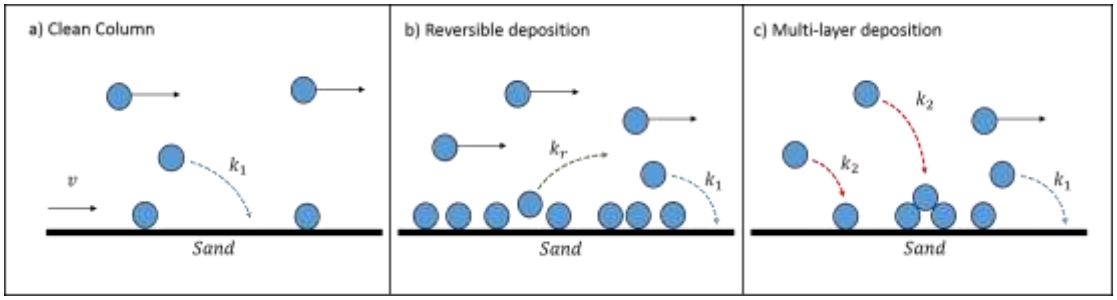

Figure 4-6 – Illustration of proposed colloid behavior near a sand grain surface. Panel (a): initial introduction of colloids to the porous media bed exhibit colloid deposition. Panel (b) shows simultaneous entrainment and deposition of the colloids to and from the fluid phase. Panel (c) is the proposed behavior for a multilayer deposition model.

However, under more extreme conditions, the dimensionless breakthrough concentration was observed to decrease over the course of the experiment. One hypothesis that supports this behavior is a multilayer deposition model, where two dissimilar rate constants cause overall deposition rates to increase with time. A mathematical description for the multilayer deposition BTCs is proposed below:

$$\theta \frac{dC}{dt} = \theta D \frac{d^2C}{dx^2} - \theta v \frac{dC}{dx} - \theta k_1 C - \rho_b k_2 C C_S \tag{4.14}$$

$$\rho_b \frac{dC_s}{dt} = \theta k_1 C + \rho_b k_2 C C_s \tag{4.15}$$

where C and C_s are the concentration of colloids in the fluid and attached to the surface, respectively, θ is the porosity, v is the flow velocity, ρ_b is the bulk density, and k are rate constants. The multilayer deposition model is not commonly used in colloidal transport models. The multilayer aspect is depicted mathematically in the addition of the second rate constant k_2. The rate of fluid phase concentration change will increase as more QDs are deposited onto the surface since k_2 is a function of the concentration of adsorbed QDs. A

Matlab script using the numerical partial differential equation (PDE) solver *pdepe* was developed to optimize the rate constants. The use of the *pdepe* function for 1-D modeling of contaminant transport in porous media, along with a significant amount of framework for numerically solving systems of advective-dispersive-reactive PDEs, was outlined by Holzbecher.[47] The experimental parameters, θ and *v*, were determined from ionic tracer breakthrough. The diffusion parameter was estimated using the Einstein-Smulchowski equation. The modeling results are included as a discussion of the mechanisms involved in QD transport. Extensive effort in literature has been expended to illuminate the physical meaning of the deposition rate constants in terms of experimental parameters. This section, however, is not so comprehensive, and approaches these modeled parameters from a phenomenological perspective.

The experimental boundary conditions offer a unique challenge to modeling, since the concentration change in a pulse injection is very dynamic at the point when the influent is switched from analyte to flush solution. Therefore, modeling both the injection and flush sections of the experiment required three components:

1) The influent concentration is unity, $C(x=0) = 1$, for a period of time $t < t_{bt}$ with background concentrations of QDs equal to zero in both the fluid phase and the adsorbed phase:

   $C(x,t=0) = 0$ and $C_s(x,t=0) = 0$

2) At the time $t = t_{bt}$ the QD concentrations in the fluid and adsorbed phases are extracted from the solution to part (1) (i.e., the concentrations at the final time step at each spatial location and phase) and became the initial condition for the subsequent step

3) At $t \geq t_{bt}$, using the new initial conditions, the behavior of the pulse was modeled using an analyte-free boundary condition: $C(x=0, t) = 0$

The results from both time periods (injection and flush) were then combined and used to

optimize the rate constants. With the presence of QD-QD interaction that is large relative to QD-collector interaction, equations (4.14) and (4.15) show that the concentrations in both phases dictate the overall rate of deposition to the surface. This necessitates recording the spatial concentration of adsorbed QDs at each time step for the mobile phase of the model, equation (4.15). The methodology for modeling this system of PDEs was developed with guidance from Dr. Mark Williams at Pacific Northwest National Laboratory.

Results

Surface potential

The observed change in voltage was plotted against the pressure head. Figure 4-7 shows the experiment data. From equations (4.4) and (4.5), the results of the ionic strength variation at each temperature were calculated at different separation distances in Figure 4-8. The second set of figures show the effect of temperature variation at each ionic strength, Figure 4-9. The QD-QD interaction energy was calculated from the Lin and Wiesner formulation, equation (4.8), and shown below in Figure 4-10 and Figure 4-11.

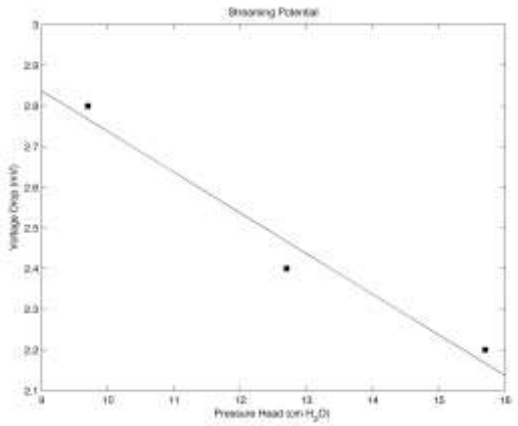

Figure 4-7 - Decreasing potential across the porous medium at different pressure heads due to surface charge. The pH was maintained at 8 and the ionic strength of the solution was 10 mM. From equation (4.10) the surface potential of the Ottawa sand is -180 mV.

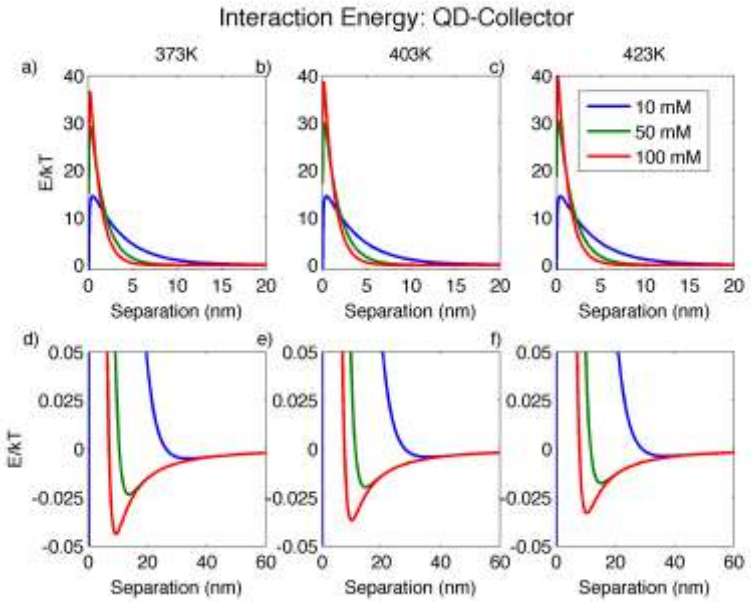

Figure 4-8 - Comparison of the effects of increasing ionic strength to intersurface potential at constant temperature (a-c: energy barrier; d-f: secondary energy minimum) based on the Lin and Weisner formulation.

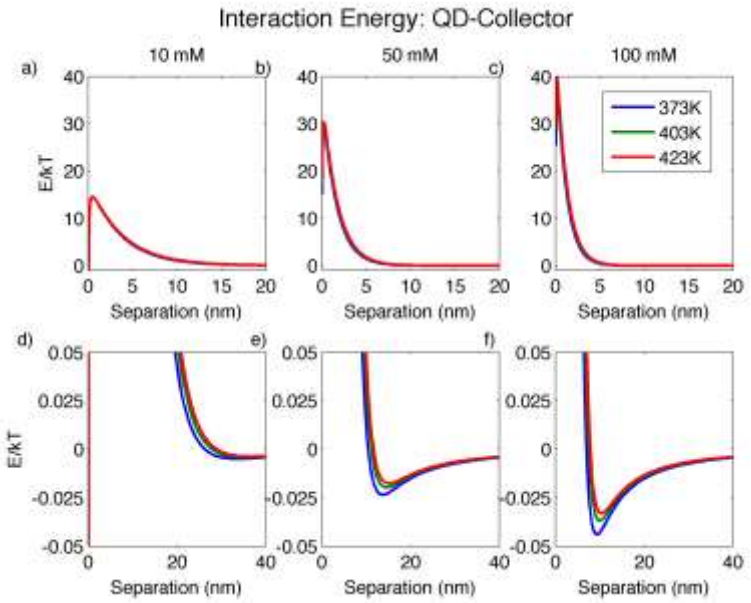

Figure 4-9 - Comparison of the effects of increasing temperature to intersurface potential at constant ionic strength (a-c: energy barrier; d-f: secondary energy minimum) from the Lin and Weisner formulation with Derjaugin approximation.

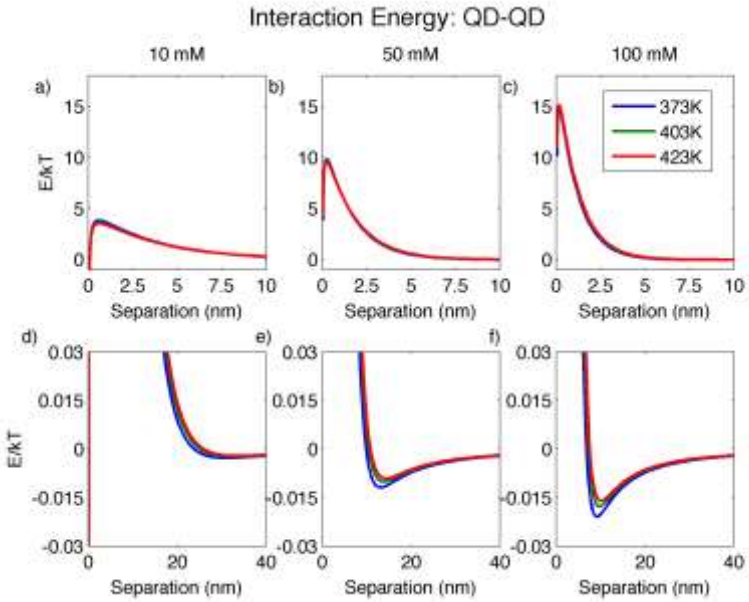

Figure 4-10 - Comparison of the effects of increasing temperature to intersurface potential at constant ionic strength (a-c: energy barrier; d-f: secondary energy minimum) from the Lin and Weisner formulation.

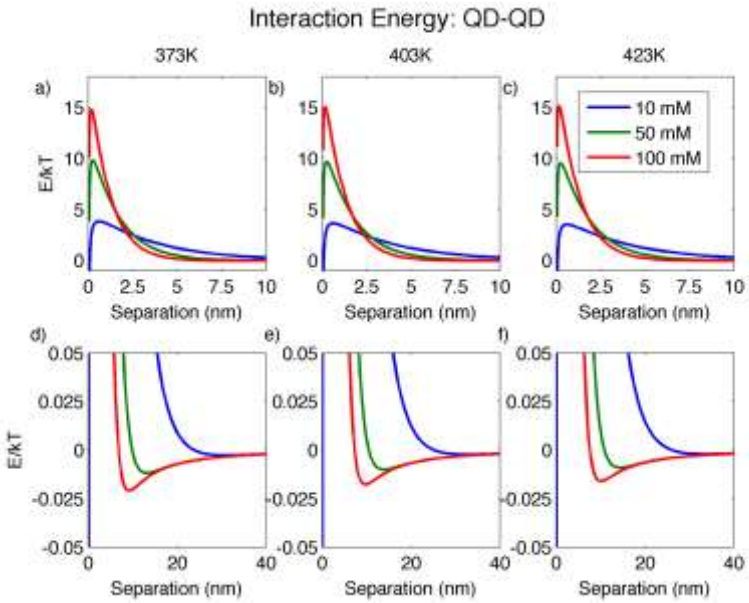

Figure 4-11 - Comparison of the effects of increasing ionic strength to sphere-sphere potential at constant temperature from the Lin and Weisner formulation with Derjaugin assumption (DA).

Quantum dot transport in high-temperature porous media

Results from the set of nine transport experiments are shown in Figure 4-12. From left to right the columns compare increases in temperature of the porous medium, while from top to bottom are the increases in ionic strength for a given temperature. The black lines show the QD detection, while the thin blue lines are the salt BTCs used to measure the conservative tracer behavior and pore volume of each system. For each experiment condition the colloids' leading edge breakthrough volume coincides with the salt BTC. Single pore volume breakthrough is a feature widely associated with conservative tracer behavior, while reactive tracer activity is delayed for a period of time due to interaction with the sediment.

All six of the 10 and 50 ionic strength experiments exhibit a steep leading edge that lies along the salt BTC. The 10 and 50 mM ionic strength experiments at 100 °C have minimal premature breakthrough features, while the 100 mM ionic strength experiment shows a detection feature at 0.75 PV. The background signal for the 100 °C experiments was near zero. Background concentration C/C_0 for the 10 mM ionic strength at 130 °C was between 0.1 and 0.2, with a detection feature at 0.55 PV. Small oscillations were also seen at this temperature for the 50 and 100 mM ionic strength experiments, but they appear to be point events due to signal fluctuation as opposed to a QD concentration variation. For each experiment at 130 °C, the leading edge coincided with the salt BTC. At 150 °C, the 10 mM ionic strength experiment has a breakthrough that matches the salt BTC, although there are premature detection of features at 0.5 and 0.75 PV. This also makes the background signal difficult to establish due to the oscillations in the short-time intensity. The background C/C_0 of 150C50 is approximately 0.2, and has a retarded breakthrough relative to the salt BTC. Experiment 150C100 has minimal background signal, but the breakthrough is difficult to match with the salt BTC due to the low magnitude of the plateau. It appears to be slightly retarded, similar to that seen in experiment 150C50.

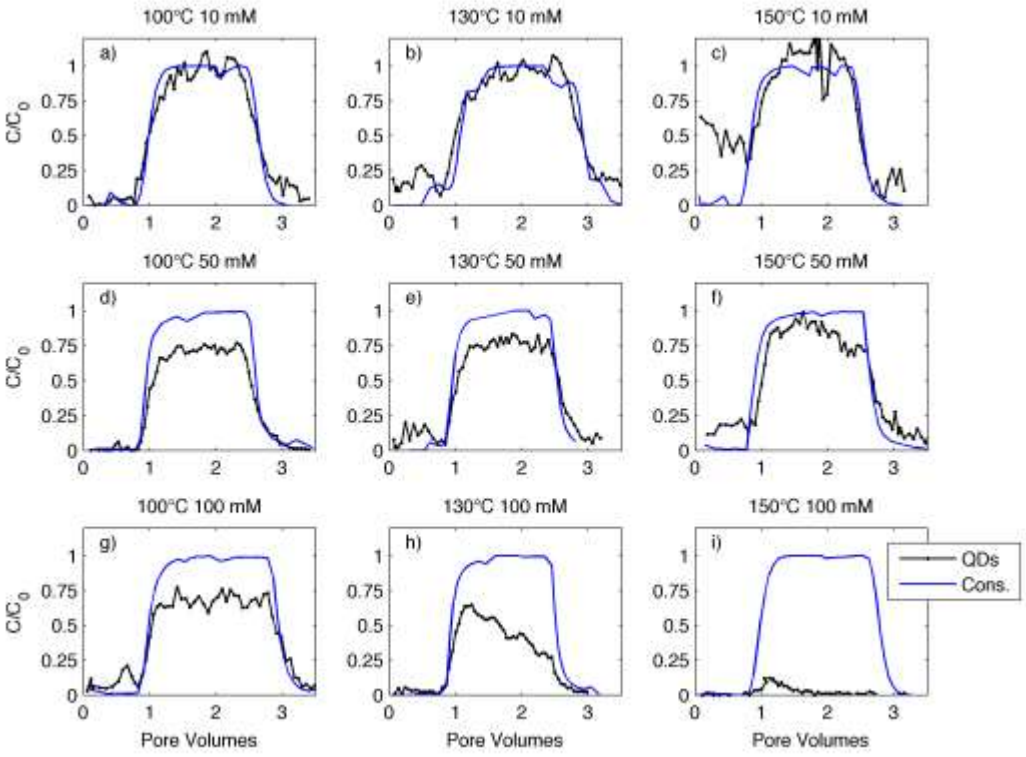

Figure 4-12 - BTCs for temperatures 100, 130, and 150 C and 10, 50, and 100 mM ionic strength. The solid lines with points show the response due to the quantum dot breakthrough, while the dotted lines alone are the conservative ion BTCs (i.e., the salt breakthrough curves).

The behavior of the QD during the steady-state injection time is of particular interest and can be used to determine the types of interactions occurring between the QDs and the sand surfaces. In experiment 100C10, the dimensionless concentration is between 0.9 and 1.1. With an increase in temperature to 130 °C, the BTC profile is stable for the 10 and 50 mM ionic strength solutions, displaying an overall flat steady-state plateau. The 100 °C temperature experiment at high salt concentrations (experiment 100C100) is characterized by a steady-state plateau region that has a slightly lower in intensity than for the lower ionic strengths. Some of the QD BTCs show nonideal trailing edge behavior. For the modest porous medium experimental parameters (low ionic strength, temperature less than 130 °C), the

elution of the QDs coincides with the salt BTC. A further increase in temperature in experiment 150C100 shows a strong amount of QD retention, with minimal breakthrough occurring (C/C_0 ~0.2) at the first pore volume followed quickly by an absence of QD in the effluent. The 150 °C, 50 mM ionic strength experiment (experiment 150C50) is the first that shows indications of tailing behavior. This occurs after a single pore volume injection, a slow decline in the steady-state region and residual tracer in the effluent following the expected tailing breakthrough volume. Late elution of QDs also occurs in experiment 150C50, with very slight tailing also seen in experiment 100C100.

In order to determine the overall percent of injected QDs that were recovered from the column for each experiment, the integrated absorbance spectrum was taken and normalized by the absorbance of the injected QD samples. The C/C_0 was then integrated numerically. The injection volume aliquots of effluent that were collected during the experiment were normalized by the absorbance intensity spectrum of pure QDs, multiplied by the injection volume (QDs in vs QDs out). The percentage of the QDs that were recovered in the effluent, calculated by normalizing the sum of integrated spectra over the PV of the experiment by the total number of spectra per volume injected, are reported in Table 4-3. At 100 °C the recovery between ionic strengths is near 100%. All 10 mM ionic strength experiments also show near complete recovery. The 50 mM ionic strength decreases from 85 to 50% recovery at 150 °C, and the 100 mM ionic strength experiments decrease from 95 to 5% recovery. Overall increases in ionic strength and temperature result in decreases in the QD recovery.

Table 4-3: Percent recovery of quantum dots

Recovery Percentage (%)	**Temperature (°C)**		
Ionic Strength (mM)	**100**	**130**	**150**
10	125	100	105
50	85	80	50
100	95	25	5

Adsorbed cadmium

The ICP method was used to sample clean Ottawa sand to establish the background cadmium detection at 410 counts/gram sand. The results of the cadmium detection assays after the transport experiments are shown in Figure 4-13. The y-axes are the distance along the column, dimensionless from zero to one vertically from the bottom (injection location at the bottom), and the x-axes are log-scales of the cadmium detection counts at 214.4 nm. The experimental parameters for each data are shown in the individual figure titles. The distance between bars indicates the relative amount of sand used for that measurement (i.e., two bars very close to each other indicate small masses of sand in that bin). Overall with the increase of temperature and ionic strength, the magnitude of cadmium detection increases. This is in agreement with the recoveries calculated from the BTC data. The average number of counts per gram of sand is outlined in Table 4-4, ranging from 1.5×10^4 to 4.8×10^5. The number of counts along the column remains near 10^4 as ionic strength increases to 100 mM. The profile of the detected cadmium is highest at the inlet and outlet for experiments 100C10 and 100C50, while experiment 100C100 shows a maximum detection peak only at the inlet. The

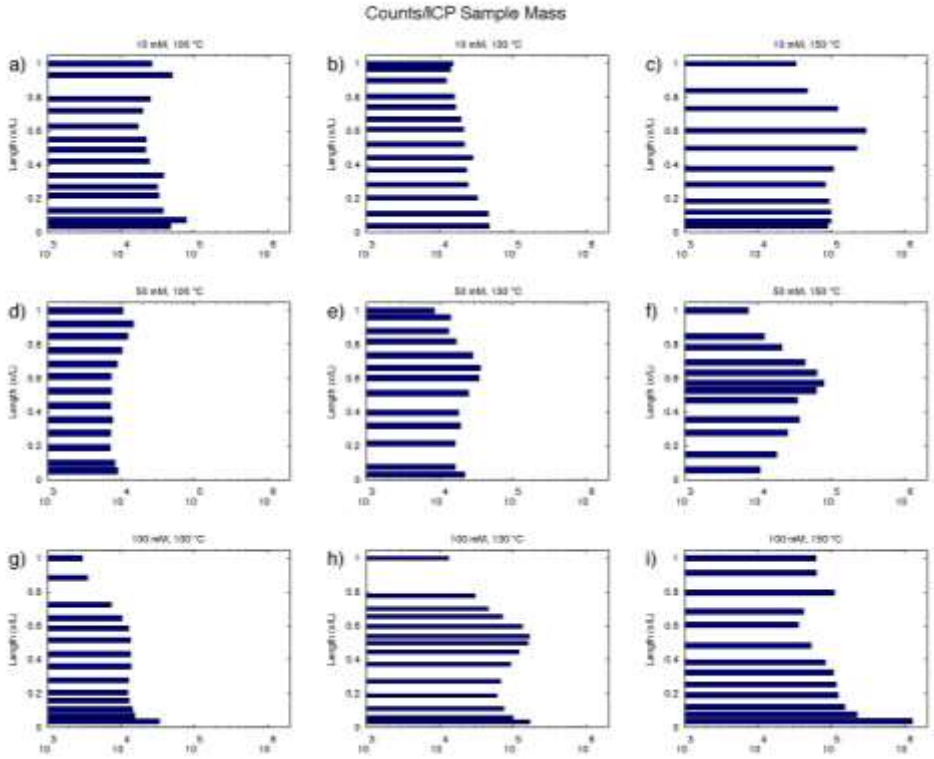

Figure 4-13 - Number of detection events for the 214.4 nm emission band of elemental cadmium for each segment of sand column for each breakthrough experiment. The horizontal axes show the dimensionless length along the column, with the inlet at x/L = 0.

Table 4-4: Average number of counts for cadmium in each section

Average Counts (10^4)			
	100 °C	**130 °C**	**150 °C**
10 mM	6.8	4.2	17.5
50 mM	1.5	3.4	6.1
100 mM	2.7	22.1	48.4

total number of cadmium counts for 10 and 50 mM ionic strength at 130 °C were similar, at 2.2 $x10^6$ and 1.9 $x10^6$ counts, respectively, normalized by the mass of each column. The amount of cadmium detected increased from 1.9 $x10^6$ to 6.7 $x10^6$ counts per mass when the experimental ionic strength was increased to 10 mM. For each experiment at 130 °C, there was a downstream peak located between 45 and 70% of the column length. The 10 mM downstream peak is located at 45% while the 50 and 100 mM peaks are at 65 and 55%, respectively. The approximate peak locations are summarized in Table 4-5. The experimental parameters for each data are shown in the individual figure titles. The distance between bars indicates the relative amount of sand used in that measurement (i.e., two bars very close to each other indicate small masses of sand in that bin.). Overall with the increase of temperature and ionic strength, the detection of cadmium increases.

Discussion

Surface potential measurement

Reported surface potential values for Ottawa sand are lower in magnitude than the value experimentally determined in this research. For example, Johnson found surface potentials for quartz sand to be as low as -55 mV at basic pH, although in the fluid conductivity

Table 4-5: Dimensionless distance location of the downstream concentration peak

Location of Downstream Peak (x/L)			
	100 °C	**130 °C**	**150 °C**
10 mM	0.9	0.45	0.6
50 mM	0.9	0.75	0.55
100 mM	-	0.5	0.8

range of interest (400-5000 μS/cm) the values decreased to around -30 mV. Similar values were reported by Kaya et al., using crushed Ottawa sand as the quartz surface of interest.[41,48] Reported values for Ottawa sand are lower in magnitude than the value experimentally determined in this research.

Interaction potential energy

At each temperature the increase of ionic strength results in an increase in the primary energy barrier near the collector surface. This is coupled with a "sharpening" of the barrier, that is, the range of influence of the charged surface decreases with an increase in ionic strength. Mathematically this is seen in exponential decay with respect to κ in equation (4.4), though dampened by the preexponential term γ of equation (4.6) (reposted below).

$$\Delta V_{El} = \frac{64\pi\epsilon}{\kappa}\left(\frac{kT}{ze}\right)^2 \gamma_1\gamma_2 \left[\left(\kappa r_p - 1\right)\exp(-\kappa h) + \left(\kappa r_p + 1\right)\exp\left(-\kappa\left(h + 2r_p\right)\right)\right] \tag{4.4}$$

$$\gamma_i = \tanh\left(\frac{z_i e\psi_i}{4kT}\right) \tag{4.6}$$

$$\kappa = \left[\frac{e^2\left(\sum n_i z_i^2\right)}{\epsilon\epsilon_0 k_B T}\right]^{1/2} \tag{4.7}$$

Figure 4-8a-c show that the height of the energy barrier increases from 12 kT at 10 mM to 33 kT at 100 mM, an approximately three-fold increase. For 10 mM the barrier is ~12 kT at all temperatures, increasing to ~25 kT for 50 mM and further to ~33 kT at 100 mM. The potential energy curves are independent of temperature at distances over 30 nm, as is shown

by the convergence of the curves under each experiment condition (Figure 4-9 and Figure 4-10).

Previous studies have shown that a secondary energy minimum in the interaction potential is also a mechanism for colloid retention in porous media.[11,12,16,19,30,49] A small secondary energy minimum was observed for all experimental conditions. This is shown in Figure 4-8d-f and Figure 4-9d-f. Increasing the ionic strength results in two interesting feature changes. First, the absolute depth of the potential well increases from 0.01 kT to 0.04 kT with an ionic strength increase from 10 to 100 mM. Second, there is a shift in the distance from the surface where the attraction is strongest. Both of these coincide with the rapid deterioration of the repulsive energy at increasing distance from the charged surface. Torkzaban et al. found that the location of the energy well was an important factor due to the hydrodynamic drag forces. Fluid velocity increases at increasing distance from the surface due to the friction/"no-slip" condition.[31] In a potential well, the colloid experiences the electrostatic force in that well and the hydrodynamic drag force. A colloid in a well further from the surface will experience larger drag forces and is more likely to be removed from the well than a colloid in a well nearer the surface. In these experiments, with larger attractive potential near the surface, the profiles for increasing ionic strength suggest that retention of QDs will also increase. The temperature does not have as strong an influence on the shape of interaction energy profile as the ionic strength. The changes of the secondary minimum with temperature are minimal, on the order of 10^{-3} kT for each ionic strength. This result shows that increasing the temperature at a set ionic strength will not result in increased secondary well retention of colloids.

It is apparent that the stability of the QDs in solution is not sensitive to increases in temperature, since the energy barrier does not deviate significantly. With an increase in ionic strength, the primary energy barrier magnitude increases, as does the sharpness of the peak.

The sharpening of the peak is again attributed to the shortening of the Debye screening length and development of the secondary minimum. Furthermore, comparing the height of energy barrier between sphere-plate and sphere-sphere is important to investigate if multilayer deposition is a reasonable model. Across all the experimental conditions the height of the energy barrier decreases, showing that permanent QD-QD interaction (agglomeration) is more likely than permanent QD-collector interaction (deposition). The increase in primary energy barrier as salinity increases was observed and discussed in Lin et al. as a paradox where electric double layer calculations do not adequately predict behavior of nanoparticles that cause failure of the Derjaugin condition (low ionic strengths and small particles). The lack of significant existing literature indicates the difficulty of applying EDL and electrostatic theories to QDs that have pseudo-colloidal properties and extremely high ratios of surface atoms relative to total atoms.

It is immediately evident that all of the QD BTCs exhibit leading edge conservative tracer breakthrough behavior, although under different conditions they have different steady-state plateau profiles and retention. This indicates that there is minimal axial dispersion of the colloids within the column. This is supported by the similarity in shape of each BTC leading edge regardless of temperature. Even at high temperatures, where water viscosity is lowest and diffusion would be highest, the QDs exhibit minimal deviation from the ionic tracer breakthrough. The similarity is due to the dominance of mechanical dispersion over the temperature-dependent diffusivity. This is likely due to a combination of two possible factors. First, using the same procedure to pack the columns leads to flow paths that are indistinguishable between experiments. Second, the system may not be large enough for tortuous flow paths to become clear in the QD breakthrough.

The presence of premature breakthrough in experiments 130C10, 150C10, 150C50, and 100C100 in Figure 4-12d, g, h, and c shows that a small fraction of injected QDs are being

excluded from small pores or are otherwise sweeping a smaller volume of the porous bed. The large initial values for the integrated intensity in experiment 150C10 at one PV are due to the elution of slightly turbid solution which scatters significant amounts of light. BTCs for which size exclusion affects transport behavior would exhibit breakthrough volumes smaller than the pore volume due to the smaller effective volume experienced by the tracer. The QDs used in these experiments exhibit narrow size distribution, a primary reason for their intensive study in chemistry and materials science. This was supported with earlier DLS size measurements that showed the QDs had an approximate diameter range of 5 nm. The QDs that do not breakthrough early arrive simultaneously with the ionic tracer breakthrough, consistent with conservative tracer behavior.

For low ionic strength and temperature, transport behavior over the entire course of the injection is conservative. This conservative behavior is shown in Figure 4-12. Increase in temperature without an increase in ionic strength shows development of attachment behavior, with recovery decreasing from 100 to 25% at 130 °C and from 100 to 5% at 150 °C. Regardless, the QD breakthrough is not retarded with respect to the salt breakthrough volume, which is consistent with a decreased Debye length. While the BTCs of experiments 100C50, 130C50, and 100C100 (Figure 4-12d, e, and g) all exhibit retention, they do not show the increasing concentration profile (positive slope over the steady-injection period) that is evidence of a finite number of adsorption sites. From these studies, it can be concluded that QD transport behavior at elevated temperature differs from traditional colloid transport where concentration increases as adsorption sites are filled.[8,16,25,50,51] Previous results from experiments involving ionic strength variation at room temperature do not always apply when the temperature is increased.

Further increase in temperature in experiment 150C50 shows that there is more retention of the QDs, with recoveries at 50 mM decreasing from 85 to 50% from 100 to 150

°C. The presence of tailing behavior is evidence that some of the QDs are being held longer in the column and are eluting less frequently, indicating an attractive force, either of chemical or electrostatic nature, exists between the QD and collector. The nonretarded breakthrough partnered with a general decrease in QD intensity shows that some of the QDs do not interact with the sand at all. Only a fraction of interactions between QDs and sand surfaces have the attractive forces necessary to withhold the QDs and only do so for a short time period. For 100 mM at 100 °C, there is steady breakthrough plateau at 60% of the maximum QD concentration, with minimal tailing behavior. Increased retention and the development of tailing occur with an increase in temperature in experiments 130C100 and 150C100. Experiment 130C100 exhibits initial breakthrough concentrations in agreement with the data from experiment 100C100 (~60%) but tails off with time. Retention events within the column are increasing and leading to decreasing concentration of QDs in the effluent. This is an uncommon phenomenon in colloid transport, but the development of tailing suggests that the retention mechanism is temperature-dependent. This is consistent with a multilayer deposition model involving two sets of kinetics as described earlier.

Adsorbed cadmium

The profiles of the 100 °C experiments do not indicate strong colloid-to-surface deposition, as the detection of adsorbed cadmium via ICP in experiments 100C10 and 100C50 is locally maximum near the inlet and the outlet. Since the predicted distribution for irreversible colloid deposition would have a maximum at the inlet, there is a fraction of colloids that are not permanently retained. These colloids translate through the column slowly. There is also a fraction of QDs that are preferentially retained near the inlet. In our system, there is no evidence of competition for adsorption sites, and consequentially, other possibilities need to be entertained. Continued injection of QD-free background solution

would eventually lead to elution of the QDs that are strongly adsorbed in the column. The additional retention is also seen in the differences in the BTCs since recovery in experiment 100C10 is 95% and decreases in experiment 100C50 to 75%. This late-time feature is not seen in the subsequent increase in ionic strength to 100 mM and the overall magnitude of cadmium detection is similar (~10^4 counts/gram). In experiment 100C100, Figure 4-13g, there are more counts of cadmium detection early in the column, a commonly observed feature with colloidal retention. This is attributed to primary attachment (irreversible immobilization of QDs on the surface) or pore-throat straining by the colloids.

At 130 °C there are similar trends to those observed at 100 °C. The 10 mM ionic strength experiment shows a decline of cadmium detected along the column, showing that the high concentration of QDs introduced at the inlet became irreversibly bound to the sand surfaces. From the energy interaction profile, the lowest primary energy barrier calculated corresponds to the 10 mM solution, although from trends at 100 °C the primary well was determined not to be the primary retention mechanism since increased retention was seen despite an increase of the energy barrier with ionic strength. The BTC for experiment 130C10, Figure 4-12b shows there is a very slight increase over the steady-state period, corresponding to previously developed treatment of porous media with a finite amount of attachment locations. The colloids at 130 °C have greater thermal energy to overcome the primary energy barrier and become permanently attached. From the 100% recovery calculated from the BTC of experiment 130C10, shown in Table 4-3, the fraction of total QDs that follow this behavior is very small. Furthermore, all of the counts of cadmium from the ICP, even for the lowest amounts at experiment 100C10 are at least five times the baseline count measured from unused, clean sand. For increased ionic strength and temperature conditions the counts of cadmium many orders of magnitude more than the baseline. This result confirms that the counts of cadmium are all associated with QD retention events.

As the ionic strength is increased from 10 mM to 50 and 100 mM at 130 °C, there is a decrease in QD mobility shown by the downstream peaks closer to the inlet in Figure 4-13e and h, in addition to the development of a local maximum at the inlet. For 50 mM, there is increased interaction due to the increased depth of the secondary energy minimum that was previously reported. Stronger interaction helps explain the recovery decrease from 100 to 80% calculated from the BTC. This means that retention increases by about 20% compared to the 10 mM experiment and the surface sites become more favorable for attachment. The QD attachment increases further at 100 mM, with recovery decreasing to 25% of the total QDs injected. The retention of QDs is particularly dramatic at the inlet sections of the column that the first ~8% of the column contains ~30% of the detected cadmium. There is increased secondary well depth at this ionic strength that causes increased retention, most likely due to its near-surface location of 10 nm. This was proposed in literature to increase retention due to lower hydrodynamic drag forces acting on the colloids.[8,31,52] There is evidence of QD mobility at high ionic strength in the form of the secondary peak downstream from the inlet, suggesting that the QDs do not overcome the primary energy barrier predicted by the double layer interaction.

Decreased mobility is a sign of either QDs located closer to the collector surfaces or stronger attractive forces, both of which are predicted by the double layer interaction calculations. The BTC from experiment 130C100 is particularly interesting since it begins to show significantly different colloid transport behavior compared to experiments under more moderate environment conditions. For permanent retention with finite sites, there is a general increase in concentration over the steady-state period, but in these experiments a general decrease was observed. This trend is not common in colloidal transport behavior at ambient temperature and there is very little existing research on high temperature porous media transport. Once QDs are retained, they do not become entrained in the mobile phase

again, but they are not necessarily deposited where the concentration gradient is largest. The strength of interaction does not fully extend to all QDs in the pore spaces, as shown by initial breakthrough concentrations between 0.7-0.8 (i.e., only 20% of the QDs initially injected experience forces strong enough for permanent retention). Over the course of the injection the BTC declines, suggesting that the retention kinetics are time-dependent. Once the QDs adsorb to the surface then they preferentially filter out subsequently injected QDs due to the lower primary interaction barrier relative to the sphere-collector. The shape of the ICP peak shows a mobile slug of QDs traveling through the column. This indicates that favorable retention conditions are not experienced by each QD. The decline of the plateau that occurs when the ionic strength is doubled from 50 to 100 mM at 150 °C is dramatic. The BTC QD recovery declined from 80% at 50 mM to 10% at 100 mM. This correlates with a 10-fold increase in detected cadmium on the sand surface. The interaction potential shows a deep near-surface secondary energy minimum under these conditions, and quick trapping of QDs led to secondary aggregation and more favorable QD retention. The increased ionic strength makes retention more favorable, particularly in the first 3% of the column where there is 10 times as much cadmium detected compared to the 50 mM experiment condition at 150 °C. The high concentration of QDs injected at the inlet increases the flux of QDs towards the sand surface, although less favorable retention conditions result in slower adsorption rates. The clean filtration bed retains 80% of the initial QD injected while secondary interactions with these QDs subsequently propagate retention and lead to rapid decrease in the amount of QDs eluted.

Surface analysis and transport

In Figure 4-12, there is strong evidence that retention changes with increases of either ionic strength or temperature. The ionic strength effect has been documented in literature and retention profiles have been connected to double layer potential and advection-diffusion in the column.[2,16,17,53] The increase of the secondary minimum with ionic strength at ambient temperatures is the dominant mechanism for colloid retention, while the primary energy well and secondary adsorption coincide with the location of peaks near the inlet. As temperature and ionic strength increase, the grain surfaces become more favorable for attachment, along with the development of a secondary peak downstream from the inlet. This is most apparent in three experiments: 130C100, 150C10, and 150C50, Figure 4-13h, c, and f. The BTCs for these experiments do not have common features that might link them to the downstream peak, such as tailing or delayed breakthrough that are associated with mobility and reversible attachment. The location of the secondary deposition peak between 45-70% into the column suggests that the behavior of the QDs in the column is impacted by similar mechanisms. This is earlier than the retention of experiment 130C50 and shows the increased interaction between the QDs and collectors in the higher temperature environment. This results in slower transport through the column. Increasing temperature has a minimal effect on the primary energy barrier, and decreases the secondary energy minimum, so the source of the increased interaction is weakly dependent on temperature. The visible decrease of QD concentration during the steady-state period indicates QD-QD interaction that results in retention by previously adsorbed QDs. The QD-QD interaction energies are reported in Figure 4-8 through Figure 4-11. The secondary energy minimum of QD-QD interaction is weaker than the secondary minimum calculated for QD-surface, but the primary energy barrier for QD-QD is lower than for QD-surface. This suggests that at high temperatures and ionic strength, the multilayer deposition is due to QDs overcoming primary

energy barriers and becoming more strongly attached to other QDs. The peaks of the 100 °C data are the weakest of all the surface data. Coupled with the high recovery rates these weak peaks show that downstream retention develops with increased salinity. This corresponds to the increase in the secondary potential well with ionic strength, but the lack of sensitivity to temperature results in QDs that translate along the surface and deposit downstream. The low temperature behavior is more like that predicted by Becker et al. who observed an *increase* in the amount of colloids retained along the length of the column.[33]

Modeling

The results of the reversible sorption (equation (4.13)) and dual-parameter (equations (4.14) and (4.15)) optimizations are below in Figure 4-14. Model solutions (red line) are compared with the experimental observations (blue markers). Figure 4-14 summarizes optimizations using the Matlab *fminsearch* function to optimize *pdepe* for either reversible, single layer deposition, or dual-deposition models. The dual-deposition equations failed to model the trends of the more moderate experimental conditions under 130 °C or under 50 mM IS. The gradual BTC concentration increase occurring at low temperatures and ionic strengths indicates irreversible sorption on a finite number of sites. In many types of molecular tracer applications, using reversible tracers is beneficial for estimating the surface area of a swept reservoir. It is possible that the adsorbed QDs in some of these systems are becoming entrained into the mobile phase and subsequently transport through the reservoir. If the secondary deposition is assumed to be negligible compared to the rate of QD release, equation (4.9) is obtained. The values of k_1 and k_r in equation (4.14) were optimized with the data, and are displayed in Figure 4-14 for six experiments: 100C10, 100C50, 100C100, 130C10, 130C50, and 100C10. At low ionic strength and temperatures the reversible attachment model is able to match the inclined steady-state plateau of low ionic strength

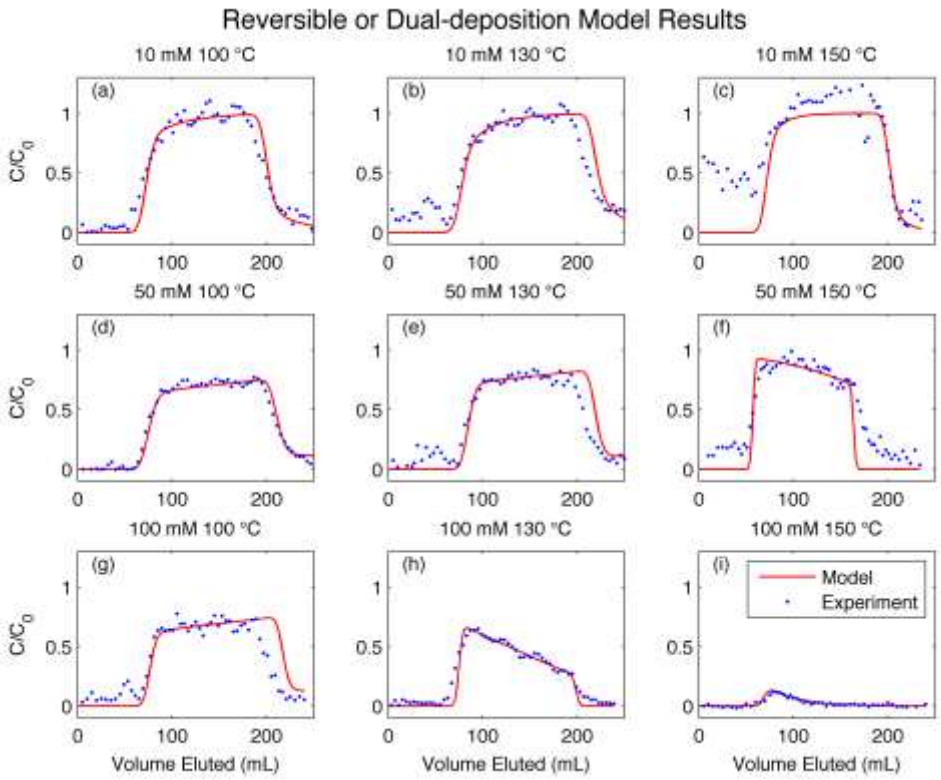

Figure 4-14 - Results of using *fminsearch* function to optimize *pdepe*, two parameter fitting. Panels a-e and g show reversible adsorption following equation (4.13). Panels f, h, and i show irreversible, dual-deposition model following equations (4.14) and (4.15).

experiments 100C10, 130C10, 100C50, 130C50, and 150C10, Figure 4-14a, b, d, e, and g. The reversible fitting model is an attempt to identify differences in columns with less retention. The BTC from experiment 100C50 shows a slightly increasing concentration profile and the reversible model is able to portray the plateau (Figure 4-14 (d)). This result is also seen in both the 10 mM ionic strength experiments at 130 and 150 °C (Figure 4-14b and c), but the effect decreases as QD-QD interaction begins to dominate the transport and retention of the QDs. Finally, the reversible fitting matches some of the tailing behavior of the experiments, particularly experiments 100C10, 130C10, and 100C50, panels a, b, and d.

The solution to the dual-deposition model, equations (4.14) and (4.15), are shown in Figure 4-14f, h, and i. They suggest that multilayer deposition is responsible for the decreasing QD concentration profile of the BTCs. This is represented by the added kinetic attachment term in the updated model. High initial breakthrough concentrations near the pore volume indicate that QDs were preferentially transported rather than adsorbed, represented by a low primary kinetic attachment parameter k_1. Generally, the primary deposition parameter k_1 for all experiments was on the order of 10^{-3} to 10^{-4} s^{-1}.For dual layer deposition, the secondary parameter k_2 was five magnitudes higher. This indicates that the initial deposition is slow, shown by the lack of retardation of the concentration front in Figure 4-14f, h, and i. Once colloids are deposited upon the surface, however, subsequent deposition occurs rapidly, as seen in the decrease in concentration profile during QD injection. Experiment 150C100, Figure 4-14i, shows that this decrease can occur extremely rapidly once QDs become deposited, and can be accurately modeled with a surface concentration-dependent parameter in the governing equation. Finally, an attempt was made to reconcile the governing equations (4.13), (4.14), and (4.15) into a three-parameter, dual deposition with reversible adsorption model. A three-parameter optimization routine resulted in significant uncertainty in modeling, and should be considered with significant skepticism. Regardless, for the majority of the experiments, the three-parameter fitted models are very similar to the two-parameter results, or did not satisfactorily fit the experimental data and were not included in this report.

Conclusions

Surface potential

Determining the potential energy field that exists between two charged surfaces has been the challenge for the field of colloid transport for many years. Difficulty lies within the intricacies of the geometry in the system and the complexity of the governing mathematics, though slowly efforts have made progress towards resolving extreme cases. Overcoming the primary energy barrier or becoming withheld in a secondary energy minimum has linked features in the energy profile to the retention of colloids. For future work in QD transport, investigation of the electrical properties of the QDs and the porous medium are relevant for predicting degrees of retention. Large primary and secondary features are present for Ottawa sand with -180 mV surface potential and QDs with zeta-potentials between -28 to -70 mV. The primary barrier increases with higher ionic strengths, while the depth of the secondary barrier also increases. The temperature impact on the energy features is much less significant than that of the ionic strength. This suggests that for colloid transport, high ionic strength environments will result in secondary deposition over primary deposition compared between temperatures. Finally, the strength of the primary QD-QD interaction is lower than the QD-surface interaction. This means interparticle agglomeration is more likely to occur and indicates the presence of multilayer deposition in porous medium transport experiments.

Quantum dot transport

The field of colloid transport has an extensive history due to its importance in colloid-facilitated transport of radionuclides. More recently, their increase in industrial and research applications and subsequent possibility of introduction into the subsurface has led to the study of their transport properties and retention mechanisms. The presence and

concentration of ions in solution were quickly identified as critical parameters, suggesting that retention mechanisms for colloids are centered on electrostatic features. The focus of colloid transport research has focused so much on prevention of mobilization in groundwater aquifers that studying elevated porous bed temperature creates a host of new experiments to study QD transport. Multiple pore volumes were injected at 100, 130, and 150 °C at ionic strengths of 10, 50, and 100 mM, made up of sodium citrate. The QD concentrations were measured in the effluent using absorption spectroscopy at intervals between 3-6 mL. The BTCs show that at low ionic strengths and moderate temperatures of 100 °C that the QDs behaved like conservative tracers, with no retardation, tailing, or retention. The retention increases with higher temperature or ionic strength. Recovery decreased from 100% at low ionic strengths to 5% at 150 ˚C and 100 mM ionic strength. Higher ionic strength leads to decreased recovery at moderate temperatures, consistent with decreased shielding distance between charged QDs and collectors, and declining BTC concentrations at high temperatures. Dual-layer deposition where QD-collector interactions are slow and weak, but QD-QD interactions are fast and occur preferentially at high temperatures and ionic strengths, and lead to time-dependent retention kinetics that increase as QDs are injected into the column.

The BTCs of QDs in the porous media showed that at moderate conditions, the colloid transport behaves similarly to early studies at room temperature. The similarities continue as the temperature and ionic strength are increased, increasing the retention as predicted by earlier ionic strength experiments but deviating from predicted BTC concentration profiles. It is important in porous media transport to understand the fate of all introduced materials. The BTCs show that retention events are occurring, but they do not fully explain the mechanisms. Further experiments for adsorbed cadmium detection can offer additional insight into the nature of the QD adsorption.

Adsorbed cadmium

The BTCs in Ottawa sand showed that QDs flowing through the porous media underwent varying degrees of clean bed filtration. In order to better understand the fates of the QDs, a standard procedure using atomic adsorption spectroscopy was used for trace metal detection from sediment surfaces. The background shows that a porous medium that is exposed to QDs at high temperature exhibits a signal seven times larger than the smallest experimental value. As the temperature and ionic strength of the injection increased, the overall amount of cadmium detected from the grain surfaces increased from $7.5x10^5$ counts/gram at 100C50 to $2.0 x10^7$ counts/gram for 150C100. This represents an increase in favorable retention. The deposition profiles show that the QDs within the columns do not exhibit log-linear deposition behavior due to reversible mobility. Downstream peaks are prominent in 130C50, 130C100, 150C10, and 150C50, showing that at low temperatures QDs will behave more conservatively but will exhibit reactive tracer behavior as temperature increases.

Modeling

The addition of colloid-collector and colloid-colloid adsorption rates to the governing transport equations provides the framework for modeling of the experimental BTCs. The internal Matlab function *pdepe* was used in conjunction with optimization routines to determine the kinetic rate parameters. Overall, both two- and reversible-parameter fitting mechanisms provided curves that are in agreement with the experimental results. The trend of the BTC models showed a transition from a positive steady-state region at lower ionic strengths and temperatures to dramatically decreasing concentrations over the injection period. The reversible-parameter model results show that reversibility of colloid-collector interaction decreases with increased ionic strengths and temperatures, while the adsorption

parameter increased. Furthermore, the adsorption parameter k_1 is a strongly determining factor in the overall intensity of the maximum breakthrough concentration, while the QD-QD parameter k_2 dictates the shape of the BTC profile. These first approximation results support earlier inferences concerning the role the QD-QD interaction plays in high temperature porous media.

References

(1) Israelachvili, J. N. *Intermolecular and Surface Forces*; Academic Press, 2010.

(2) Lin, S.; Wiesner, M. R. *Langmuir* **2012**, *28* (30), 11032–11041.

(3) Bhattacharjee, S.; Elimelech, M. *J. Colloid Interface Sci.* **1997**, *193* (2), 273–285.

(4) Gregory, J. *J. Colloid Interface Sci.* **1975**, *51* (1), 44–51.

(5) Huber, M. L.; Perkins, R. A.; Laesecke, A.; Friend, D. G.; Sengers, J. V.; Assael, M. J.; Metaxa, I. N.; Vogel, E.; Mareš, R.; Miyagawa, K. *J. Phys. Chem. Ref. Data* **2009**, *38* (2), 101–125.

(6) Rose, P. E.; Leecaster, K.; Mella, M.; Ayling, B.; Bartl, M. H. *AGU Fall Meet. Abstr.* **2011**, *32*, 04.

(7) Rose, P. E.; Benoit, W. R.; Kilbourn, P. M. *Geothermics* **2001**, *30* (6), 617–640.

(8) Sasidharan, S.; Torkzaban, S.; Bradford, S. A.; Dillon, P. J.; Cook, P. G. *Colloids Surf. Physicochem. Eng. Asp.* **2014**, *457*, 169–179.

(9) Torkzaban, S.; Kim, H. N.; Simunek, J.; Bradford, S. A. *Environ. Sci. Technol.* **2010**, *44* (5), 1662–1669.

(10) Saiers, J. E.; Lenhart, J. J. *Water Resour. Res.* **2003**, *39* (1), 1019.

(11) Johnson, W. P.; Tong, M.; Li, X. *Water Resour. Res.* **2007**, *43* (12), W12S13.

(12) Johnson, W. P.; Tong, M. *Environ. Sci. Technol.* **2006**, *40* (16), 5015–5021.

(13) Kini, G. C.; Yu, J.; Wang, L.; Kan, A. T.; Biswal, S. L.; Tour, J. M.; Tomson, M. B.; Wong, M. S. *Colloids Surf. Physicochem. Eng. Asp.* **2014**, *443*, 492–500.

(14) Taghavy, A.; Mittelman, A.; Wang, Y.; Pennell, K. D.; Abriola, L. M. *Environ. Sci. Technol.* **2013**, *47* (15), 8499–8507.

(15) Huynh, K. A.; Chen, K. L. *Environ. Sci. Technol.* **2011**, *45* (13), 5564–5571.

(16) Shen, C.; Li, B.; Huang, Y.; Jin, Y. *Environ. Sci. Technol.* **2007**, *41* (20), 6976–6982.

(17) Li, X.; Scheibe, T. D.; Johnson, W. P. *Environ. Sci. Technol.* **2004**, *38* (21), 5616–5625.

(18) Sasidharan, S.; Torkzaban, S.; Bradford, S. A.; Dillon, P. J.; Cook, P. G. *Colloids Surf. Physicochem. Eng. Asp.* **2014**, *457*, 169–179.

(19) Johnson, W. P.; Pazmino, E.; Ma, H. *Water Res.* **2010**, *44* (4), 1158–1169.

(20) Bradford, S. A.; Simunek, J.; Bettahar, M.; Tadassa, Y. F.; van Genuchten, M. T.; Yates, S. R. *Water Resour. Res.* **2005**, *41* (10), W10404.

(21) Johnson, W. P.; Ma, H.; Pazmino, E. *Environ. Sci. Technol.* **2011**, *45* (9), 3831–3832.

(22) Ma, H.; Pazmino, E.; Johnson, W. P. *Langmuir* **2011**, *27* (24), 14982–14994.

(23) Bradford, S. A.; Simunek, J.; Bettahar, M.; Van Genuchten, M. T.; Yates, S. R. *Environ. Sci. Technol.* **2003**, *37* (10), 2242–2250.

(24) Petosa, A. R.; Jaisi, D. P.; Quevedo, I. R.; Elimelech, M.; Tufenkji, N. *Environ. Sci. Technol.* **2010**, *44* (17), 6532–6549.

(25) Painter, S.; Cvetkovic, V.; Pickett, D.; Turner, D. R. *Environ. Sci. Technol.* **2002**, *36* (24), 5369–5375.

(26) Kuhnen, F.; Barmettler, K.; Bhattacharjee, S.; Elimelech, M.; Kretzschmar, R. *J. Colloid Interface Sci.* **2000**, *231* (1), 32–41.

(27) Bradford, S. A.; Yates, S. R.; Bettahar, M.; Simunek, J. *Water Resour. Res.* **2002**, *38*, 1327.

(28) Oncsik, T.; Trefalt, G.; Csendes, Z.; Szilagyi, I.; Borkovec, M. *Langmuir* **2014**, *30* (3), 733–741.

(29) Trefalt, G.; Szilagyi, I.; Borkovec, M. *J. Colloid Interface Sci.* **2013**, *406*, 111–120.

(30) Tong, M.; ma, H.; Johnson, W. P. *Environ. Sci. Technol.* **2008**, *42* (8), 2826–2832.

(31) Torkzaban, S.; Bradford, S. A.; Walker, S. L. *Langmuir* **2007**, *23* (19), 9652–9660.

(32) Christiane Shani, N. W. *Colloids Surf. Physicochem. Eng. Asp.* **2008**, *316* (1-3), 142–150.

(33) Becker, M. D.; Wang, Y.; Pennell, K. D.; Abriola, L. M. *Environ. Sci. Nano* **2015**, *2* (2), 155–166.

(34) Amy Lauren Dale, G. V. L. *Env. Sci Nano* **2014**, *2* (1).

(35) Praetorius, A.; Tufenkji, N.; Goss, K.-U.; Scheringer, M.; Kammer, F. von der; Elimelech, M. *Environ. Sci. Nano* **2014**, *1* (4), 317–323.

(36) Torkzaban, S.; Walker, S. L.; Bradford, S. A. *Water Resour. Res.* **2009**, *45* (9), W09604.

(37) Johnson, W. P.; Li, X.; Tong, M.; Ma, H. *Water Resour. Res.* **2009**, *45* (9), W09603.

(38) Tufenkji, N.; Elimelech, M. *Environ. Sci. Technol.* **2004**, *38* (2), 529–536.

(39) Johnson, W. P.; Li, X.; Yal, G. *Environ. Sci. Technol.* **2007**, *41* (4), 1279–1287.

(40) Erickson, D.; Li, D. *J. Colloid Interface Sci.* **2001**, *237* (2), 283–289.

(41) Johnson, P. R. *J. Colloid Interface Sci.* **1999**, *209* (1), 264–267.

(42) Szymczyk, A.; Fievet, P.; Foissy, A. *J. Colloid Interface Sci.* **2002**, *255* (2), 323–331.

(43) Rabani, E. *J. Chem. Phys.* **2002**, *116* (1), 258–262.

(44) Bradford, S. A.; Bettahar, M. *J. Contam. Hydrol.* **2006**, *82* (1–2), 99–117.

(45) Yu, W. W.; Qu, L.; Guo, W.; Peng, X. *Chem. Mater.* **2003**, *15* (14), 2854–2860.

(46) Recovery, U. E. O. O. of R. C. and. 3000 Series Methods http://www3.epa.gov/epawaste/hazard/testmethods/sw846/online/3_series.htm (accessed Oct 13, 2015).

(47) Holzbecher, E. *Environmental Modeling*; Springer Berlin Heidelberg: Berlin, Heidelberg, 2012.

(48) Kaya, A.; Yukselen, Y. *Can. Geotech. J.* **2005**, *42* (5), 1280–1289.

(49) Kuznar, Z. A.; Elimelech, M. *Colloids Surf. Physicochem. Eng. Asp.* **2007**, *294* (1–3), 156–162.

(50) Quevedo, I. R.; Tufenkji, N. *Environ. Sci. Technol.* **2012**, *46* (8), 4449–4457.

(51) Treumann, S.; Torkzaban, S.; Bradford, S. A.; Visalakshan, R. M.; Page, D. *J. Contam. Hydrol.* **2014**, *164*, 219–229.

(52) Uyusur, B.; Darnault, C. J. G.; Snee, P. T.; Kokën, E.; Jacobson, A. R.; Wells, R. R. *J. Contam. Hydrol.* **2010**, *118* (3–4), 184–198.

(53) Elimelech, M. *J. Colloid Interface Sci.* **1994**, *164* (1), 190–199.

CHAPTER 5

OPTICAL DETECTION OF TRACER SPECIES IN STRONGLY SCATTERING MEDIA

Reproduced with permission from Brauser E. M., Rose P.E., McLennan J.D., and Bartl M.H. Optical detection of tracer species in strongly scattering media. *Appl. Spectrosc.* **2015** 69(3) pp 363-369. Copyright 2015 Society of Applied Spectroscopy.

Optical Detection of Tracer Species in Strongly Scattering Media

Eric M. Brauser,[a,*] Peter E. Rose,[a,b] John D. McLennan,[a,b] Michael H. Bartl[c,*]

[a] *Department of Chemical Engineering, University of Utah, 50 Central Campus Drive, Salt Lake City, UT 84112 USA*
[b] *Energy and Geoscience Institute, 423 Wakara Way, Suite 300, Salt Lake City, UT 84108 USA*
[c] *Department of Chemistry, University of Utah, 315 South 1400 East, Salt Lake City, UT 84112 USA*

A combination of optical absorption and scattering is used to detect tracer species in a strongly scattering medium. An optical setup was developed, consisting of a dual-beam scattering detection scheme in which sample scattering beam overlaps with the characteristic absorption feature of quantum dot tracer species, while the reference scattering beam is outside any absorption features of the tracer. This scheme was successfully tested in engineered breakthrough tests typical of wastewater and subsurface fluid analysis, as well as in batch analysis of oil and gas reservoir fluids and biological samples. Tracers were detected even under highly scattering conditions, conditions in which conventional absorption or fluorescence methods failed.

Index Headings: **Fluorescence; Nanocrystals; Tracers; Turbidity; Light scattering; Light absorbance.**

INTRODUCTION

Optical characterization of absorptive and fluorescent chromophores requires an environment that is conducive to light transmission. This can be a limiting factor in turbid or opaque media due to scattering of transmitted or emitted light. Particulates in turbid media reflect and scatter light, resulting in overestimated absorption measurements and preventing accurate measurement of fluorescence emission. Both of these conditions are common in a range of analytically important environments, including biological samples (cellular, tissue, blood, and plasma), wastewater analysis, and underground oil and water reserve estimations.[1–7]

For example, the interpretation of fluorescence measurements in biological mixtures is a well-documented field that has used various correction techniques to address scattering of light within tissue samples.[2,8,9] Wu et al. reported a method for extracting intrinsic fluorescence from the observed fluorescence in aortic tissue media by coupling the diffuse reflectance with the observed fluorescence, resolving intrinsic fluorescence from distorted fluorescence data.[10] Bradley et al. summarized the evolution of developed models that use the relationships between fluorescence and reflectance in order to extract the true fluorescence emission intensity.[11] These range from a simple reflectance to emission intensity ratio to correction factors that better model the intricacies between excitation and emission wavelengths.[1,3,10]

Received 15 May 2014; accepted 6 August 2014.
* Authors to whom correspondence should be sent. E-mail: eric.brauser@utah.edu, bartl@chem.utah.edu.
DOI: 10.1366/14-07601

These analysis methods require steady-state conditions due to their reliance on the optical parameters and coefficients. While scattering and adsorption coefficients are linear combinations of the numbers of scattering particles and chromophores, the photon mean-free path will change with changes in the number of scattering particles.[11] Thus, unknown changes in scattering particle concentration will lead to errors in the correction factor that must be used for finding the true emission or absorption spectrum.[3]

Similar problems arise in wastewater treatment and subsurface fluid analysis. Here, prior to analyte detection, samples must undergo clarification via filtering or separation using time-intensive chromatography methods.[4–9,12] Emerging energy-related examples are oil and gas reservoir fluid analysis and geothermal systems that necessitate a method for detection of tracers. Connectivity between subsurface zones is becoming an increasingly important feature for characterizing such underground reservoirs, requiring tracers (ionic, molecular, or colloidal materials). Sedimentation in fluids is a common occurrence in underground plumes, which can make detection of tracers difficult and prevents accurate understanding of reservoir characteristics.[13–16] Due to aggressive chemical conditions and high temperatures (up to 350 °C), the range of suitable tracer species is limited. In addition, fluorescence tracing fails at such high temperatures due to quenching. Consequently, tracer detection has to be done in absorption mode in the visible to UV spectral range where scattering has a distinct effect.

The importance of analyte detection in these systems has led us to develop a method in which the combination of scattering and absorbance of light can be used to detect tracer species (such as molecules and nanocrystal quantum dots (QDs)). Our method uses a simple dual light-emitting diode (LED) setup with a sample and a reference beam. The reference beam overlaps with the absorption wavelength range of the tracer species. Therefore, in the presence of tracer, part of the sample beam is absorbed, resulting in reduction of its scattering intensity. The second LED beam operates outside the absorption window of the tracer and thus acts as a reference beam. Comparison of scattering intensities of sample and reference beam thus becomes a reliable means to detect absorbing tracers even under strongly scattering conditions, conditions in which conventional fluorescence and absorption–transmission techniques fail. In addition, our method can also be used in high-temperature conditions in which fluorescence signals would be quenched. We demonstrate successful appli-

0003-7028/15/6903-0363/0
© 2015 Society for Applied Spectroscopy

cation of our method in tracer breakthrough experiments and give several examples of tracer detection in "real-world" samples such as oil and gas recovery liquids, geothermal reservoirs, lipid solutions, and *Escherichia coli* cell lysate.

METHODS

Quantum Dot Tracer Synthesis. Cadmium selenide (CdSe) core–cadmium sulfide shell QD synthesis and characterization were done based on a modified procedure of Rogach et al.[17] Precursor monomer solutions of cadmium perchlorate and 1-1,dimethylselenourea were rapidly injected into alkaline water in a 1 L round-bottom flask at 80 °C in the presence of a coordinating ligand (sodium citrate). The core CdSe crystals were allowed to grow for 10 min before the sulfur source thioacetamide was injected to form a passivating CdS shell (cadmium perchlorate hydrate from Sigma-Aldrich, lot no. 2189GPJ, no further purification; reagent grade thioacetamide from Sigma-Aldrich lot no. 00613EJ, no further purification; 1,1-dimethyl-1-selenourea from Sigma-Aldrich, no further purification; sodium citrate dihydrate from Mallinckrodt, lot no. B07627, no further purification). The QD optical properties were characterized using absorbance and fluorescence spectroscopy using a fiber-optic-coupled Ocean Optics USB2000 spectrometer with a deuterium broadband light source (absorbance) or a LS-450 light source (fluorescence). QD sizes and concentrations were calculated using a previously published empirical method using the characteristic optical absorbance and the wavelength of the absorption peak maximum.[18]

Scattering Test Media. Polystyrene spheres with diameters of 210 and 310 nm (210 nm spheres from Bangs Laboratories; 10% solids, lot no. 9936; 310 nm spheres from Duke Scientific Corp., 10% w/w solids, lot no. 29338) were used as scattering sources in the column experiments. Prior to each experiment, the tubing was flushed with solution of 102 mg/L concentration of 210 nm diameter polystyrene spheres and 20 mg/L concentration of 310 nm diameter polystyrene spheres to establish a consistent background. Mixtures were created of 0.9 μM, 0.6 μM, and 0.2 μM CdSe–CdS QDs with 102 and 20 mg/L of 210 and 310 nm diameter polystyrene spheres, respectively.

Dual-Beam Optical Scattering Detection Setup. Two Ocean Optics LED sources emitting at 470 nm and 640 nm were coupled into a single optical fiber (Fig. 1). A collimating lens was used to focus both LED beams onto the sample (in a spectroscopic cuvette or an Ocean Optics flow cell). The scattered light was collected at a 90° angle by a collimating lens and guided into an Ocean Optics USB2000 spectrometer using an optical fiber. The signal from the spectrometer was analyzed using Ocean Optics SpectraSuite software.

Continuous-Flow (Breakthrough) Detection Studies. The solutions of colloids and QDs were pumped through stainless steel tubing using a Waters M45 solvent delivery system. At the termination of the tubing was a flow cell from Ocean Optics with a 90° optical path for detection of scattering and fluorescence in the effluent (Fig. 1). The tubing was thin-walled 0.1016 cm outer diameter stainless steel tubing obtained from Swagelok, and the total system had a volume of 24.4 mL. The in-line sample excitation source is a blue LED providing light at 470 nm, also from Ocean Optics; the complementary reference source is a red LED emitting at 640 nm (outside the QD absorption region). The eluted volume was measured beginning when a pulse of the QD/polystyrene mixture was first pumped into the tubing. A pulse duration of 2 min of the QD mixture was followed by a 20 min flush with the solution containing 102 and 20 mg/L of 210 and 310 nm diameter polystyrene spheres, respectively. The resulting profile depicts the time that the analyte takes to move through the tubing and reach the flow cell where it can be detected. This measured light intensity plotted against the cumulative volume pumped through the system is referred to in chromatography and subsurface flow literature as a breakthrough curve.

Batch Detection Studies in Industrial and Biological Test Media. Industrial test samples included briny mixtures from a fractured geothermal reservoir containing sediments, and fluids from enhanced gas and oil recovery systems containing thick, dark, long-chain hydrocarbons and a water-based, highly turbid phase with polydisperse sedimentation. These samples were provided by the Energy and Geoscience Institute at the University of Utah. Two biological test samples (an aqueous lipid mixture and an *E. coli* cell lysate) were obtained from the Department of Chemistry at the University of Utah. All test samples were combined with aqueous solutions containing the QD tracer species. The amount of the tracer solution was varied to give total QD tracer concentrations between 0.1 and 1.2 μM. Reference samples were prepared in the same way, however, using same volumes of ultra-pure water instead of the aqueous QD solutions. This was done to prevent differences in scattering of the sample and the reference mixtures due to differences in dilution. Sample and reference mixtures were then filled into spectroscopic cuvettes, and the optical scattering properties were measured using the dual-beam scattering detection setup described above (Fig. 1).

RESULTS AND DISCUSSION

Fluorescence emission in molecules is quenched at elevated temperatures due to the increased number of interspecies collisions and the subsequent increase in non-radiative energy decay channels. This phenomenon is of particular importance for the pursuit of detectable tracer particles in the geothermal industry in which current tracer technologies are being transitioned from radioactive and ionic tracers towards molecules and materials that exhibit characteristic absorbance behavior, emission behavior, or both.[19] Geothermal reservoirs have temperatures up to 350 °C and require tracers that are able to give information about approximate thermal breakthrough time scales and connectivity between injection and production wells.[15,16] Furthermore, water that is produced from a commercial geothermal well has traveled through complex fracture networks that are several kilometers or more in length. These high-temperature, produced waters can contain significant

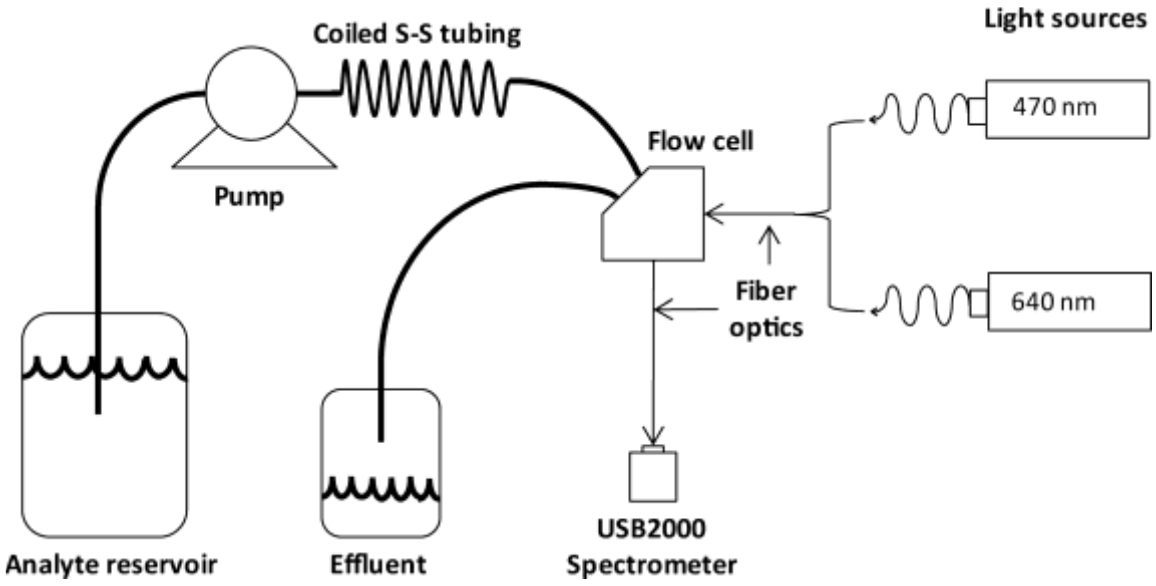

FIG. 1. Dual-beam optical scattering detection setup for continuous-flow studies. Two LED sources with 470 and 640 nm emission outputs act as sample and reference beams, respectively, and are coupled into a single fiber and directed onto flow cell. The scattered light is collected in a 90° angle and guided into a spectrometer. Left side: Continuous-flow setup using stainless steel tubing and a Waters M45 fluid delivery system. For batch measurements the continuous flow setup and flow cell were replaced by a spectroscopic cuvette.

sedimentation, which can cause loss of optical clarity in withdrawn samples. Small particulates picked up in the effluent scatter incident light, extinguishing fluorescence and saturating absorption measurements.

A typical temperature dependence of a fluorescent QD tracer in solution is given in Fig. 2. This shows quenching of the emission intensity with increasing temperature. A quantitative analysis of the intensity of the characteristic QD emission peak at 545 nm is given in Fig. 2b. The intensity is seen to approach zero as temperature is raised beyond 130–140 °C. The quenching of QD emission intensity with increasing temperature is very similar to that of molecular fluorophores and can be fitted by an exponential decay model (solid line in Fig. 2b).[20]

QD luminescence quenching also occurs due to the scattering of emitted light by the larger polystyrene colloidal spheres. As the colloidal sphere concentration is increased while keeping the QD concentration constant, the intensity of emitted light reaching the detector decreases sharply due to the likelihood of a scattering event occurring prior to detection. In strongly scattering media this can result in a complete loss of detectable emission; i.e., emitted light is largely unable to leave the scattering media to reach the detector. The limitation of temperature quenching of tracer signal can be overcome by detecting the optical absorption features of their electronic transitions. While there is a slight wavelength red-shift of the absorption features due to higher population of excited vibrational levels, optical absorption transitions are largely undisturbed by temperature. However, the problem of scattering still needs to be considered, and a typical transmission-type measurement would fail to give reliable absorption measurements in strongly scattering media.

Instead, in our method, we determine tracer chromophore absorption indirectly via a change in light scattering intensity. As an example, Fig. 3 shows the change of scattered light at a frequency overlapping with QD absorption features at a wavelength of 470 nm. The intensity of the scattered light at 470 nm decreased when QDs were present in the effluent, due to absorption by the QDs. This experiment was performed under weakly scattering conditions in order to compare the result to fluorescence detection of QD tracers. Figure 3 demonstrates complete overlap of the two signals, indicating that even in weakly scattering media the reduction of scattered light due to absorption by a chromophore is strong enough to be a detection method.

More importantly, this scattering method also works in highly scattering media—conditions in which fluorescence detection fails. An example is given in Fig. 4 for a mixture of QD chromophore tracers and polystyrene colloids as scattering particles. Using detection of QD fluorescence at 560 nm (the position of QD characteristic emission) fails to show a clear signal of QD presence in the breakthrough curve. Monitoring the intensity of scattered light at a wavelength that overlaps with QD absorption (470 nm), a clear response can be detected at about 25 mL of eluted volume (Fig. 4).

However, this method is vulnerable to random fluctuations in scattering due to changes in the medium not related to the tracer's presence (e.g., change in concentration of scattering particles, or change in size and shape of these scatterers). To account for these changes in background scattering we developed a dual-

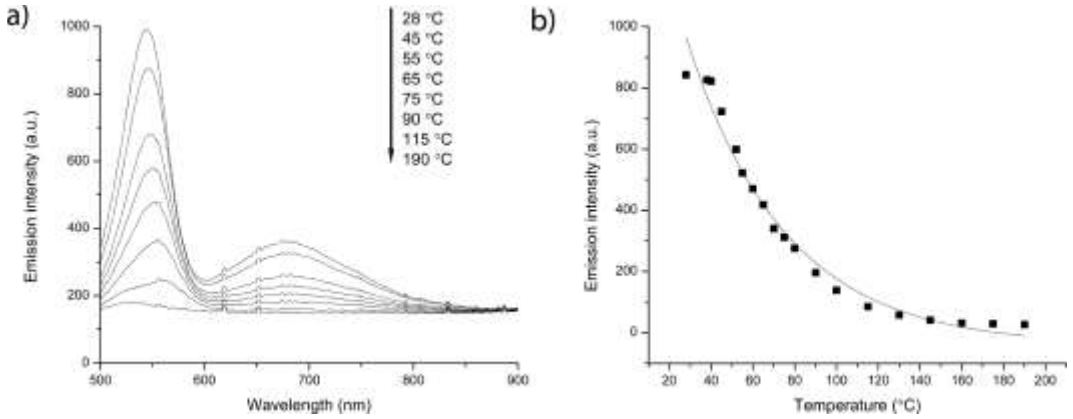

FIG. 2. (**a**) QD photoluminescence emission spectra recorded as a function of solution temperature. (**b**) Decrease of QD emission intensity at a wavelength of 545 nm with increasing temperature. Fit to an exponential decay model is given by solid line.

beam scattering method (Fig. 1). In detail, a turbid sample containing the chromophore tracer is illuminated with two collimated light beams (from two LEDs). The scattered light (from both LEDs) is simultaneously collected at a 90° angle and focused into a spectrometer. The wavelengths of the two incident light beams are chosen so that the shorter-wavelength beam overlaps with the absorption region of the chromophore ("sample beam") and the second beam is at a longer wavelength, outside the chromophore absorption region ("reference beam").

The basic premise is that in the presence of absorbing chromophores the intensity of the scattered sample beam will be reduced, while the reference beam is not affected by the presence of the absorber. The decrease in sample beam intensity normalized to the reference beam is thus a direct, quantitative measure of the presence of chromophore tracers in the strongly scattering medium. As an example, Fig. 5 shows a comparison of the absorption spectrum of a QD chromophore tracer with the output of the dual-LED system: While the shorter-wavelength (470 nm) LED source overlaps with the QD absorption region, the entire profile of the longer-wavelength (640 nm) LED output is outside any QD absorption.

In a typical flow experiment described earlier, as QDs move through the flow cell the incident light intensity of the 470 nm LED will decrease due to absorption by the QDs, while the 640 nm source will remain unaffected. It is important to note that even in the absence of any absorbing species the changes in the scattered light at 460 and 640 nm wavelengths are not identical in magnitude. Since light scatters proportionally to λ^{-4}, there is a larger magnitude increase in the shorter-wavelength LED intensity than the longer-wavelength LED. To take this into consideration, the spectral intensity profile of both of the scattered LED sources (after baseline correction) were evaluated by numerical integration of the intensity over a range of pixels, using λ^{-4} to correct for the wavelength-dependent scattering

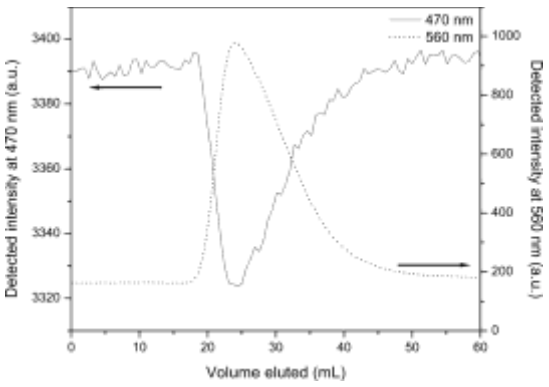

FIG. 3. Breakthrough curves showing response of characteristic QD emission intensity (at a wavelength of 560 nm) along with decrease in scattering intensity (at a wavelength of 470 nm).

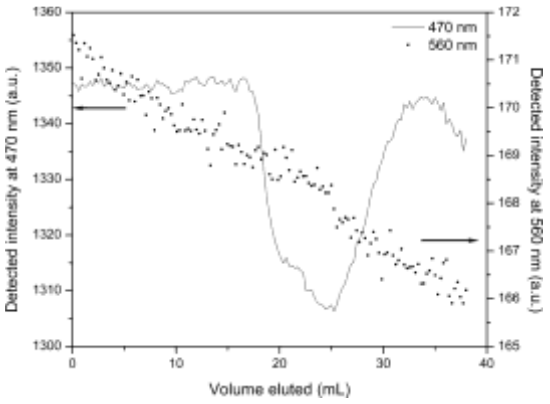

FIG. 4. Breakthrough curves under strongly scattering conditions. Response of characteristic QD emission intensity (at a wavelength of 560 nm) compared to decrease in scattered light intensity (at a wavelength of 470 nm) due to QD absorption.

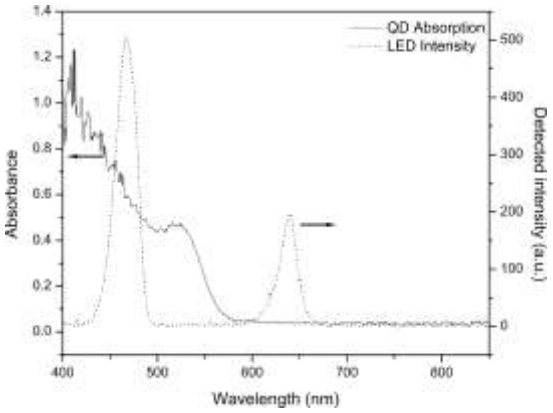

FIG. 5. Optical absorbance profile of QD tracers compared to emission output of the dual-LED setup.

intensity, described by Eqs. 1 and 2:

$$A_k = \sum_{i=1}^{i=m} I_i(\lambda_{i+1}^4 - \lambda_i^4) \tag{1}$$

$$R_{1/2} = \left(\frac{A_1}{A_2}\right) = \frac{\sum_{i=1}^{i=m} I_i(\lambda_{i+1}^4 - \lambda_i^4)}{\sum_{j=m+1}^{j=n} I_j(\lambda_{j+1}^4 - \lambda_j^4)} \tag{2}$$

where A_k = integrated area of emission peak k; I = intensity of data at reference point; $R_{1/2}$ = ratio between scattering beam spectrum ($k = 1$) and reference beam spectrum ($k = 2$); i, j = dummy indices for numeric integration; m = pixel limit for scattering beam integration; n = pixel limit for reference beam integration; and λ = wavelength.

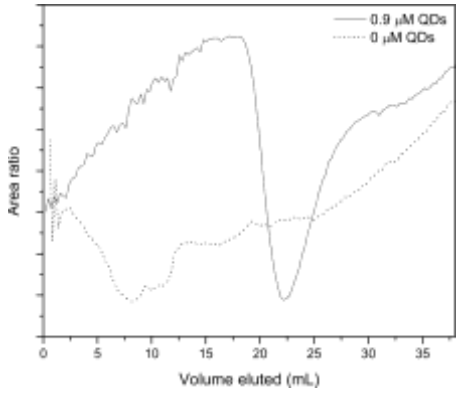

FIG. 6. Area ratio breakthrough curve of a strongly scattering medium with and without the presence of absorbing QD tracers (0.9 μM concentration).

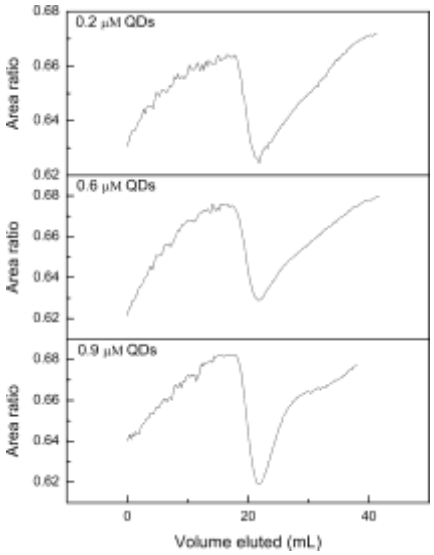

FIG. 7. Area ratio breakthrough curves of a strongly scattering medium with varying concentrations of absorbing QD tracers.

To demonstrate the feasibility of this approach, we tested the method with a strongly scattering colloid solution with and without absorbing QD tracers. For the scattering solution (a 102 and 20 mg/L mixture of polystyrene spheres with diameters of 210 and 310 nm, respectively) the intensity ratio of the sample and reference LED beams, $R_{1/2}$, only shows random fluctuations in the noise level, as shown in Fig. 6. In contrast, for a scattering sample with absorbing QD tracers (0.9 μM concentration), the area ratio breakthrough curve captures the different behaviors of the short- and long-wavelength LEDs, thus detecting the presence of QD tracers at an eluted volume of about 25 mL. (Note that the breakthrough curves for solutions with and without QD tracers are each given as normalized intensity ratios.)

Finally, the sensitivity of this method to QD concentration was investigated. Figure 7 shows a comparison of breakthrough curves of the same scattering medium used for the previous experiment (102 : 20 mg/L mixture of 210 : 310 nm diameter colloids) but with lowered QD tracer concentrations, namely, 0.6 and 0.2 μM. Compared to the 0.9 μM QD sample, lower QD concentrations yielded basically the same breakthrough response with a clear minimum in the area ratio at 22 mL eluted volume due to QD absorption of scattered light. Initial results associated with further lowering the QD tracer concentration showed partial loss of the definition of the curve in the greater elution volume section of the peak (the tailing portion).

We speculate that this loss of definition at the tailing edge is caused by the overlap of the reference LED beam at 640 nm with the weak trap-state emission of QDs in the 600–700 nm range (see also Fig. 2). While this weak effect is negligible at higher QD concentrations its contribution at low concentrations most likely contributes

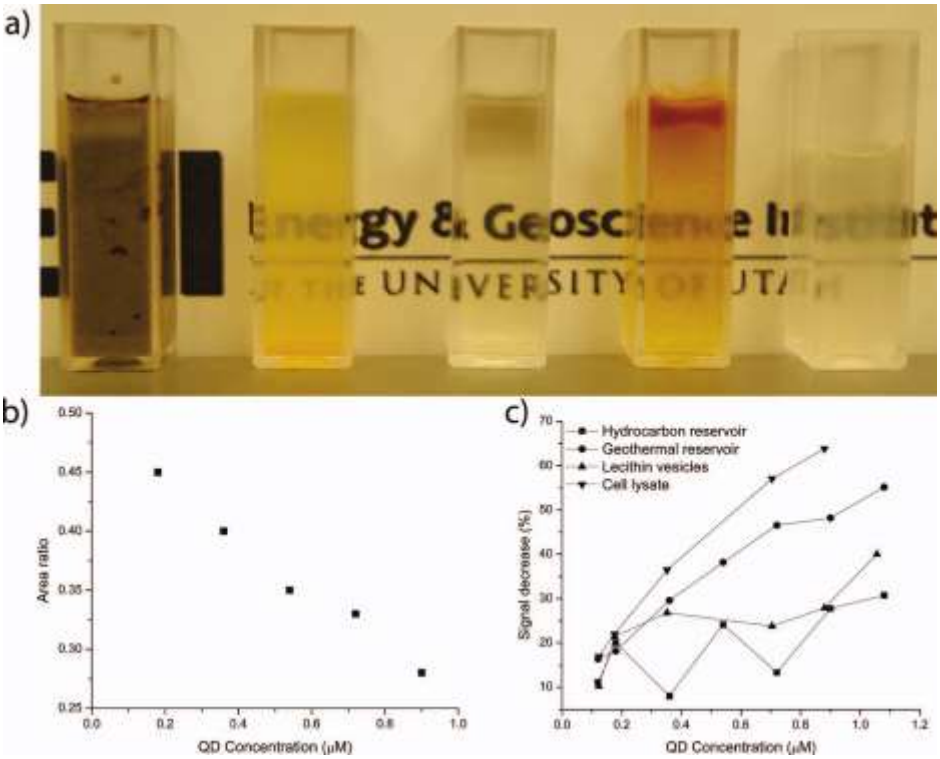

FIG. 8. (**a**) Photograph of test fluid samples. From left: oil recovery fluid, fractured gas reservoir fluid, geothermal reservoir fluid, aqueous lipid mixture, and *E. coli* cell lysate. (**b**) Dependence of the peak area ratio of the scattered sample beam and the scattered reference beam on the QD tracer concentration in the fractured gas reservoir fluid. The turbidity of the sample was held constant for different tracer concentrations. (**c**) Tracer signal response as a function of concentration for four different subsurface and biological test media.

significantly to the scattering signal. Attempts to move the reference beam wavelength further into the infrared part of the spectrum, outside QD trap emission, are currently underway.

To test our method for "real-world" applications we investigated the detection ability of tracers in different industrial and biological fluids, including gas and oil recovery liquids, geothermal reservoir fluids, phospholipid solutions, and *E. coli* cell lysate. Photographs of these fluids (before tracer addition) are given in Fig. 8a. A comparison shows a wide range of optical properties of these test samples: from strongly scattering to weakly turbid, from colorless to colored, and to strongly absorbing throughout the visible spectrum.

All of these samples were then spiked with different concentrations of QD tracers and investigated with our duel-LED setup. In general, we observed a linear decrease in scattering intensity (i.e., decreased area ratio of sample and the reference LED beams) with increased tracer concentrations. As an example, Fig. 8b shows the response behavior of a gas reservoir sample spiked with different concentrations of QD tracer. Despite the orange-yellow turbid nature of the fluid, a linear decrease in scattering intensity with increased tracer concentration (while keeping all other factors constant) was observed. This not only demonstrates the applicability of our method for this underground fluid sample, but the linearity of the signal variation indicates changes in the sample scattering beam are a direct consequence of increased absorbance by the tracer species.

The tracing ability of our method in the other four samples (oil recovery liquids, geothermal reservoir fluids, phospholipid solutions, and *E. coli* cell lysate) is summarized in Fig. 8c. It shows the percent reduction of the scattering intensity of a given test fluid due to the presence of QD tracers at varying concentration. The addition of the aqueous QD tracer solution results in a slight dilution of the test fluids, which can lead to small changes in scattering behavior. To compensate for this factor, reference samples (100% scattering) were prepared by mixing a given test fluid with the same amount of pure water as was used for the QD tracer solution. Several observations are noteworthy: Regardless of the degree of scattering and coloration of the test fluids, a clear tracer signal was observed, even for tracer concentrations as low as 0.1 μM. The same tracing species gave reliable results for various test fluid compositions, including water, oils, particulates, and biological cellular components. Lastly, the ability to use an optical tracer in the oil recovery test fluid, which is highly scattering and strongly absorbing throughout the visible spectrum, is particularly remarkable and under-

lines the broad applicability of our dual-beam scattering detection method.

CONCLUSIONS

We developed a dual-beam scattering method that makes it possible to detect optically active species in highly scattering media through their optical absorption characteristics. This technique offers the potential for analyte–tracer detection in highly scattering media and at high temperatures. Our method is thus of importance for optical detection in strongly scattering and high-temperature environments in which conventional emission and absorption methods fail. By measuring the ratio of the integrated scattering intensities at two distinct wavelength regions (one inside the window of tracer absorption and one outside this window), a scattering area ratio can be evaluated, which is indicative of the presence of the tracing species. We validated this method using tracer breakthrough simulations under various conditions, evaluated initial limits of sensitivity, and demonstrated its application on "real-world" samples from biological mixtures and underground gas, oil, and water reservoir samples. We anticipate our method thus to be useful for a broad range of tracing applications in research and industry.

ACKNOWLEDGMENTS

This work was supported in part by U.S. Department of Energy Geothermal Program (DE-EE0002768) and the National Science Foundation MRSEC program at the University of Utah under grant DMR-1121252. We are grateful to Dr. Jacqueline Siy (Navillum Nanotechnologies) for insightful discussions about aqueous QD synthetic methods, and to Mike Mella (Energy and Geoscience Institute, University of Utah) for help with transport experiments. We also thank Prof. Matthew Kieber-Emmons, Bryce Turner, and Mike Mella for supplying the biological and underground reservoir test samples.

1. A.J. Durkin, S. Jaikumar, N. Ramunujam, R. Richards-Kortum. "Relation Between Fluorescence Spectra of Dilute and Turbid Samples". Appl. Opt. 1994. 33(3): 414-423.
2. G. Themelis, J.S. Yoo, K.S. Sohm, R. Schulz. "Real-time Intraoperative Fluorescence Imaging System Using Light-Absorption Correction". J. Biomed. Optics. 2009. 14(6): 060412.
3. N.N. Zhadin, R. Alfano. "Correction of the Internal Absorption Effect in Fluorescence Emission and Excitation Spectra from Absorbing and Highly Scattering Media: Theory and Experiment". J. Biomed. Opt. 1998. 3(2): 171-186.
4. J.H. Goldman, S.A. Rounds, J.A. Neeboda. "Applications of Fluorescence Spectroscopy for Predicting Percent Wastewater in an Urban Stream". Environ. Sci. Tech. 2012. 46(8): 4374-4381.
5. W.-T. Li, S.-Y. Chen, Z.-X. Xu, Y. Li, C.-D. Shuang, A.-M. Li. "Characterization of Dissolved Organic Matter in Municipal Wastewater Using Fluorescence PARAFAC Analysis and Chromatography Multi-Excitation/Emission Scan: A Comparative Study". Environ. Sci. Tech. 2014. 48(5): 2603-2609.
6. M.M. Schultz, C.P. Higgins, C.A. Huset, R.G. Luthy, D.F. Barofsky, J.A. Field. "Mass Balance Study of Fluorochemicals During Wastewater Treatment". Environ. Sci. Tech. 2006. 40: 7350-7357.
7. C.A. Stedmon, S. Markager, R. Bro. "Tracing Dissolved Organic Matter in Aquatic Environments Using a New Approach to Fluorescence Spectroscopy". Mar. Chem. 2003. 82(3-4): 239-254.
8. Y. Chen, Z.-P. Chen, J. Ying, J.-W. Jin, J. Zhang, R.-Q. Yu. "Quantitative Fluorescence Spectroscopy in Turbid Media: A Practical Solution to the Problem of Scattering and Absorption". Anal. Chem. 2013. 85(4): 2015-2020.
9. C.T. Xu, J. Axelsson, S. Andersson-Engels. "Fluorescence Diffuse Optical Tomography Using Upconverting Nanoparticles". App. Phys. Lett. 2009. 94(25): 251107.
10. J. Wu, M.S. Feld, R.P. Rava. "Analytical Model for Extracting Intrinsic Fluorescence in Turbid Media". Appl. Opt. 1993. 32(19): 3585-3595.
11. R.S. Bradley, M.S. Thorniley. "A Review of Attenuation Correction Techniques for Tissue Fluorescence". J. R. Soc. Interface. 2006. 3(6): 1-13.
12. S. Pérez, D.S. Aga. "Recent Advances in the Sample Preparation, Liquid Chromatography Tandem Mass Spectrometric Analysis and Environmental Fate of Microcystins in Water". Trends Anal. Chem. 2005. 24(7): 658-670.
13. N.E. Deeds, G.A. Pope, D.C. McKinney. "Vadose Zone Characterization at a Contaminated Field Site Using Partitioning Interwell Tracer Technology". Environ. Sci. Tech. 1999. 33(16): 2745-2751.
14. D.D. Bosch, R.K. Hubbard, R.A. Leonard, D.W. Hicks. "Tracer Studies of Subsurface Flow Patterns in a Sandy Loam Profile". Trans. Am. Soc. Agr. Eng. 1999. 42(2): 337-349.
15. G.M. Shook, J.H. Forsmann. "Tracer Interpretation Using Temporal Moments on a Spreadsheet". U. S. Department of Energy, 2005. DE-AC07-05ID14517.
16. P. Rose, K. Leecaster, S. Clausen, R. Sanjuan, M. Ames, P. Reimus, M. Williams, V. Vermeul, D. Benoit. "A Tracer Test at the Soda Lake, Nevada Geothermal Field Using a Sorbing Tracer". Proceedings, Thirty-Seventh Workshop on Geothermal Reservoir Engineering. Stanford University, Stanford, CA; January 30–February 12, 2012.
17. A.L. Rogach, D. Nagesha, J.W. Ostrander, M. Giersig, N.A. Kotov. "Raisin Bun-Type Composite Spheres of Silica and Semiconductor Nanocrystals". Chem. Mater. 2000. 12(9): 2676-2685.
18. W.W. Yu, L. Qu, W. Guo, X. Peng. "Experimental Determination of the Extinction Coefficient of CdTe, CdSe, and CdS Nanocrystals". Chem. Mater. 2003. 15(14): 2854-2860.
19. R. Haggerty, S.A. McKenna, L.C. Meigs. "On the Late-Time Behavior of Tracer Test Breakthrough Curves". Water Resources Res. 2000. 36(12): 3467-3479.
20. R.G. Bennett, P.J. McCartin. "Radiationless Deactivation of the Fluorescence State of Substituted Anthracenes". J. Chem. Phys. 1966. 44(5): 1969-1972.

CHAPTER 6

OVERALL CONCLUSIONS AND DIRECTION

The purpose of understanding how colloids transport in porous media originated with natural occurring particles, and more recently has been driven by the increased in technological applications of nanoparticles. Current literature has identified a large number of parameters that control or impact colloid transport under various circumstances, all of which are relevant to one of countless subsurface environments. Colloids larger than 100 nm have been well studied in porous media transport. Experiments have developed from early model environments to include complex natural conditions and high-level modeling. Only a small amount of study has gone into nanoparticle colloids with diameters smaller than 100 nm, even though fundamental research and application is growing in other research fields. This study looked to address these issues, beginning with fundamental nanoparticle behavior in the fluid phase following with their introduction to high temperature porous medium and transport.

Crystal dissolution was done experimentally and modeled by developing a material balance of the monomers between the crystal and fluid phase. This approach bypasses the complex mechanisms involved in colloid formation and reduces the number of parameters for optimization to only growth and dissolution reactions. Parameter determination over a range of temperatures provided the basis for calculating activation energy for the growth and dissolution reactions: 14±6 and 27±8 kJ mol^{-1}, respectively. As kinetic parameters for both

reactions were found, the fundamental thermodynamic properties governing the system could be determined using the van't Hoff equation. The enthalpy and entropy of the system were -15±7 kJ mol^{-1} and -37±18 J mol^{-1} K^{-1}. At high temperatures, crystal growth is driven by the presence of excess monomers in solution due to the large values of the kinetic growth rate constant. This is also the consequence in aqueous systems, where over a range of ionic strength and temperatures QDs exhibited linear growth due to excess monomers in solution. Activation energies for QD growth at 10, 50, and 100 mM ionic strength were 37 ± 2, 50 ± 5, and 53 ± 3 kJ mol^{-1}, showing that higher ionic strength led to larger activation energies, but also showed more rapid crystal growth. The combination of these solubility studies show that QD sizes under geothermal conditions will not be static in the presence of fluid-phase monomers, instead changing in predictable ways.

The behavior of monomers and ligands at the interface between the QDs and the fluid phase dictate how they will interact with other surfaces. Electrostatic interaction has often been identified as a governing influence in colloid transport. From existing surface charge interaction calculations, the forces are measurably affected by the concentration of ions in solution and have led to increased retention. There is little existing evidence that shows how nanoparticles will behave in high temperature transport conditions, though from the force equations, changing temperature would predict minimal changes in retention. QD transport was evaluated by measuring QD concentration in the effluent through equilibrated columns of Ottawa sand. The results of nine experiments show that the QD recovery decreases from 100% at low ionic strength and temperature to 5% at 150 °C and 100 mM ionic strength. The two implications of these transport results are 1) that the QDs are increasingly adsorbing to the surface at elevated ionic strength and temperatures, and 2) at the most extreme conditions the QDs are exhibiting time dependent adsorption kinetics. Surface detection using ICP trace metal analysis revealed that QDs are adsorbed on the surface. The magnitude

increased with the transport conditions, but exhibited both flux-driven deposition near the inlet and reversible deposition with downstream detection peaks. Only at 150 °C and 100 mM ionic strength was near-inlet deposition completely dominant, highlighting the complexity that effects QD transport. In order to determine if multilayer deposition was causing the unique BTC profiles, governing transport equations were developed with kinetic parameters that depended on the amount of deposited QDs. Model results of these equations showed good agreement with the high ionic strength and temperature experiments that exhibited retention that increased over time. The increased retention also agreed with the results of the QD-QD interaction potential that predict lower primary energy barriers at all ionic strength and temperature compared to the QD-surface energy features, leading to higher chances of retention when QDs aggregate to QDs that are previously adsorbed.

APPENDIX

DERIVIATION OF KINETIC EQUATIONS

In order to create a material balance for cadmium in the system, a control volume was first created around a single QD that was introduced into the monomer-free solvent. This "unit crystal" was used to simulate the behavior of all the nanocrystals in the ensemble. Accounting for crystal growth and dissolution allows the general material balance for cadmium to written as follows:

$$\frac{d}{dt}[Cd] = k_d A(t)[Nc] - k_g A(t)[Nc][Cd] \tag{A.1}$$

$$[Cd] = \frac{N_{Cd}}{Volume} = \left[\frac{mol\ Cd}{L^3}\right];\ [Nc] = \frac{N_0}{Volume} = \left[\frac{mol\ Crystals}{L^3}\right]$$

$$\frac{d}{dt}\frac{mol\ Cd}{V} = k_d A(t)\left[\frac{molCrys}{V}\right] - k_g A(t)\left[\frac{molCrys}{V}\right]\left[\frac{molCd}{V}\right] \tag{A.2}$$

N_{Cd}: $Number\ of\ cadmium\ elements\ in\ solution$

N_0: $Number\ of\ particles\ \left(Here, N_0 = \frac{1}{6.02E23}\right)$

$k_d, k_g = Dissolution\ and\ growth\ kinetic\ parameters$

$A(t) = \ Surface\ area\ of\ single\ crystal\ at\ time\ t$

$Unit\ Volume\ V_U = Total\ Volume\ /\ Number\ of\ Crystals$

If the reaction volume V is constant, then it can come out of the equation. This results in the volume-independent version of (A.3) below:

$$\frac{d}{dt}molCd = k_d A(t)(molCrys) - k_g A(t)(molCrys)\left(\frac{molCd}{Vol}\right) \tag{A.3}$$

This assumes that the number of crystals is unchanging, that the reaction volume is constant, and all of the particles are identical size. The number of Cd monomers in solution at time t can be expressed by the loss of Cd elements from the colloidal phase over Δt:

$$N_{Cd} = N_0^{NC} - N_t^{NC} \tag{A.4}$$

N_0^{NC}: *The number of Cd elements in the nanocrystal at* $t = 0$

N_t^{NC}: *Number of Cd elements in the nanocrytal at time* t

V_m = *molar volume of CdSe*

$$N^{NC} = \frac{Volume}{Crys} * V_m^{-1} = V_m^{-1}\left(\frac{4\pi}{3}\right)r^3 \tag{A.5}$$

$$\frac{dN_{Cd}}{dt} = k_d A(t)N_0 - k_g A(t)(N_0)\left(\frac{1}{V_m}\right)\left(\frac{N_0^{NC} - N_t^{NC}}{V_T}\right) \tag{A.6}$$

The number of Cd elements at times 0 and t can be expressed in terms of the crystal volume, molar volume, and Avagadro's constant

$$\frac{dN_{Cd}}{dt} = k_d A(t) N_0 - k_g A(t) N_0 \left(\frac{4\pi}{3}\right) V_m^{-1} \left(\frac{r_0^3 - r(t)^3}{V_T}\right) \quad \text{(A.7)}$$

$$r_0 : Initial\ particle\ radius$$

$$r(t) : Particle\ radius\ at\ time\ t$$

$$N_A : Avagadro's\ constant$$

$$V_M : Molar\ volume\ of\ CdSe$$

The derivative can be expressed as a product of its partial derivatives, and the same relation can be used to express the change of Cd elements within the crystal in terms of the volume change:

$$-\frac{V_M}{1}\frac{dN_{Cd}}{dt} = \frac{dV}{dt} \quad \text{(A.8)}$$

Equation (A.8) can be expressed as a set of partial derivatives:

$$\frac{dV}{dt} = \frac{\partial V}{\partial r}\frac{\partial r}{\partial t} \quad \text{(A.9)}$$

$$\frac{1}{V_m}\frac{dV}{dt} = k_d A(t) N_0 - k_g A(t) N_0 \left(\frac{4\pi}{3}\right) V_m^{-1} \left(\frac{r_0^3 - r(t)^3}{V_T}\right) \quad \text{(A.10)}$$

$$\frac{dV}{dt} = V_m k_d A(t) N_0 - V_m k_g A(t) N_0 \left(\frac{4\pi}{3}\right) V_m^{-1} \left(\frac{r_0^3 - r(t)^3}{V_T}\right) \quad \text{(A.11)}$$

Expressing volume in terms of the radius results in simplification of (A.11)

$$\frac{\partial V}{\partial r} = \frac{\partial}{\partial r}\left(\left(\frac{4\pi}{3}\right)r^3\right) = 4\pi r(t)^2 = A(t) \tag{A.12}$$

Plugging the results from equations (A.8), (A.11), and (A.12) into (A.7) and cancelling the V_M in the growth term results in a differential equation describing the change in radius as a function of time and radius:

$$\begin{aligned}\frac{dV}{dt} = \frac{\partial V}{\partial r}\frac{\partial r}{\partial t} = \; & A(t)\frac{\partial r}{\partial t} \\ & = V_m k_d A(t) N_0 - k_g A(t) N_0 \left(\frac{4\pi}{3}\right)\left(\frac{r_0^3 - r(t)^3}{V_T}\right)\end{aligned} \tag{A.13}$$

$$\frac{dr(t)}{dt} = V_m k_d N_0 - k_g N_0 \left(\frac{4\pi}{3}\right)\left(\frac{1}{V_T}\right)(r_0^3 - r(t)^3) \tag{A.14}$$

$$\begin{aligned}\frac{dr(t)}{dt} = -\frac{V_M}{1}\frac{1}{A(t)}\Big[& k_d A(t) \\ & - k_g A(t)\left(\frac{4\pi}{3}\right)\left(\frac{1}{V_M}\right)(r_0^3 - r(t)^3)\left(\frac{1}{V_u}\right)N_0\Big]\end{aligned} \tag{A.15}$$

$$\frac{dr(t)}{dt} = -V_m k_d N_0 + k_g \left(\frac{4\pi}{3}\right)(r_0^3 - r(t)^3)\left(\frac{1}{V_u}\right)N_0 \tag{A.16}$$

The units of kd, kg, and K are easily reported and are consistent with all equations within the derivation of (A.16):

$$k_d = [L^{-2}T^{-1}];\ k_g = [M^{-1}L^{-2}T^{-1}];\ K_{eq} = \frac{k_d}{k_g} = [M]$$

In order for kd and kg to have units consistent with the system of interest, they are defined as:

$$k_d = [nm^{-2}s^{-1}];\ k_g = \left[\left(\frac{mol}{nm^3}\right)^{-1} nm^{-2}s^{-1}\right];\ K_{eq} = \frac{k_d}{k_g} = \left[\frac{mol}{nm^3}\right]$$

For reporting purposes, however, these kinetic parameters can be converted to conventional units with simple unit transformations:

$$k_d = [nm^{-2}s^{-1}]\left(\frac{10^{-9}nm}{m}\right)^2;\ k_g = \left[\left(\frac{mol}{nm^3}\right)^{-1} nm^{-2}s^{-1}\right]\left(\frac{10^{-9}nm}{m}\right)$$

$$K_{eq} = \frac{k_d}{k_g} = \left[\frac{mol}{m^3}\right] = \left[\frac{mol}{1000L}\right]$$

As time approaches infinity, the change in radius becomes negligible as the dissolution and growth kinetics balance, by setting the two terms on the RHS of (A.16) equal to each other, one rate constant can be eliminated.

$$k_d = \frac{k_g N_A}{V_M}\left(\frac{4\pi}{3}\right)\left(r_0^3 - r_{eq}^3\right) \qquad \text{(A.17)}$$

r_{eq}: *The average particle radius when the system is in equilibrium*

Plugging the result provided in (A.17) back into (A.16) allows for the simplification of the differential equation.

$$\frac{dr(t)}{dt} = -k_g\left(\frac{4\pi}{3}\right)\left[\left(r_0^3 - r_{eq}^3\right) + \left(r_0^3 - r(t)^3\right)\right] \tag{A.18}$$

$$\frac{dr(t)}{dt} = k_g\left(\frac{4\pi}{3}\right)\left[r_{eq}^3 - r(t)^3\right] \tag{A.19}$$

Equation (A.19) is the resulting differential equation to describe the change of radius of a single crystal per unit volume. The change for all crystals per unit volume is then expressed with the total number of particles in solution:

$$\frac{dr(t)}{dt} = k_g N_0\left(\frac{4\pi}{3}\right)\left[r_{eq}^3 - r(t)^3\right] \tag{A.20}$$

In order to determine the kinetic rate constants shown in equation (A.8), two approaches were attempted. The first used experimental data for the measured particle radius *r(t)* to fit a dissolution curve to equation (A.20). The parameter k_g was optimized so that the square of the residual differences between the data and the model was minimized. The dissolution rate constant k_d was then calculated using equation (A.17). The second method simultaneously optimized the k_d and k_g parameters in equation (A.16) and minimized the residuals squared.